

Kennesaw State University

DigitalCommons@Kennesaw State University

Master of Science in Chemical Sciences Theses

Department of Chemistry and Biochemistry

Spring 5-5-2020

Mineral-Surface Chemistry of Hydroxyapatite and Urea-Rich Solutions

Estefania Garcia

Follow this and additional works at: https://digitalcommons.kennesaw.edu/mscs_etd

 Part of the [Chemistry Commons](#), [Geochemistry Commons](#), and the [Other Astrophysics and Astronomy Commons](#)

Recommended Citation

Garcia, Estefania, "Mineral-Surface Chemistry of Hydroxyapatite and Urea-Rich Solutions" (2020). *Master of Science in Chemical Sciences Theses*. 33.

https://digitalcommons.kennesaw.edu/mscs_etd/33

This Thesis is brought to you for free and open access by the Department of Chemistry and Biochemistry at DigitalCommons@Kennesaw State University. It has been accepted for inclusion in Master of Science in Chemical Sciences Theses by an authorized administrator of DigitalCommons@Kennesaw State University. For more information, please contact digitalcommons@kennesaw.edu.

Mineral-Surface Chemistry of Hydroxyapatite and Urea-Rich Solutions

by

Estefania L. Garcia

Master of Science in Chemical Sciences

Kennesaw State University, 2020

Submitted in Partial Fulfillment of the Requirements

For the Degree of Master of Science in the

Department of Chemistry and Biochemistry

Kennesaw State University

May 2020

Committee Chair

Graduate Program Coordinator

Committee Member

Department Chair

Committee Member

College Dean

ACKNOWLEDGMENTS

Thank you to Dr. Heather Abbott-Lyon, for being an excellent mentor. I truly appreciate the confidence and independence that you instill in your students.

Center for Chemical Evolution for the opportunities, feedback, and funding of this project.

I appreciate my supportive lab family in the Abbott-Lyon laboratory, for the unexpected adventures, and Katie Slavicinska for her experimental design, guidance, and friendship.

My committee members: Dr. Altug Poyraz, Dr. Huggins Msimanga, faculty and staff at Kennesaw State University, thank you to everyone that I've bothered and your willingness to help.

My previous mentors at Dalton State College, Dr. Dean Turner, Dr. April Kay, and Dr. Tricia Scott for giving me the tools to pursue graduate school.

My friends, family, and most importantly my parents, there are no words for the sacrifices you've made, thank you for your unwavering support.

ABSTRACT

On this planet the development of life requires six essential elements: C, H, O, N, P, and S. These elements are present in gaseous form, with the exception of phosphorus, which is primarily found in solid mineral sources. Phosphorus in biological systems is significant through its involvement in metabolic functions (*e.g.*, Coenzyme A), cell structure (*i.e.*, phospholipid membranes), and genetic storage/transfer (*i.e.*, phosphodiester bonds in DNA and RNA). However, an ambiguity remains with the assimilation of phosphorus in biological systems, caused by its habitual presence in insoluble phosphate mineral sources. Recent research has found that insoluble phosphate minerals, when combined with urea-rich solvents, can release sequestered phosphate into solution and promote mineral transformation to more soluble secondary minerals.

Our study investigates surface interactions of hydroxyapatite, a prebiotically plausible phosphate mineral source on the early Earth, with urea-rich solvents (urea, ammonium formate, and water, UAFW) and magnesium sulfate. Time-dependent infrared studies were conducted via polarization modulated – infrared reflection-absorption spectroscopy (PM-IRRAS) to monitor structural changes of the mineral surface. Thin hydroxyapatite films were analyzed with scanning electron microscopy (SEM), energy-dispersive x-ray spectroscopy (EDX), and PM-IRRAS before and after reaction. Phosphate depletion was observed with PM-IRRAS and was supported by more established instrumentation including nuclear magnetic resonance spectroscopy (NMR) and energy dispersive x-ray spectroscopy (EDX). Film corrosion was observed by post-reaction characterization, and ammonium formate was found to activate orthophosphate release into solution.

TABLE OF CONTENTS

LIST OF FIGURES & TABLES	V
LIST OF KEY ACRONYMS	X
CHAPTER 1. INTRODUCTION	1
1.1 Origins of Life and Phosphorus	1
1.2 Ubiquity and Biological Significance of Phosphorus	4
1.3 The Phosphate Problem	5
1.4 Initial Approaches to Understanding Prebiotic Phosphorylation	7
1.5 Twenty-first Century Approaches to Understanding Prebiotic Phosphorylation	9
1.6 Understanding Prebiotic Chemistry Through Mineral Surfaces	13
1.6.1 Crystalline vs. Mineral Surfaces	14
CHAPTER 2. EXPERIMENTAL METHODS	19
2.1 Methodology Overview	19
2.2 Reflection Absorption Infrared Spectroscopy (RAIRS)	25
2.2.1 Theory of RAIRS	25
2.2.2 Theory of Polarization Modulation-Infrared Absorption Reflection Spectroscopy (PM-IRRAS).....	29
2.2.3 Experimental Implementation	30
2.2.3.1 Optical Alignment	30
2.2.3.2 Experimental Modifications	38
2.2.4 Data Collection and Interpretation	40
2.3 Characterization Methods	45
2.3.1 X-ray Diffraction (XRD)	46
2.3.2 Scanning Electron Microscopy (SEM) & Energy Dispersive X-Ray Spectroscopy (EDX)	48
2.3.3 Nuclear magnetic resonance spectroscopy (NMR).....	50
3.2 Influence of Additives, Temperature, and pH	61

CHAPTER 4. REACTIVITY STUDIES	67
4.1 Reactivity of Copper	67
4.2 Mitigation Strategies	69
4.2.1 Alternative Solvents	69
4.2.2 Alternative metal substrates.....	72
4.3 Synthesis on Gold	78
CHAPTER 5. UREA, AMMONIUM FORMATE, AND WATER ON HA	82
5.1 Data Analysis of water (W) on HA at 298 K.....	84
5.2 Data Analysis of urea-water (UW) on HA at 298 K	88
5.3 Data Analysis of ammonium formate-water (AFW) on HA at 298 K	95
5.5 Data Analysis of MgSO₄ and UAFW on HA	108
CHAPTER 6. CONCLUSION AND FUTURE WORK.....	127
APPENDIX 1. STANDARD OPERATING PROCEDURE FOR SEM	153

LIST OF FIGURES & TABLES

- Fig. 1.1** Artists' image of the early Earth
- Fig. 1.2** Structure of reduced P compounds
- Fig. 1.3** Diagram of significant applications relating to surface science
- Fig. 1.4** Surface defect sites
- Fig. 2.1** Scheme representation of overall experimental methodology for this study
- Fig. 2.2** Schematic and experimental setup for electrochemical deposition.
- Fig. 2.3** Cyclic Voltammogram Sample 26
- Fig. 2.4** Schematic of electric field vectors for light polarization
- Fig. 2.5** Relationship between incident angle and absorption intensity
- Fig. 2.6** Dipole theory illustration
- Fig. 2.7** Schematic of Optical layout
- Fig. 2.8** Schematic of Liquid-Solid cell mount
- Fig. 2.9** Real refracted index as a function of wavenumbers, obtained through the Kramers-Kronig method
- Fig. 2.10** Critical angle for different interfaces as a function of wavenumbers
- Fig. 2.11** PM-IRRAS spectra of HA/Cu, where incidence angle is varied
- Fig. 2.12** Teflon body cell used for liquid-solid interface analysis
- Fig. 2.13** Comparison of PM-IRRAS spectra with and without a purge system

Fig. 2.14 Grid polarizer, s- and p- polarizations

Fig. 2.15 Comparison of background spectra for HA, R_s/R_B

Fig. 2.16 Comparison of data processing methods, with and without a purge system

Fig. 2.17 Schematic of crystal structure and its relation to XRD

Table 1. Summary of electrochemical deposition conditions for HA/Cu samples

Fig. 3.1 Infrared signal intensity for HA deposited onto Cu foils

Fig. 3.2 PM-IRRAS baseline corrected spectra of HA/Cu samples

Fig. 3.3 XRD-spectra of HA/Cu samples

Fig. 3.4 SEM and EDX of an HA/Cu sample

Fig. 3.5 SEM image of an HA/Cu sample

Fig. 3.6 Image of an HA/Cu sample with addition of NaNO_3

Fig. 3.7 SEM image of HA/Cu film with no pH adjustment

Fig. 3.8 SEM image for the surface and cross-section of HA/Cu

Fig. 3.9 SEM images of HA/Cu films with 2%, 4%, and 6% (w/w) H_2O_2

Fig. 3.10 SEM images of HA/Cu films with 2% at 10 mm and 200 μm

Fig. 3.11 Image of HA/Cu sample with 0.80 mM and 1.80 mM SDS at different pHs

Fig. 4.1 Image of HA/Cu in liquid-solid cell after interaction with UAFW

Fig. 4.2 Reaction of HA/Cu samples with urea, water and ammonium formate

Fig. 4.3 Proposed reaction mechanism for ammonium formate and copper oxide

Fig. 4.4 Image of HA/Cu samples with UAFW, adjusted at different pHs

Fig. 4.5 Reaction of ammonia and water

Fig. 4.6 Image of HA on iron and stainless steel

Fig. 4.7 Image of iron, stainless steel, and nickel with UAFW

Table 4.1 Summary of control experiments for UAFW, Cu, and HA

Table 4.2 EDX of iron dried down product

Table 4.3 EDX of stainless steel dried down product

Fig. 4.8 External standard calibration plot for analysis of aluminum

Table 4.4 EDX of gold dried down product

Table 4.5 Summary of observations and analytical techniques used for metal and UAFW reactivity

Fig. 4.9 Image of a bare and HA electrodeposited gold-plated flat mirror

Fig. 4.10 Images of HA/Au film improvement

Table 4.6 Synthesis conditions for HA/Au samples

Table 4.7 EDX of HA/Au sample

Fig. 4.11 SEM image comparison of HA/Cu and HA/Au samples

Fig. 5.1 Experimental setup for reactivity experiments

Fig. 5.2 PM-IRRAS R-spectra of H₂O adsorbed to HA at room temperature

Fig. 5.3 PM-IRRAS R and B-spectra of H₂O adsorbed to HA at room temperature

Fig. 5.4 PM-IRRAS R-spectra of UW adsorbed to HA

Fig. 5.5 PM-IRRAS O-spectra of UW adsorbed to HA

Fig. 5.6 PM-IRRAS B-spectra of UW adsorbed to HA

Table 5.1 EDX of HA/AU after a four hour reaction with UW

Fig. 5.7 EDX mapping of HA/Au sample after four hour reaction with UW

Fig. 5.8 ¹H-decoupled-³¹P-NMR-spectra of UW at one hour intervals

Fig. 5.9 PM-IRRAS O-spectra of AFW adsorbed to HA

Fig. 5.10 PM-IRRAS R-spectra of Au, optical system with no sample, and HA

Table 5.2 EDX of HA/Au after a four hour reaction with AFW

Fig. 5.11 PM-IRRAS B-spectra of AFW adsorbed to HA

Fig. 5.12 PM-IRRAS R-spectra of AFW adsorbed to a *wet* HA surface

Fig. 5.13 ^1H -decoupled- ^{31}P -NMR-spectra of AFW at one hour intervals

Fig. 5.14 PM-IRRAS R-spectra of UAFW adsorbed to HA

Fig. 5.15 PM-IRRAS B-spectra of UAFW adsorbed to HA

Table 5.3 EDX of HA/Au after a four hour reaction with UAFW

Fig. 5.16 Comparison of PM-IRRAS B-spectra for UAFW, AFW, and UW adsorbed to HA for one hour

Fig. 5.17 Comparison of PM-IRRAS B-spectra of UAFW, AFW, and UW adsorbed to HA for four hours

Fig. 5.18 ^{31}P NMR decoupled-spectra of UAFW at one hour intervals

Fig. 5.19 PM-IRRAS B-spectra of 249 mM MgSO_4 UAFW, 747 mM MgSO_4 UAFW, and UAFW adsorbed to HA

Fig. 5.20 SEM image of a HA/Au sample after a four hour reaction with a saturated MgSO_4 solution (5 M).

Fig. 5.21 PM-IRRAS B-spectra of 249 mM MgSO_4 UAFW, 747 mM MgSO_4 UAFW, and UAFW adsorbed to HA at 298 K after one hour

Fig. 5.22 PM-IRRAS O-spectra of 249 mM MgSO_4 UAFW, 747 mM MgSO_4 UAFW, and UAFW adsorbed to HA at 298 K after one hour, $4000\text{-}2000\text{ cm}^{-1}$

Fig. 5.23 PM-IRRAS O-spectra of 249 mM MgSO_4 UAFW, 747 mM MgSO_4 UAFW, and UAFW adsorbed to HA at 298 K after one hour, $2000\text{-}750\text{ cm}^{-1}$

Table 5.4 EDX of HA/Au after a four hour reaction with 249 mM MgSO_4 UAFW and 747 mM MgSO_4 UAFW

Fig. 5.24 EDX mapping of the HA/Au sample after a four hour reaction with 249 mM MgSO₄ UAFW at 298 K.

Fig. 5.25 EDX mapping of the HA/Au sample after a four hour reaction with 747 mM MgSO₄ UAFW

Fig. 5.26 ³¹P NMR decoupled-spectra of 249 mM MgSO₄ during reaction with HA

Fig. 5.27 ³¹P NMR decoupled-spectra of 747 mM MgSO₄

Fig. 5.28 ³¹P NMR decoupled-spectra of: 416 mM MgSO₄ and 831 mM MgSO₄

Tables 5.5-5.8 Summary of PM-IRRAS assignments for HA, W/HA, UW/HA, AFW/HA, UAFW/HA, 249 mM MgSO₄/HA, 747 mM MgSO₄/HA, and reference values in literature

LIST OF KEY ACRONYMS

HA: hydroxyapatite or hydroxylapatite

SEM: scanning electron microscopy

EDS/EDX: energy dispersive X-ray spectroscopy

RAIRS/IRRAS: reflection-absorption infrared spectroscopy

PM-IRRAS: polarization modulated – infrared reflection absorption spectroscopy

XRD: X-ray diffraction

NMR: nuclear magnetic resonance spectroscopy

AAS: atomic absorption spectroscopy

PPM: parts per million (mg/L)

UAFW: urea, ammonium formate, and water

UW: urea and water

AFW: ammonium formate and water

CHAPTER 1. INTRODUCTION

*“The beauty of a living thing is not the atoms that go into it,
but the way those atoms are put together.”*

- Carl Sagan

1.1 Origins of Life and Phosphorus

Of the eight planets located in the Milky Way galaxy, our home planet, a pale blue dot is the only one known to inhabit life.¹ This pale blue dot formed more than 4.55 billion years ago with life estimated to have originated 4.3 billion years ago.^{2,3} The history of the Earth can be broken down into four geological periods (eons): Hadean, Archean, Proterozoic, and Phanerozoic.⁴ The first period on the Earth is referred to as the Hadean (4.56-3.85 billion years ago), with water present on the surface by 4.3 billion years ago.³ Conditions during the Hadean were drastically different compared to modern day Earth. For example, there was a reducing atmosphere (limited oxygen), with gases consisting of methane (CH₄), carbon dioxide (CO₂), and smaller amounts of sulfur dioxide (SO₂), sulfur oxide (SO), ammonia (NH₃), and nitrogen (N₂).⁵⁻⁸ Additionally, the Hadean and early Archean had high temperatures as well as more hydrothermal vents and volcanoes than modern Earth. Evidence of these high temperatures come from komatiites, which are rocks that were mainly present on this high temperature

environment.⁹ The surface of the early Earth (represented in Fig. 1.1) was also largely composed of water and had few stable land masses.^{8, 10} With this environment in place, life arose and the process by which this occurred is unknown and under investigation.



Fig. 1.1 Artists rendering of the environment on the early Earth.

Image credit: NASA

The Miller-Urey experiment in 1952 propelled origins of life experimental research and made evident that biology is mainly a prolongation of chemistry.¹¹⁻¹² This experiment used an electric discharge to add energy to a system of prebiotically plausible gases that were available on the early Earth including H_2O , CH_4 , NH_3 , and H_2 . This experiment produced precursor molecules such as formaldehyde (CH_2O) and hydrogen cyanide (HCN), which can form amino acids or nucleobases, as well as amino acids (aspartic acid, glycine, alpha-amino-butyric acid, L-alanine, and D-alanine). Since 1952 this experiment has gone through numerous replications, with a protocol also developed

by Eric Parker et al. Parker used modern analytical methods to detect 23 amino acids in a racemic mixture for this experiment (e.g., L-valine, D-valine, and L-serine).¹³

Origin of life research may focus on the development of each macromolecule to form a protocell (*i.e.*, nucleic acids, polypeptides, polysaccharides and lipids), but before this, it can be deconstructed into: a) prebiotic synthesis b) polymerization and c) catalysis.¹⁴ Prebiotic synthesis research focuses on the formation of prebiotic molecules in the form of monomers and subsequently oligomers. Reactions that have been highly studied include the formose reaction, the formation of sugar molecules from formaldehyde, and nucleobase formation through HCN polymerization.¹⁵⁻¹⁶ In this model, polymerization relates to the formation of biopolymers and formation of macromolecules (*e.g.*, nucleic acids, lipids, proteins, and carbohydrates). Generally, polymerization reactions concentrate key monomeric molecules together through condensation reactions. Lastly, catalysis refers to the use of these polymers to catalyze reactions; examples of this include ribozymes as well as mineral surfaces.^{17, 18}

One area in origin of life research that has not been significantly explored to date is the role that mineral surfaces may have played in the formation of prebiotic molecules and in prebiotic polymerization. Solid surfaces are known to catalyze many industrial reactions.^{19,20} Given this knowledge and the prevalence of aqueous-mineral interfaces on the early Earth, this is an important area of investigation. The work presented here focuses on the incorporation of the element phosphorus into biochemical molecules. While recent experiments suggest that phosphorylation occurs in urea-rich solutions in contact with phosphate minerals, many questions remain about how phosphorus is released from the mineral. The mechanism of the dissolution process and mineral

transformations that have been observed post-reaction are not well understood.

Monitoring structural changes in the surface as the mineral dissolves may provide insight into these mechanisms. Moreover, developing a novel method for mineral surface analysis, supported by more established instrumental techniques, may have a wide range of applications.^{21,22}

1.2 Ubiquity and Biological Significance of Phosphorus

The pervasiveness of phosphorus in biological systems is evidence of its indispensable role in life. The biological significance of this element is illustrated by its presence in nucleic acids (*i.e.*, DNA and RNA), structural components (*i.e.*, cellular phospholipid membranes and apatite in bones), and metabolic molecules (*e.g.*, coenzyme A, glucose-6-phosphate, and ATP). As noted above, the presence of phosphorus in living organisms is primarily as a phosphate group: orthophosphate (PO_4^{3-}) or an organophosphate (*i.e.*, PO_4^{3-} bound to an organic molecule). Furthermore, its existence as an organophosphate may be subdivided into four categories: a) orthophosphate esters (*e.g.*, sugar phosphates, DNA, RNA through C-O-P bonds), b) reactive organophosphate molecules (*e.g.*, phosphocreatine through P-O-C bonds through carbonyl or vinyl groups), c) organic polyphosphates (*e.g.*, ATP, coenzyme A, and NAD through P-O-P bonds), and d) reduced phosphorus (*e.g.*, antibiotics through C-P bonds).^{14,23} In fact, 44% of metabolic biological molecules contain phosphorus.²⁴

Properties of the phosphate group (PO_4^-) include its ability to form bonds (*i.e.*, bridging formation, C-O-P linkage in DNA) while maintaining its charge.^{25,26} By maintaining its negative charge, phosphate aids in the stability of phospholipid membranes by enhancing a molecule's solubility and preventing diffusion of cell

contents through amphiphilic membranes. Furthermore, this charge restricts hydrolysis or break down of bonds by water (oxygen acts as a nucleophile and seeks an electrophile, and phosphorus has a localized negative charge), making important biopolymers such as nucleic acids (*i.e.*, DNA and RNA) more stable.²⁶⁻²⁸

1.3 The Phosphate Problem

Despite the presence and significance of phosphate in biochemistry, there are several challenges regarding its initial incorporation into life. In origin of life research, this is known as the “phosphate problem.” In particular, the phosphorylation mechanism for the formation of the earliest organophosphate compounds is under investigation and there are three proposed models: a urea-catalyzed mechanism, an organocatalysis mechanism, and a phosphate-intermediate mechanism.²⁹ In a urea-catalyzed reaction, urea is believed to act as a catalyst to form an intermediate comparable to a carbodiimide crosslinking.^{30,31} However, current research by Burcar *et al.* and work by Schoffstall *et al.*, suggests that phosphorylation occurs mainly via organocatalysis with a urea-catalyzed reaction having a minor role.^{22,32,33} Organocatalysis assumes hydrogen bonding between hydrogens in urea and the oxygen in phosphate. The oxygen from phosphate gets extracted leaving a metaphosphate, which is attacked by a nucleophile (the organic compound to be phosphorylated *e.g.*, nucleosides such as thymidine and uridine) to produce an organophosphate.³³ A phosphate intermediate pathway would also utilize urea, but a reactive phosphate intermediate forms. Despite numerous experiments, this reactive phosphate intermediate has not been observed experimentally. Below is a generic reaction for the phosphorylation of an organophosphate with H_2PO_4^- being the reactive

species at pH 7 and inducing phosphorylation. (*n.b.*, The primary form of phosphate is highly pH dependent.³⁴)



The first major challenge associated with phosphorylation of an organic molecule relates to the so-called water problem.^{35,36} The equation above shows the release of water upon phosphorylation (*aka* phosphate condensation).¹⁴ An abundance of water in the environment pushes the equilibrium toward the unphosphorylated reactant rather than the phosphorylated product by Le Chatelier's principle. Therefore, phosphorylation cannot readily occur in aqueous environments, which were abundant on the early Earth (as mentioned in Section 1.1) and widely considered the most likely place for life to have emerged. Unfortunately, phosphate condensation reactions in aqueous solution are endergonic and non-spontaneous (*e.g.*, the phosphorylation of ADP to form ATP has a $\Delta_r G^\circ = +30.5$ kJ/mol and pyrophosphate $\Delta_r G^\circ = +42$ kJ/mol).¹⁴

Adding to the water problem is the low availability of phosphorus in solution. Unlike the other five elements essential for life (*i.e.*, C, H, O, N, and S), which exist in gaseous form or in a volatile liquid, P is trapped primarily in mineral sources. An exception is phosphine gas (PH₃), which is not believed to have had an appreciable abundance on the early Earth.³⁷ The most abundant natural sources of phosphorus on the early Earth are believed to be phosphate minerals, which are highly insoluble in water.^{38,39} The insolubility of phosphate minerals creates a challenge to understanding the most likely prebiotic scenario of life evolving in water (*i.e.*, that life evolved in a “warm little pond”).⁴⁰ Additionally, phosphate minerals commonly occur on the surface of stony meteorites and carbonaceous chondrites, with 15 phosphate mineral species recorded;

carbonaceous chondrites, such as the Murchison meteorite contain various organic molecules, such as amino acids, nucleobases, and phosphonic acids and may be useful in studying the origins of life.⁴¹⁻⁴⁵

The significance of phosphonic acids on the surface of the Murchison meteorite may provide a link between phosphite (PO_3^{3-}) as a prebiotic phosphorus source.³⁹ Phosphite has a solubility 1000 times higher compared to apatite (mineral with phosphate rather than phosphite).⁴⁶ Phosphites as well as reduced phosphorus mineral sources will be discussed in Section 1.5. Prebiotic sources of phosphorus could have included minerals composed of phosphate and phosphide groups, including minerals on Earth and meteoritic sources.

1.4 Initial Approaches to Understanding Prebiotic Phosphorylation

To investigate the phosphate problem, a prebiotic phosphorus mineral source needs to demonstrate a plausible phosphorylation route. Previous research has investigated scenarios to overcome the challenges of organophosphate formation under prebiotic conditions. The use of condensing agents, energetic phosphates, and lowered water activity (dehydration) have been explored (*e.g.*, see Ref 14 and references therein).

In previous experimental origin of life research, phosphorylation of organic compounds has been induced through condensing agents such as imidazoles, thioacetate, and cyanate compounds.⁴⁷⁻⁵⁵ These agents allow for the formation of a reactive phosphorylated intermediate, usually an energetic species that is susceptible to reacting.¹⁴ However, the yields can be low, there are numerous side reactions, and the low pHs may degrade biological molecules, specifically nucleic acids.^{56,57,26}

Energetic phosphates or condensed phosphates are polyphosphates, which have a stable P-O-P bond.⁵⁵ Advantages to these polyphosphate sources are: 1) their high solubility compared to orthophosphate (PO_4^{3-}), and 2) phosphate is a better leaving group than water, allowing for higher phosphorylation yields.^{58, 26} Since the leaving group is no longer water than phosphorylation yields increase because the need for chemical equilibrium to shift to the reactants is no longer present. However, dehydration is needed to initially synthesize polyphosphates.⁵⁹⁻⁶¹ Several researchers have investigated the conversion of orthophosphate into these polyphosphates, such as triphosphate, trimetaphosphate, pyrophosphate, and cyclotrimetaphosphate (cTMP).⁶²⁻⁷⁰ CTMP and trimetaphosphates exhibit high phosphorylation yields; High yields are obtained specifically when ammonia and ammonium are present.^{71, 72} Despite phosphorylation occurring more readily with polyphosphates, an issue is the scarcity of these sources on the early Earth. Researchers showed the formation of these compounds in a volcanic environment, with the formation of pyrophosphate and triphosphate.⁷³⁻⁷⁵ Additional research has investigated phosphorylation reactions using minerals containing KH_2PO_4 and NaH_2PO_4 as abiotic sources of phosphorus.⁷³⁻⁷⁶ However, potassium and monosodium phosphate are highly soluble in water and were most likely not present on the early Earth.⁴⁴ Thus, the prebiotic plausibility of phosphate minerals needs to be considered. Phosphate minerals that have been preserved in the geological record from the Hadean eon on Earth include hydroxyapatite (HA), $\text{Ca}_{10}(\text{PO}_4)_6(\text{OH})_2$ and whitlockite, $\text{Ca}_9(\text{MgFe})(\text{PO}_4)_6\text{PO}_3\text{OH}$, which have low solubility of 10^{-6} M.^{18, 77, 78} Recent work has shown that the inventory of phosphate minerals on the early Earth may have included higher amounts than initially suspected of soluble phosphate minerals such as struvite and

newberyite in subaquatic environments.²² Modeling suggests they actually may have been more abundant than apatites under the conditions of the early Earth. However, they are not as stable in the long term, making it unlikely that they would have been preserved in the rock record.

Phosphorylation of organic molecules may also be promoted through lowered water activity by dehydration. Dehydration experiments include experiments that increase temperature or use solvents with lowered water activity; the former will be discussed in detail in the next section. Several dehydration experiments focused on increasing the temperature of phosphate dissolved with organic compounds to target the water problem. and use temperatures These experiments were prominent in the 1960s and focused on high temperatures from 120 to 160° C.^{79, 80} While the conditions did cause phosphorylation (e.g., the formation of nucleotides from nucleosides).^{81,82} the experiments revealed deterioration of reactants and they depended on unlikely phosphate sources.²⁶

1.5 Twenty-first Century Approaches to Understanding Prebiotic Phosphorylation

More modern approaches to overcome the challenges associated with phosphorylation have investigated lowered water activity through dehydration and the use of alternative solvents such as urea and formamide, non-aqueous solvents, and deep eutectics. Several recent experiments have also used reduced phosphorus sources rather than phosphate minerals, which will be discussed below.⁸³⁻⁸⁵ Here, we refer to alternative solvents as any solvent that has a low water activity, either because the effective or the actual concentration of water in the solvent is low. Major advantages of alternative solvents, are increased phosphorylation yields, since water activity is decreased and

prebiotic phosphate minerals are also highly insoluble in water.⁸³ Formamide was one of the earliest alternative solvents used in 1976 and is prebiotically plausible as a product of HCN hydrolysis formed from ammonia and carbon monoxide.⁸⁶⁻⁸⁹ In the presence of formamide, phosphorylation of nucleosides and glycerol has been observed, with nucleotides produced in yields of 6-59%.⁹⁰⁻⁹⁴ However, issues with some of these results pertain to the prebiotic plausibility of the phosphate minerals used (*i.e.*, copper and lead phosphate minerals) as well as the use of pure formamide. Other alternative solvents include deep eutectics, which are mixtures that evaporate at a consistent ratio when heat is applied. Urea and choline chloride (2:1 ratio) is a deep eutectic solvent which was shown to phosphorylate a wide range of molecules, nucleotides, glycerol, and glucose with phosphorylation yields of 15-99% with a variety of phosphate sources (*i.e.*, struvite, monetite, and NaH_2PO_4).⁹⁵ A deep eutectic mixture of choline chloride and glycerol (1:2.5 ratio) has also produced organophosphates.⁹³ However, the prebiotic plausibility of choline chloride is questionable and choline is also phosphorylated during the reaction, limiting the total phosphorylation.

Recent research has investigated a deep eutectic composed of urea, ammonium formate, and water (UAFW in a 1:2:4 ratio), which has been shown to form formamide when heated for several days.³² The components of this solvent are prebiotically plausible, since urea is produced when ammonium cyanide encounters sunlight, and ammonium formate is produced as HCN is hydrolyzed.^{96,97} Phosphorylation of nucleosides and glycerol in the UAFW is observed with various phosphate sources (*e.g.*, hydroxyapatite, struvite, and disodium phosphate) and yields increase as magnesium sulfate is added (MgSO_4) and the system is heated to 85°C.³²

While a large focus has been on phosphates as the starting material for phosphorylation, reduced phosphorus and energetic phosphorus minerals have also been considered. Phosphate minerals contain phosphorus with an oxidation state of +5, and a majority of terrestrial surface phosphorus has this oxidation state.⁹⁸ There are sources of phosphorus with lower oxidation states; examples of these reduced phosphorus sources include: phosphite, hypophosphite, phosphine, and phosphide (see Fig. 1.2). A compound is a reduced phosphorus source, when the charge of phosphorus is less than +5. While reduced phosphorus sources were speculated to be significant in origin of life chemistry, it wasn't until analysis of the Murchison meteorite showed the presence of phosphonic acids and organophosphonates that a source was identified.^{38,45} The Murchison meteorite is a carbonaceous chondrite containing amino acids, carboxylic acids, alkyl sulfonic acids, and phosphonic acids. Eight alkyl phosphonic acids with concentrations of 9 nmol/gram and orthophosphate at 25 μ mol/gram were identified. This was a significant discovery because of the presence of phosphorus in a reduced oxidation state (+3) as phosphonic acids or organophosphonates, which have a P-C bonds.⁴¹ Phosphorus in a reduced oxidation state (+3) as phosphonic acids or organophosphonates, which have a P-C bond.⁴⁵

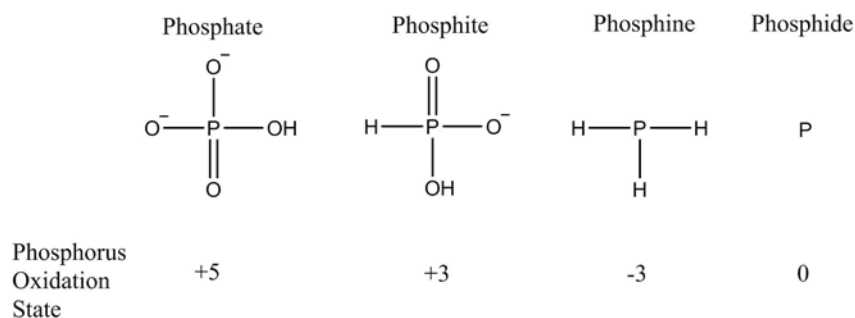


Fig. 1.2 Structures of common phosphorus species are depicted.

Additionally, plausible prebiotic minerals containing phosphide groups may have also been sources for phosphorylated biological compounds. Phosphides are commonly found on meteorites and to a lesser extent in comets and on interplanetary dust particles.^{99,100} The extraterrestrial mineral schreibersite, $(\text{Fe,Ni})_3\text{P}$ is an example of a phosphide mineral; the oxidation state of phosphorus is about -1 compared to +5 in orthophosphate.¹⁰¹⁻¹⁰³ The presence of schreibersite on Earth is suggested by the concentrations of phosphite found in carbonate rocks, which date to 3.52 billion years as well as its natural occurrence in a few locations on Earth, such as Disko Island.^{84,104,105} Furthermore terrestrial phosphides have recently been identified in Israel and Jordan near the Dead Sea, Levant.¹⁰⁶ The reaction of schreibersite with water produces dissolved phosphorus oxyanions (*e.g.*, pyrophosphate $\text{P}_2\text{O}_7^{4-}$, phosphite PO_3^{3-} , and hypophosphite $\text{P}_2\text{O}_6^{4-}$) and researchers have phosphorylated nucleosides into nucleotides with this mineral under moderate temperature (20-85°C) and basic pH (6.5-8).¹⁰⁷⁻¹⁰⁹

Phosphite species produced by schreibersite are significant in their increased solubility by nearly 1000 times, while hypophosphite is 10^6 times more soluble (when

divalent cations are present) compared to phosphates.²⁶ Furthermore, phosphite species may include metal phosphites in the form of $MHPO_3$ ($M = Ca^{2+}, Mg^{2+}, Fe^{2+}$). Phosphite species may be oxidized by hydrogen peroxide, H_2O_2 in the presence of Fe^{2+} to form polyphosphates (*i.e.*, triphosphate and trimetaphosphate) via the Fenton reaction. The condensed phosphates formed by the Fenton reaction are much more reactive in water than orthophosphate (PO_4^{3-}). Moreover, this reaction is more versatile because it can be performed under a wider range of pHs and it produces appreciable yields even at lower concentrations.^{26,108,110} Additionally, phosphites may also react with organic compounds, including glycerol phosphates.^{111,112,86}

1.6 Understanding Prebiotic Chemistry Through Mineral Surfaces

Surface chemistry is significant for its applications in a variety of processes, of notable importance is heterogeneous catalysis (see Fig. 1.3). 90% of industrial material output including fertilizers and plastics are produced by heterogeneous catalysis; examples include the Haber-Bosch process for the synthesis of ammonia and hydrogenation (*e.g.*, production of saturated fats and oils).^{113,114,115} Interactions on surfaces are crucial for industrial systems as well as processes such as soil weathering. Surface interactions will be the main focus of this project, specifically interactions on a solid surface between liquid-solid interfaces. A general review of solid and mineral surfaces will be given below.

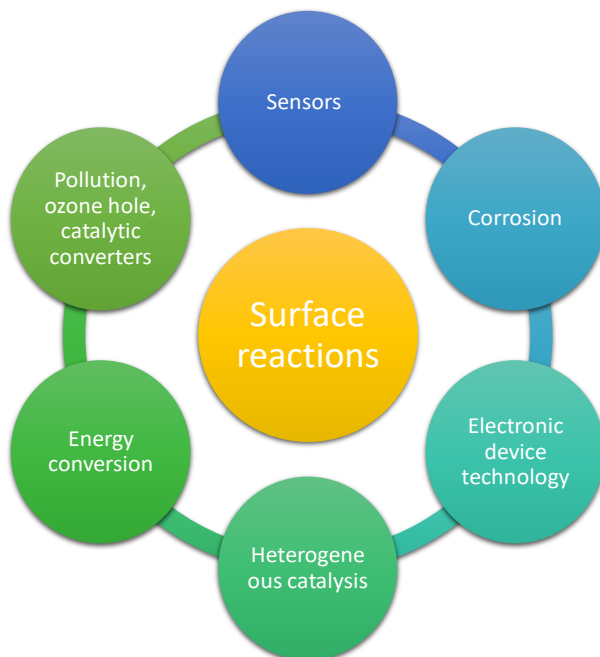


Fig. 1.3 Significance of surface reactions in different fields. Redrawn and adapted from Ref 113.

1.6.1 Crystalline vs. Mineral Surfaces

To have a basic understanding of the physical and chemical properties of a solid surface, the atomic geometry or physical arrangement of its atoms needs to be studied (Fig. 1.4). While ideal surfaces are flat and have no defect sites, real single crystals have defect sites. In contrast to single crystals, minerals have many more defect sites. These defect sites affect the reactivity of materials.¹¹⁶⁻¹¹⁹ Surfaces are affected by their unfavorable thermodynamics, unlike the bulk of a material; surfaces have a positive free energy of formation, caused by bond breakage and reduction in coordination number.^{120,121} This unfavorable positive free energy is minimized by surface atom rearrangement to decrease the surface area (*e.g.*, by relaxation and reconstruction).¹²¹ Nonetheless, there will be charge density at the surface in so-called dangling bonds. These are orbitals that were previously used to bind to the bulk material, before there was

a surface. The stability of a surface can be reshaped by the dangling bond surface states (*i.e.*, anion and cation derived from the electron-hole pairs); a surface is autocompensated when the charge on the surface is neutral and stable.¹²² Once the surface is autocompensated, the atomic arrangement of the surfaces may undergo relaxation, change in the interlayer spacing between the surface layers as compared to the bulk material or reconstruction, change in symmetry for the surface, creating different symmetries between the surface and bulk.^{120,122} The extent of relaxation or reconstruction depends on each individual surface and the degree to which its rehybridized. The surface dangling bond charge density may be rehybridized due to the low atomic coordination of the surface. This rehybridization may induce charge transfer between surface atoms and lead to new bond formation (*i.e.*, surface dimerization) or bond formation between surface and adsorbed molecules (*i.e.*, adatoms).¹²² In general, surfaces undergo autocompensation and its atomic geometry is dependent upon rehybridization and surface strain, to reduce its free energy (surface tension).¹²²

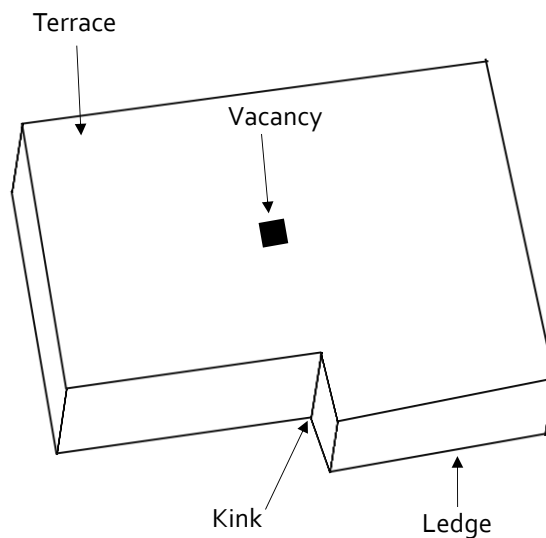


Fig. 1.4 Schematic representation of surface defects. Adapted from Ref. 120.

Surface chemistry is complex, as mentioned above various surface defects are present on solid surfaces, these allow for multiple types of binding sites. This may increase the complexity in analysis, an additional layer of complexity stems from symmetry- breaking occurring on a solid-gas or solid-liquid interface. Mineral surfaces are more complex than real crystal or metal surfaces, as most minerals have irregular surfaces and are generally not ideally planar (examples of mineral surfaces planar at the atomic scale include [001] planes of micas and chlorites).¹²³ Minerals may not always have repeating two-dimensional surfaces, some may be amorphous and an additional factor is the point of zero charge (pzc, different for each mineral).¹⁸ The pzc indicates the pH at which the mineral surface is neutral, pH values above the pzc create an environment for cationic surface reactions and adsorption, likewise pH values below the pzc do the same with anions.¹²⁴ The pzc was not taken into account for this project due to

time constraints; however, this is an additional factor of complexity when dealing with mineral surfaces.

Minerals promote reactions and may have been key for prebiotic chemistry. Origin of life researchers recognized this as early as 1940s.¹²⁵ Porous minerals contain a variety of defect sites, which allows for concentration of molecules but adsorption is also dependent upon pH.¹²⁶ Macromolecules essential for life include nucleic acids, amino acids, and sugars; minerals serve to concentrate and assemble these monomers so that they may assemble and polymerize, rather than degrading in an aqueous environment.¹²⁷⁻¹²⁹ Research on amino acid assembly has shown small protein formation on clays through evaporation, various other minerals have also been studied in relation amino acids (*e.g.*, rutile, calcite, hematite, montmorillonite, and pyrite).¹³⁰⁻¹³² Mineral surfaces may also have higher enthalpies of rehydration, allowing condensation reactions to occur more readily, and pores provide protection from UV radiation.^{133,134}

Phosphorus-bearing minerals that were prevalent on the early Earth include hydroxyapatite (HA) and whitlockite, these minerals have low solubility and unfavorable thermodynamics with aqueous solutions.⁴⁴ Current research³² has shown that hydroxyapatite can interact with solutions of prebiotic molecules that have lowered water activity, such as urea rich solvents composed of urea, ammonium formate and water or UAFW-with additives (*e.g.*, magnesium sulfate). Additionally, this research suggests that phosphorylation might occur through surface mediated processes, as HA can be used to phosphorylate; however, this does not directly correlate with an increase in solubility of orthophosphate from the mineral.³² Scenarios with urea-rich solvents take into account lowered water activity and allow for phosphorylation to occur more readily, since life

likely originated in an aqueous environment and water is a product of phosphorylation (as shown in Eq. 1.). This high water activity can be mitigated with the use of alternative solvents and advantages of these solvents are lowered water activity while maintaining a fluid environment. Additionally UAFW forms a fourth component, formamide, upon heating.³² The focus of this thesis is based on phosphates interacting with non-aqueous urea-rich solutions (UAFW). The purpose of our research project is to develop hydroxyapatite thin films that are conducive to surface analysis and can be used to investigate the activation of phosphorus in mineral surfaces and surface-mediated interactions in mineral transformation.

CHAPTER 2. EXPERIMENTAL METHODS

2.1 Methodology Overview

Most surface sensitive techniques used to study interfaces require a conductive backing. A concern in surface chemistry is the range of instrumentation possible for analysis. For example, scanning tunneling microscope (STM) and x-ray photoelectron spectroscopy (XPS) instruments are selective for conductive materials and insulators/low heat conductors are difficult to analyze, as there is a charge build up, limiting analysis.¹³⁵⁻¹³⁷ An alternative solution to overcome this issue is through the use of thin film samples deposited on a conductive backing; light can adequately reflect off the surface and charge does not buildup.¹³⁸

Thin hydroxyapatite (HA) films will be synthesized on metal substrates (*i.e.*, copper and gold) using electrochemical deposition and characterized prior to reaction by polarization modulation-infrared reflection absorption spectroscopy (PM-IRRAS), scanning electron microscopy (SEM), and energy-dispersive x-ray spectroscopy (EDX). These methods provide information about the surface, surface morphology, and the elemental composition, respectively. These techniques will be used to verify that HA has been synthesized and assess its initial composition.

Films will then be reacted with solutions containing mixtures of prebiotic solutions such as urea, ammonium formate, and water (UAFW) at room temperature (298 K). Structural changes as a function of time will be monitored using PM-IRRAS at one hour intervals for a total of four hours. Control experiments with binary solutions

(*e.g.*, urea/water and ammonium formate/water) and water will be used to help decipher the spectra for UAFW. Post reaction analysis with SEM and EDX will support these time dependent studies to understand mineral corrosion, and supernatant analysis by nuclear magnetic resonance spectroscopy (NMR) will investigate the release of phosphate into solution. Overall stages and methodology are depicted in Fig. 2.1.

Two primary research questions arise from this project: “Can ultrathin phosphate mineral films be developed?” and “Can molecular interactions of urea rich solvents on HA be probed and what role do individual components of the solvent play in mineral dissolution?” Developing ultrathin phosphate mineral films for surface analysis suggests films need to be robust and be similar enough to have reproducible results for each reaction. Mineral dissolution can be monitored by characterization pre- and post-reaction, and molecular interactions can be probed by observing structural changes with time and through control experiments.

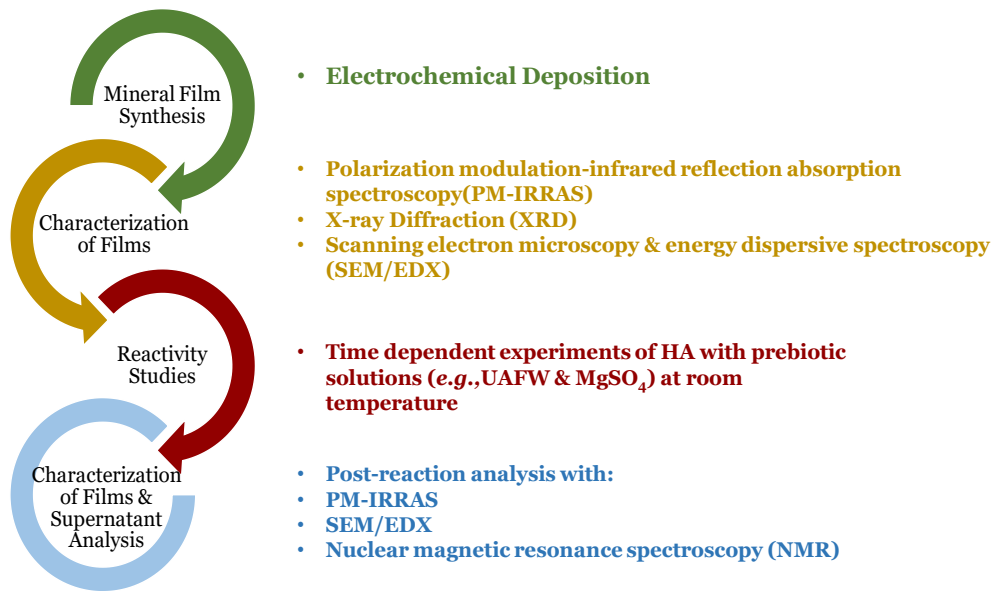


Fig. 2.1 Schematic showing the stages and methodology of this project.

2.1 Synthesis of Hydroxyapatite: Electrochemical Deposition

HA was chosen as our model phosphate mineral since procedures for synthesizing thin films of this material via electrodeposition have already been developed. HA is a bioceramic and found in bone and tooth enamel.¹³⁹ Previous research has focused on developing implants for orthopedic and dental procedures, allowing for established synthesis methods of this mineral to be accessible and easily modified for this study.¹⁴⁰⁻¹⁴⁴ The aim of this project is to study the surface of hydroxyapatite and the role of mineral surfaces in phosphorylation of small biological molecules. Since the focus of this study is surface analysis, the synthesis method needs to be suitable for this analysis, meaning desired characteristics of HA films need consideration.

Electrochemical deposition of HA films has been chosen for several reasons. First, this method allows for growth on mirror-finished samples that are highly reflective for infrared light. Other techniques such as hydrothermal and sol-gel processes were considered, but they require defect sites for initial nucleation and film growth, while electrochemical deposition does not depend heavily on defect sites.¹⁴⁵ Initially a hydrothermal method was used to prepare HA films by Ethan Ertell from the Poyraz laboratory, but this technique was not conducive for infrared surface analysis. Additionally, electrochemical deposition results in a homogeneous composition and customizable thickness. Additionally, it is cost efficient compared to synthesis using vacuum deposition methods (*e.g.*, plasma enhanced chemical vapor deposition or physical vapor deposition).¹⁴⁵

Electrochemical deposition (*i.e.*, electrodeposition) is a synthesis technique used to deposit materials on conductive substrates; metal plating is a common example. This

process occurs in an electrochemical cell, which may have two or three electrodes. A three-electrode system allows for better accuracy. The primary components include a working electrode (WE), counter electrode (CE), reference electrode (RE), and an electrolytic solution.¹⁴⁶ The working electrode is the electrode where the material of interest is deposited. The counter electrode or secondary electrode serves to balance the reactions occurring at the WE. For example if reduction occurs at the WE, oxidation of the same magnitude occurs on the CE. The CE needs to allow electron transfer reactions to occur more readily and be inert, to minimize interference with the WE. The reference electrode serves to maintain a consistent potential and should have little to no current passing through it.¹⁴⁷ In electrochemical reactions, a charge exchange occurs between chemical species and an electrode. An example of a simple electrode reaction is electron transfer, including oxidation at the anode and reduction at the cathode. Reactions that involve electron transfer occur when species are close to the electrode surface; the transformation of reactant to product must be constant and implies addition and removal of the reactant and product in combination with electron-transfer.¹⁴⁷ Species undergo a charge transfer and are also transferred to the electrode. Three types of mass transport include diffusion, migration, and convection.¹⁴⁸

For electrodeposition of HA, a potentiostat is used to control the difference in potential between the WE and CE. (An Interface 1010 B Potentiostat/Galvanostat/ZRA was used for this study.) The potentiostat is used in a potentiostatic mode to control the potential by modifying the current. The deposition can be run in a pulsed mode (where the potential is varied as a square wave) or through linear sweep voltammetry (potential is increased linearly from one defined value to another). Alternatively, cyclic

voltammetry may be used; this technique ramps the potential of the WE through a range of voltages, starting and ending at the same value.¹⁴⁶

The experimental setup for electrodeposition was developed with the help of Dr. Altug Poyraz. The electrochemical cell components for the synthesis of HA were: platinum for the CE, gold for the WE, saturated calomel electrode (SCE) for the RE, and a molar (electrolytic) solution of 0.0168 M $\text{Ca}(\text{NO}_3)_2 \cdot 4\text{H}_2\text{O}$ and 0.0100 M $\text{NH}_4\text{H}_2\text{PO}_4$, as illustrated in Fig. 2.2.

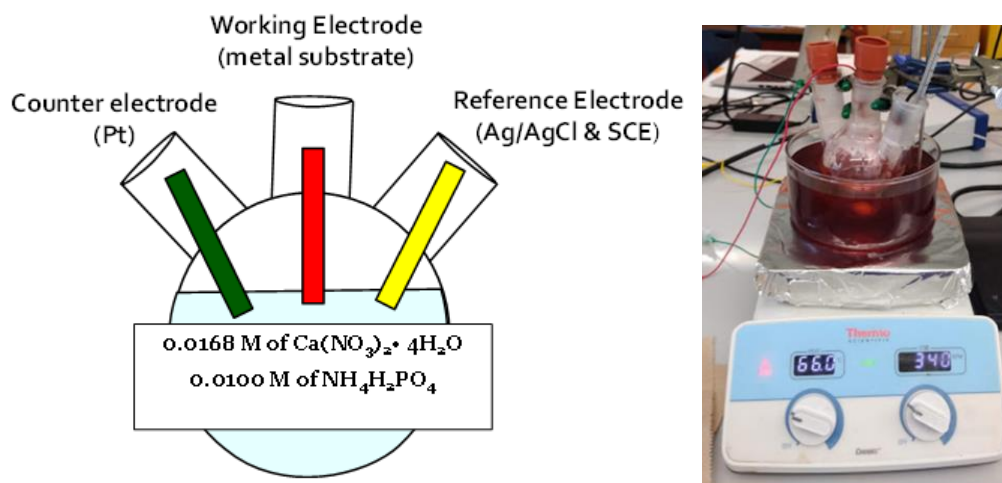


Fig. 2.2 Schematic (left) and experimental setup (right) for electrochemical deposition.

The concentrations of the molar solutions were determined to ensure a 1.67 stoichiometric ratio corresponding to the ratio of Ca to P in HA. Cyclic voltammetry was the technique chosen for electrodeposition, a voltammogram is presented in Fig. 2.3. The potential used for the gold substrate was 0.0 V to -1.6 V and the molar solution was pH adjusted to ~ 5.7 . To create ultra-thin films, the scan rate (mV s^{-1}), number of cycles, temperature, and concentration were adjusted. The working principle for electrochemical deposition is based on two electrical currents, one produced by the ions in the electrolytic

(molar) solution and the other produced by the external circuit. As the potential of the electrode decreases, species in the electrolyte solution are reduced, which increases the current by creating more phosphate and hydroxide anions in solution; possible reduction reactions are listed below (see Eqs. 2.1-2.3).¹⁴⁷ These ions react with free calcium cations to form HA on the working electrode.

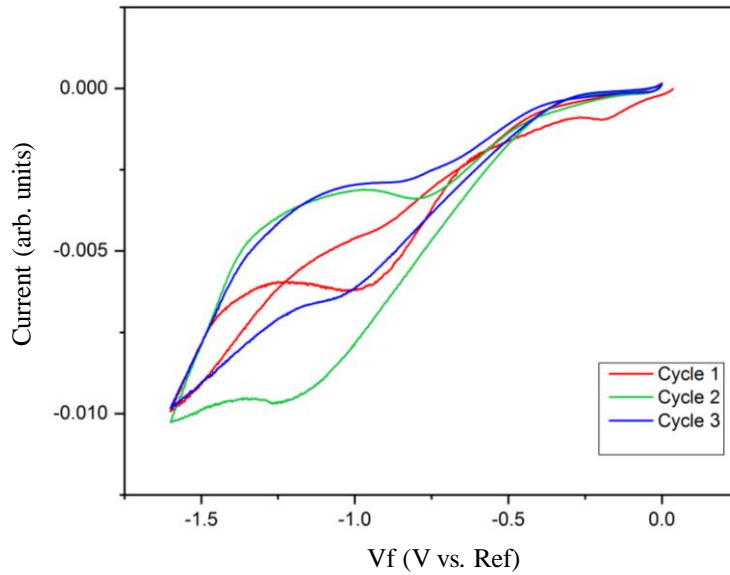
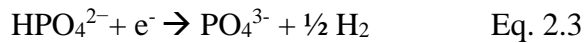
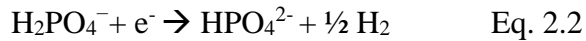


Fig. 2.3 Cyclic Voltammogram Sample 26 parameters: 59–60 °C, 25 mV s⁻¹, 10 mA, 0.0V to -1.6V, pH: 5.814, cycles: 3.



The thickness of the films increases depending on the concentration of the electrolytic solution used; however, this is limited by the rate of diffusion. Film thickness is also controlled by temperature. The temperature affects film porosity, the diffusion rate of ions, and the solubility of HA. With increasing temperature the solubility of HA

decreases, which promotes deposition on the WE. After a certain maximum temperature is reached, film thickness does not continue to increase but to decrease, due to increase of phosphate and hydroxide ions that diffuse and form HA in solution rather than on the surface of the electrode.¹⁴⁰

2.2 Reflection Absorption Infrared Spectroscopy (RAIRS)

2.2.1 Theory of RAIRS

Reflection-absorption infrared spectroscopy (RAIRS) or infrared reflection-absorption spectroscopy (IRRAS) is a type of optical spectroscopy that focuses infrared light onto a reflective and conductive substrate (*e.g.*, metals), giving information about the surface structure (*i.e.*, functional groups and coordination of adsorbed species). This technique relies on the vibrational motion of molecules and their interaction with infrared light.

Within molecular orbitals, there are three types of energy levels: rotational, vibrational, and electronic. Infrared radiation is responsible for probing molecular vibrations. For a vibrational mode to be infrared active, there has to be a net change in dipole moment with the motion of the molecule's vibration. This implies a difference in electronegativity as well as the symmetry of a molecule in motion, which may serve to enhance or cancel out a dipole moment. The optoelectric theory behind RAIRS relies on this gross selection rule (*i.e.*, a net change in dipole moment as the molecule vibrates). However, it is also affected by the reflective surface, which is most commonly a metal.¹⁴⁹

The incoming infrared light striking the surface has two components, s- and p-polarization. These components are defined by their relation to the plane of the incident and reflected light. (This plane is represented in red in Figure 2.4; s- is perpendicular to

the plane and p- is parallel to the plane.) Fig. 2.4 illustrates E as the electric field vector of the incident (E^i) and reflected (E^r) light. The incident s-polarized light (E_s^i) undergoes a phase shift of approximately 180° such that the reflected s-polarized light (E_s^r) will destructively interfere with the incident s-polarized light and not be detected. In contrast, the incident p-polarized light (E_p^i) constructively interferes with the reflected p-polarized light, allowing for an increased electric field. Therefore, the p-polarized light gives information about the surface, due to its constructive interference.^{149,150}

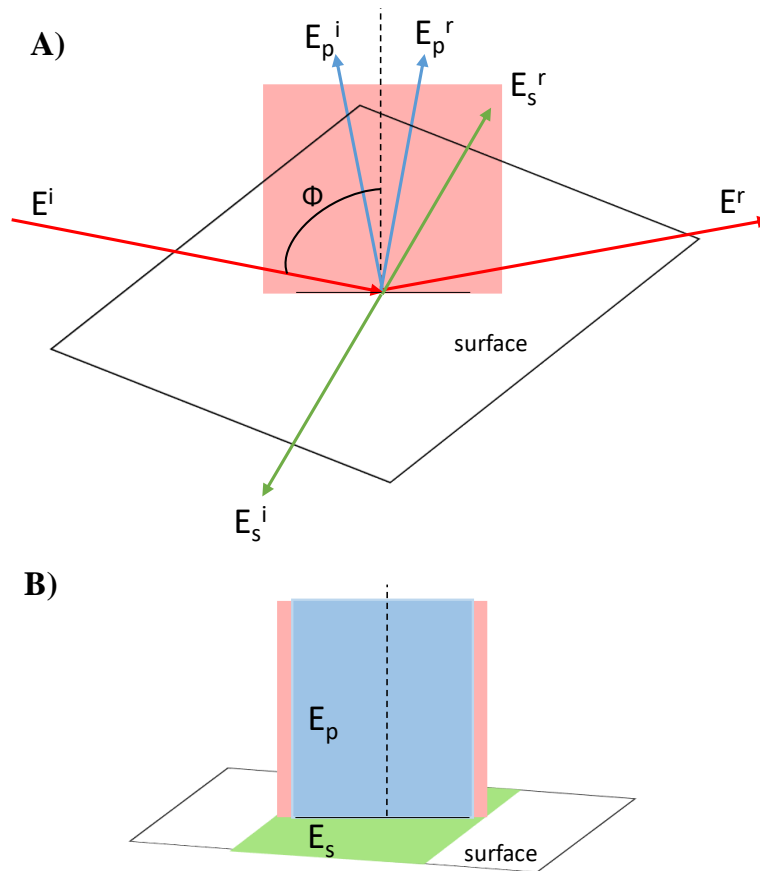


Fig. 2.4 Electric field vectors for p-polarized and s-polarized light in relation to the surface, where Φ represents the incident angle. The bottom schematic illustrates that p-polarized light (blue) is parallel to the incident and reflected plane (red), while s-polarized light (green) is perpendicular to this plane.

P-polarized light may be broken down into \perp perpendicular and \parallel parallel components. The perpendicular component contributes a higher amplitude compared to the parallel component, when a grazing angle of incidence is used. Both electric field sums of s- and p- are represented in the equations below, where δ represents a phase shift caused by reflection, θ is the phase of the light, and r is a reflectivity coefficient. Different metals have varying reflectivity in the infrared region, some yielding higher signal intensities. Varying the incident angle (Φ or φ) also changes the signal intensity caused by a higher amplitude of the electric field, as illustrated in Fig. 2.5. In Fig. 2.5 the p-polarized light is partitioned into perpendicular (\perp) and parallel (\parallel) components and absorption intensity is plotted as a function of the incident angle, where E_p^\perp / E_p^i represents the amplitude of the perpendicular electric field vector and $(E_p^\perp / E_p^i)^2 \sec\Phi$ represents the total absorption intensity. As the incident angle increases, the absorption intensity and amplitude of the electric field increases; however, once the incident angle approaches 85° and greater, both the amplitude and absorption intensity drastically decrease, caused by destructive interference. Listed below are Eq. 2.4 and Eq. 2.5, where the former represents the electric field vector for s-polarized light, and the latter represents the electric field vector for the perpendicular and major component of p-polarized light.^{149,150}

$$E_s = E_s^i [\sin \theta + r_s \sin(\theta + \delta_s)] \quad \text{Eq. 2.4}$$

$$E_p^\perp = E_p^i \sin \varphi [\sin \theta + r_p \sin(\theta + \delta_p)] \quad \text{Eq. 2.5}$$

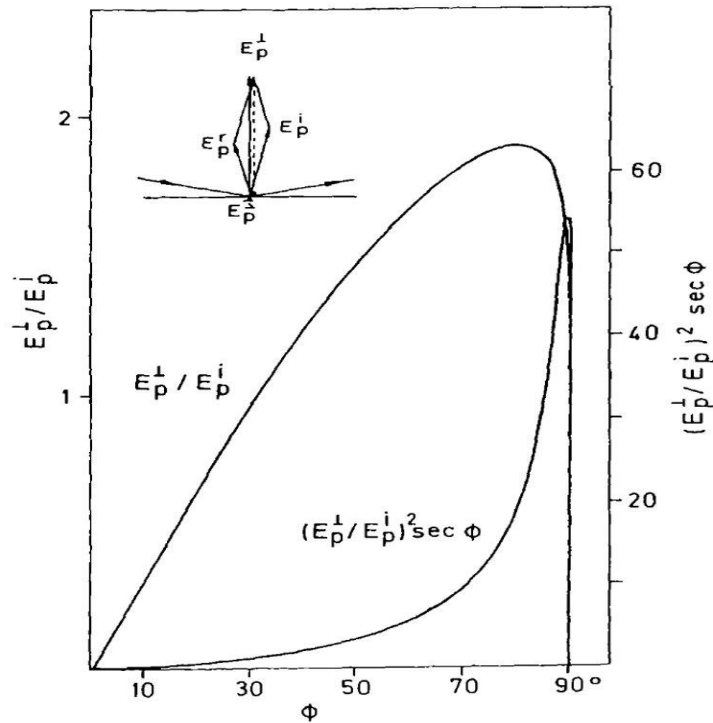


Fig. 2.5 E_p^\perp / E_p^i represents the amplitude of the perpendicular electric field vector and $(E_p^\perp / E_p^i)^2 \sec \phi$ represents the total absorption intensity. As the incident angle increases the absorption intensity and amplitude of the electric field increases to a certain extent. The small schematic on the top left illustrates the major contribution of the perpendicular component compared to the parallel component of p-polarized light. Obtained and used with permission from Ref. 150.

Image dipole theory, represented in Fig. 2.6, explains why only vibrational motions with a dipole moment perpendicular to the plane of the surface can be observed by RAIRS. When infrared light interacts with molecules on the surface, the dipole moment induced by this vibration creates an image dipole within the conductive surface. Image dipoles are created by the rearrangement of electrons near the surface of a conductive material such as a metal. If a dipole moment is perpendicular to the surface, then the image dipole will also be perpendicular; this will amplify the infrared signal

(Fig. 2.6A). If the dipole moment is parallel to the surface, then the image dipole will also be parallel, with identical magnitude and opposite direction. There will be no net change in dipole moment because the vectors cancel.

Experimental studies performed with IRRAS depend solely on p-polarized light and may be normalized by the metal substrate. Reflectivity of the p-polarized light is measured by an absorbance or transmittance spectrum, as described in Eq. 2.6.^{149,151,152} In Eq. 2.6, R_p represents p-polarized reflectivity, d corresponds to the film of interest on a metal surface, 0 corresponds to the bare substrate (*i.e.*, the underlying metal), and A corresponds to absorbance of infrared light.^{151,152}

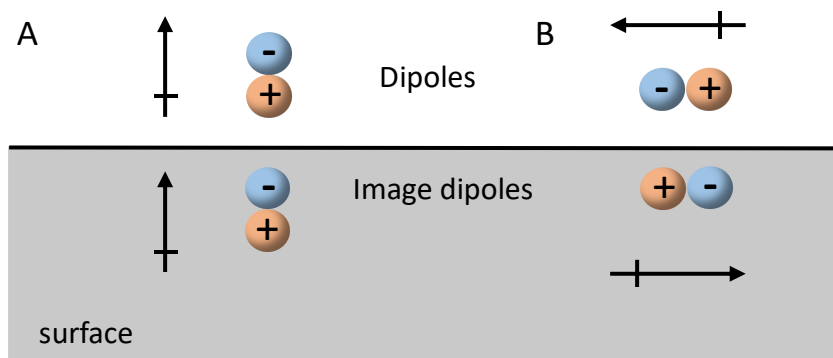


Fig. 2.6 Image dipole theory illustration. A) perpendicular dipole and signal amplification B) parallel dipole and no net signal.

$$A(d) = \frac{R_p(d)}{R_p(0)} - 1 \quad \text{Eq. 2.6}$$

2.2.2 Theory of Polarization Modulation-Infrared Absorption Reflection Spectroscopy (PM-IRRAS)

Greenler was the first to establish IRRAS through experiment and theory by investigating solid-solid interfaces.¹⁵² This technique can be enhanced through

polarization modulation to minimize contributions from fluid phases when analyzing liquid-solid and gas-solid interfaces. PM-IRRAS is often uses a photoelastic modulator (PEM) to rapidly alternate the incident light between s- and p-polarizations.^{151,153} However, for these experiments the polarization of light was modulated manually. As referenced in the previous section, only the p-polarization of light gives information about the surface but s-polarization gives information about the gas or liquid phase above a solid surface. By ratioing p- and s-polarized light (see next section) information about adsorbates is acquired.

2.2.3 Experimental Implementation

2.2.3.1 Optical Alignment

The experimental setup for polarization-modulation infrared reflection-absorption spectroscopy (PM-IRRAS) is based on an optical system, designed by Katerina Slavicinska and T.J. Beckman from the Abbott-Lyon Laboratory. Optical layouts for PM-IRRAS are limited by the FTIR spectrometer sample compartment size, since the infrared light beam must be redirected and optical components may be too large. Therefore, our optical layout used the external beam port of a Thermo Scientific Nicolet iS50 FTIR spectrometer and is an external setup. The external infrared light beam from the spectrometer is redirected by a 2" flat gold mirror, at an angle of 45° to a 6" parabolic gold mirror (a length of 6" allows for a longer beam path to extend to the polarizer and sample). Before reflecting off the sample surface, this light beam passes through a ZnSe wire grid polarizer. Once light is reflected off the sample, which is mounted in a liquid-solid cell onto a stainless steel rotational stage (allowing for control of the incident angle), it diverges onto a 6" uncoated gold parabolic mirror and is redirected and collimated onto a 4" parabolic uncoated gold mirror. Light is then converged onto a

wide-band mercury cadmium telluride (MCT-B) type detector, chosen due to a wider coverage in the mid IR region (down to 400 cm^{-1}). The optical layout for PM-IRRAS experiments is illustrated in Fig. 2.7.

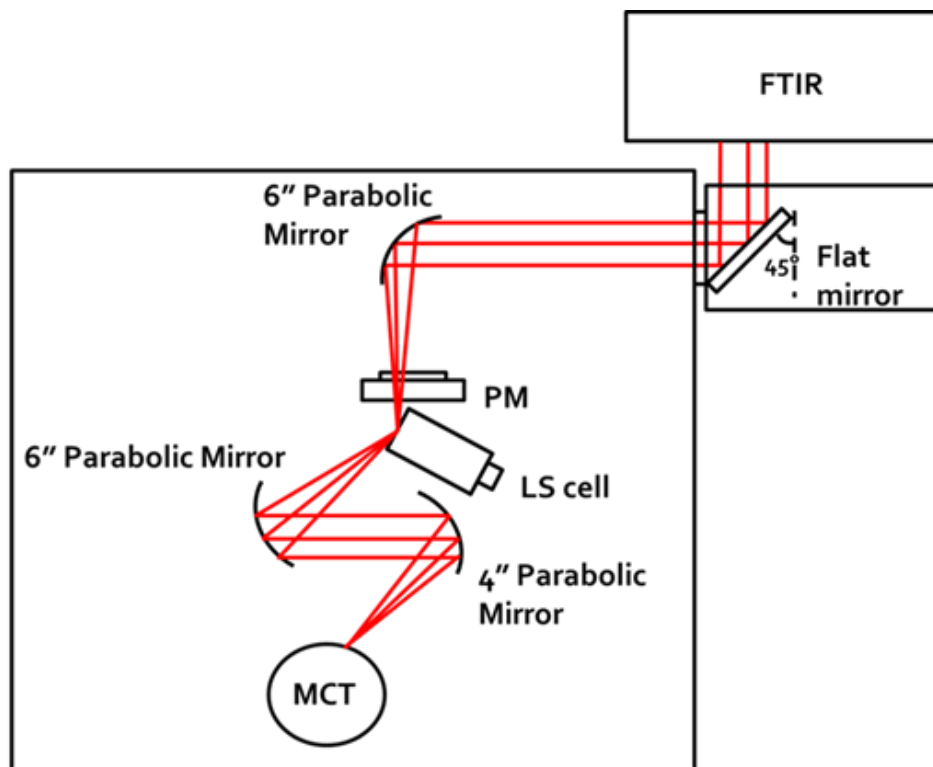


Fig. 2.7 Optical layout for PM-IRRAS, enclosed by two purge boxes and connected by clear PVC tubing.

Incident angle modification was possible through the sample mount in a liquid-solid cell, which was then placed into a stainless steel apparatus. This stainless steel apparatus allows for simple modification of the incident angle and height. Determination of the incident angle through this experimental setup and a schematic of the sample mount is illustrated below in Fig. 2.8. In the schematic and on the stainless steel apparatus, there is a black line near the rotational stage, representing the surface normal. The angle on the yellow line in the schematic (white on the actual rotational stage) is

offset from the surface normal by 45° , the angle on the yellow line is adjusted by the user, depending on optical alignment. Determination of the incident angle (presented as A , in this schematic), is simply: $A^\circ = 360^\circ - 45^\circ - \text{angle modified by user}$ (e.g., 262° for most experiments in this study).

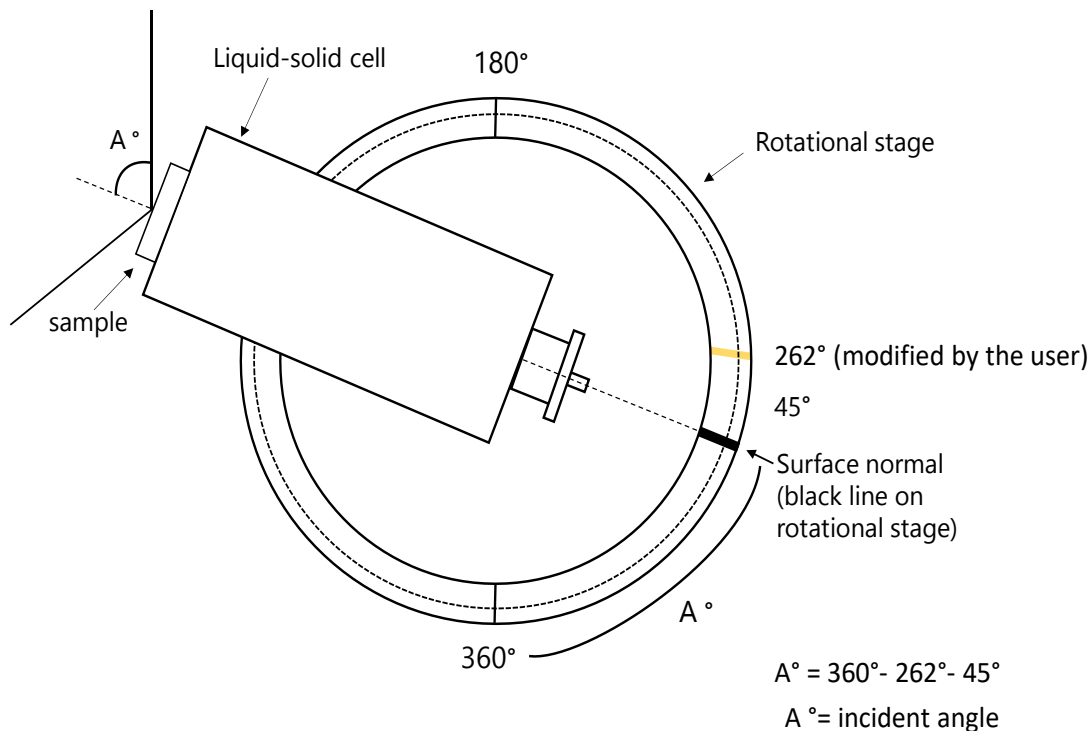


Fig. 2.8 Schematic of liquid-solid cell mount, containing a rotational stage for incident angle modification.

Initially PM-IRRAS experiments were going to be conducted *in situ* with a ZnSe prism to maintain a thin layer of UAFW on the sample surface while heating. However, the original liquid-solid cell had an uneven heat distribution and leaked over time. Therefore, the liquid-solid cell needed to be redesigned and a new ZnSe prism needed to be purchased. To optimize PM-IRRAS experiments, undergraduate Shannon

McElhenney (CBSURE REU participant) performed optical calculations to determine the optimal set-up parameters using Mathematica. This program determined the optimal angle of incidence with different parameters in place, including with and without, a ZnSe prism (45° - 45° - 90°) and a layer of an urea, ammonium formate and water (UAFW) solution on the HA surface. The aim of these calculations was to improve signal intensity and determine if different regions in the infrared required different angles of incidence when a prism and a consistent layer of UAFW was in place. S. McElhenney measured the refractive index of the UAFW experimentally for the visible region and then determined the refractive index theoretically via the Kramer's-Kronig method. Critical angles were calculated with Snell's Law. Before elaborating more on these methods, optical concepts will be reviewed.

Initially, the aim was for infrared light to have a path of: air, prism, UAFW, HA, metal substrate, HA, UAFW, prism and air. However, the system in place for this project has a path of: air, HA, metal substrate, HA, and air. For a light beam to successfully enter and exit different mediums (materials), it needs to be refracted and not reflected, meaning the refractive index (RI) of each material and critical angle are taken into account when calculating the incidence angle. Reflection occurs when light hits an object and instead of being absorbed or passed through this object, light is redirected. Refraction occurs when light hits an object and instead of being reflected off the interface, it bends at this interface and passes through this boundary. For refraction to take place, the refractive index of each material in a path needs to be taken into account. Refractive index (RI) describes the speed of light as it passes through a material; a higher RI value indicates an increased speed. Snell's law describes refraction and predicts the angle at which this light

will bend after passing a material, described in Eq. 2.7. In this equation, n represents refractive index, θ_1 is the angle of incidence, and θ_2 is the angle of refraction. For light to be refracted or pass through a material, the angle of incidence cannot be great than the critical angle. A critical angle is the value of the incident angle in which refraction does not take place, instead reflection does.

$$n_1 \sin \theta_1 = n_2 \sin \theta_2 \quad \text{Eq. 2.7}$$

Since a major component of UAFW is water (1:2:4 molar ratio), the RI varies with water absorption in the infrared region, producing changes in the RI of UAFW as a function of wavelength.^{154,155} A refractive index is complex, described by Eq. 2.8.

$$n = n + ik \quad \text{Eq. 2.8}$$

In this equation, the refractive index is broken down into imaginary (k) and real values (n). Imaginary values refer to the amount of light lost due to absorption by the medium, whereas real values refer to the refracted light. The Kramers-Kronig method relates both real and imaginary parts of the complex refractive index (Eq. 2.9), this method was used to determine the infrared RI of UAFW.¹⁵⁵ In Kramers-Kronig, n represents the complex index of refraction, n_n are the real values and n_k represents the imaginary values, ω is the rotational frequency, ω' is the change in rotational frequency, and P is the Cauchy Principal Value (used for conveying values when using improper integrals).

$$n_n(\omega) = \frac{1}{\pi} P \int_{-\infty}^{\infty} \frac{n_k(\omega')}{\omega' - \omega} d\omega' \quad \text{Eq. 2.9}$$

Transmittance data for UAFW was collected with ATR-FTIR, this data was used to obtain imaginary values of the RI using Eq. 2.10, where λ represents wavelength, α is absorbance, and d_{eff} is effective depth. Real values were calculated by the Kramers-Kronig equation; the imaginary values were then obtained from these real values with code obtained from Rowe et al. and Lucarini et al.^{154,156}

$$k(\lambda) = \frac{\lambda\alpha}{4\pi d_{eff} \log_{10}(e)} \quad \text{Eq. 2.10}$$

Calculated values for the real refractive index of water and UAFW are illustrated in Fig. 2.9, where reference values are used to gauge the precision of these calculations. Fig. 2.9 indicates that calculated values are valid because of their similarity to reference values, and UAFW behaves similarly to water because it is a prime component. After this step was completed, all critical angles were calculated using Snell's Law, critical angles for different interfaces are depicted in Fig. 2.10. These critical angles describe the maximum angle in which refraction rather than total internal reflection occurs. For example, the critical angle for a ZnSe prism and UAFW needs to be below $\sim 48^\circ$ for refraction to occur, not depicted is the critical angle for HA to air, 40° or less.

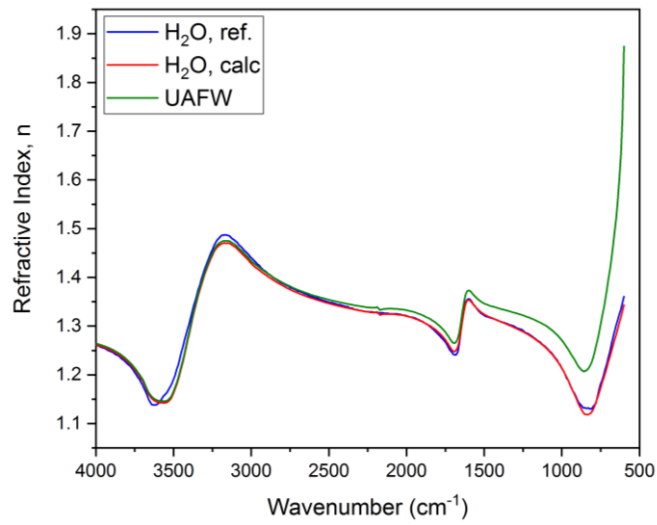


Fig. 2.9 Real refracted index as a function of wavenumbers for calculated water, reference data of water, and UAFW. Image Credit: S. McElhenney

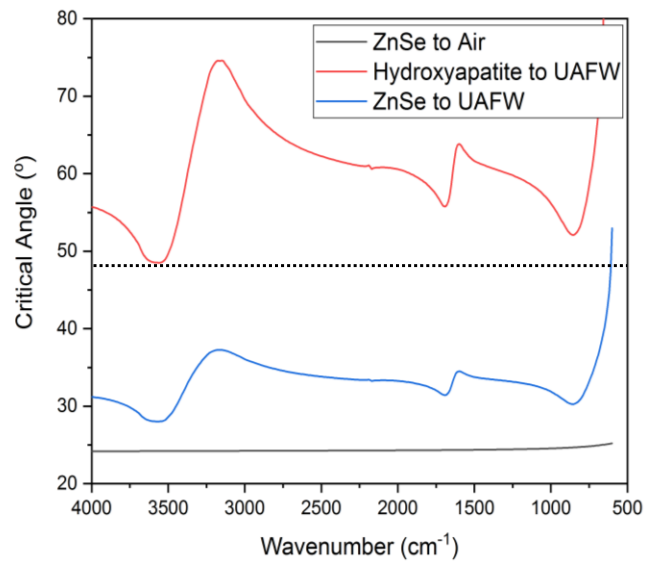


Fig. 2.10 Critical angle for different interfaces as a function of wavenumber. Image Credit: S. McElhenney

In addition to optical calculations, the effect of varying the angle of incidence experimentally for bare HA/Cu was measured. Fig. 2.11 describes the change in spectra as the angle of incidence decreases from 80° to 60°. P-O stretches are negative at 80° and become positive and increase in intensity as the angle decreases. A feature at 1010 cm⁻¹ changes direction and intensity as the angle decreases. The angle used for experiments in Chapter 5 was 53°, for a system with HA and air (UAFW was on the surface of HA, but spectra was collected when this solution was dry). The feature at 1010 cm⁻¹ is present in some of the spectra shown in Ch. 5. Despite 53° used for each experiment, the sample might have been shifted slightly forward, causing this feature to appear in some spectra.

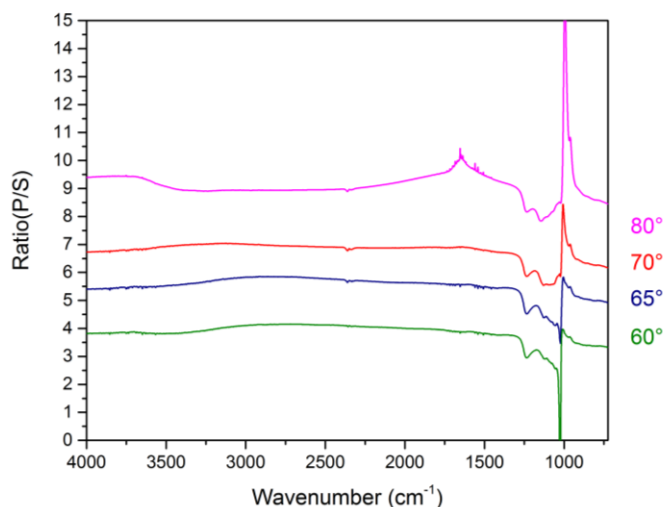


Fig. 2.11 PM-IRRAS spectra of HA/Cu in air at 298 K, where the angle of incidence is varied.

2.2.3.2 Experimental Modifications

An infrared liquid-solid cell was designed by the Abbott-Lyon Laboratory (K. Slavicinska and T. J. Beckman) as a sample mount, illustrated in Fig. 2.12. The cell has a cylindrical body composed of Teflon and an inner rod also made of Teflon. The purpose of the inner rod is to hold the sample in place and adjust the position by bringing it closer to the surface of the Teflon body. Inside this Teflon rod is a 4.5-inch Cu threaded rod and a 0.75-inch Cu disk, a 1-inch diameter sample, with HA on its surface is attached to this disk and threaded rod. This threaded rod, disk and sample are loaded into the inner Teflon rod and a disk is attached to the end of the threaded rod, to limit movement. This inner Teflon rod is then placed in the main Teflon body. The liquid-solid cell is placed in a stainless steel apparatus, containing a rotational stage with corresponding angles at the bottom. This allows for control of the angle of incidence. The design for this experimental apparatus was based on work done by researchers Kubota, Ma, and Zaera.¹⁵⁷

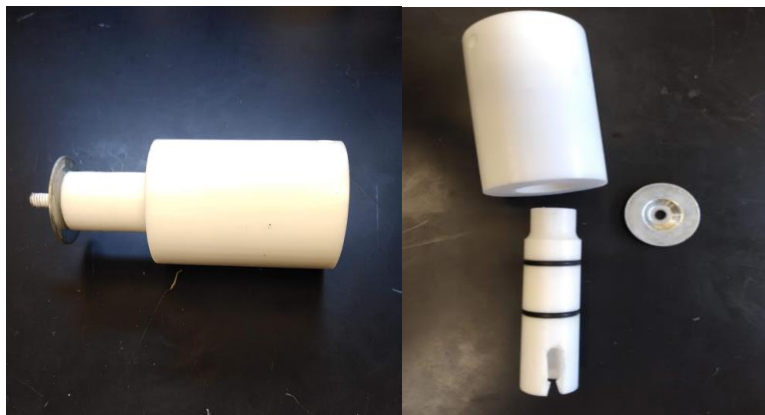


Fig. 2.12 Teflon body cell used for liquid-solid interface analysis. The cell has two Teflon pieces, the smaller piece holds the sample and allows for forward and reverse movement.

After characterization, synthesis, and liquid-solid-cell alterations, a purge system was established to improve the background spectrum. Two different purge boxes were created to cover the entire optics; these were connected with 3.5" clear PVC tubing. A. Nastase helped to establish a purge system using a purge gas generator (Model CO₂-PG14), to limit CO₂ and H₂O gas peaks. This system was connected to a flow meter and Teflon tubing was used to create two lines that would purge the system, one connected directly to the instrument and the other directly to the optical system. As shown in Fig. 2.13, the amount of gas phase H₂O and CO₂ decreased significantly once the system was in place.

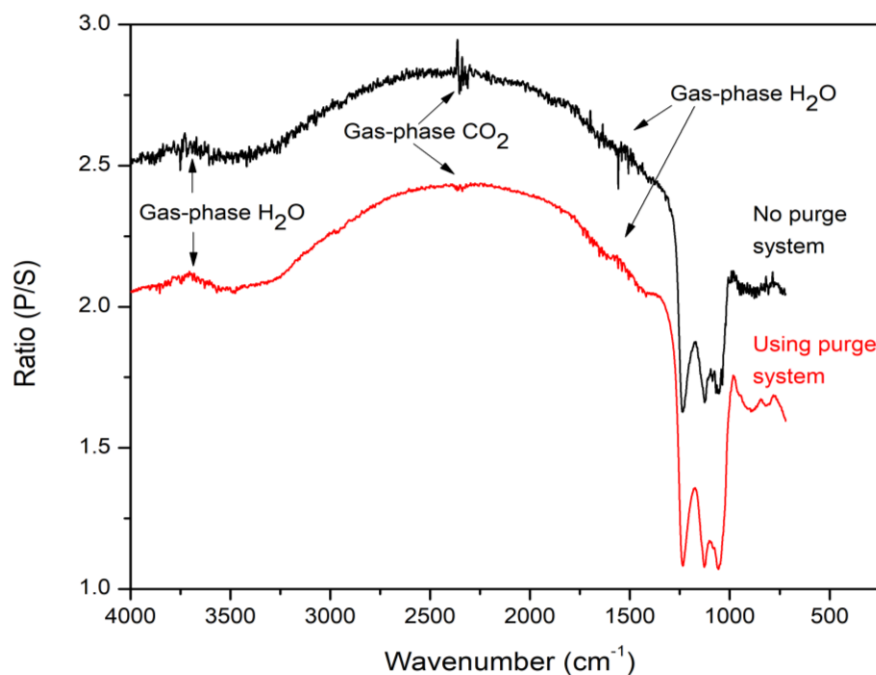


Fig. 2.13 Comparison of PM-IRRAS spectra with and without a purge system. The black line is a single beam spectra of HA without a purge. The red line is also a single beam spectra of HA with a purge in place.

2.2.4 Data Collection and Interpretation

An additional modification included background subtraction performed at the beginning of each experiment, to account for variations due to daily changes in room temperature and humidity. The polarization of light was modulated manually (s- and p-polarization on the grid polarizer are depicted in Fig. 2.14), rather than with an automatic photoelastic modulator (PEM), consistency between each s- and p-polarization of light was ineffective, so a marking was made for the polarization mount. Fig. 2.15 represents the background spectrum before and after incorporating this marking, with B representing a flatter baseline accounting for instrumental noise, mostly found in the P-O region.

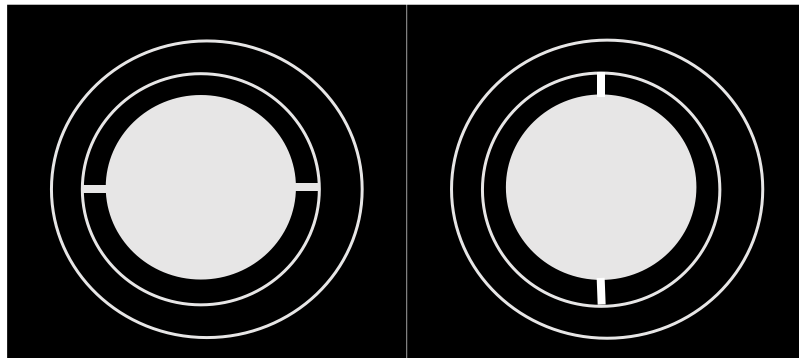


Fig. 2.14 Grid polarizer in a rotation mount, left: s-polarization and right: p-polarization.

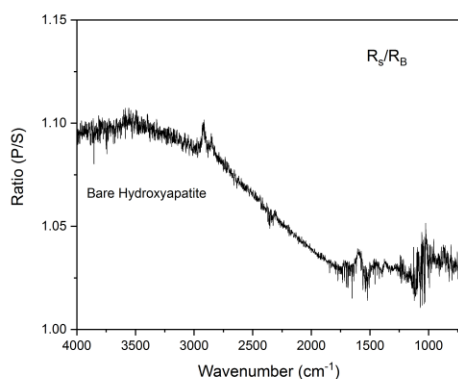
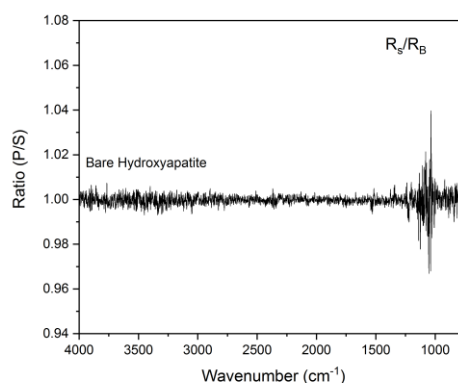
A)**B)**

Fig. 2.15 Comparison of background spectra for HA, termed N_s and represented by R_s/R_b , where $R = P/S$. R_b is the background spectra for all PM-IRRAS experiments performed on the day of consecutive experiments. R_s is taken at the beginning of a series of experiments and after R_b , to assess instrument noise levels. A) N_s spectra without the marking on the polarizer. B) N_s spectra with marking on the polarizer.

After s- and p- polarizations were collected for each sample, spectra were processed to produce a normalized spectrum. Spectral data presented in Chapters 3 and 4 was processed by normalizing p- and s- spectra. That is dividing p- by s- spectra (P/S) to minimize gaseous CO_2 and residual water. However, this processing (P/S) decreased CO_2 and residual water in the normalized spectrum, but did not entirely eliminate it. Processing s- and p- polarizations of light through a different method, was found to be more effective at eliminating spectral noise, this new processing method is depicted below in Eq. 2.11, termed the R-spectrum. This data processing method has been used by other research groups.¹⁵¹

$$R = \frac{(P-S)}{(S+P)} \quad \text{Eq. 2.12}$$

This equation was implemented for data in Ch. 5, and is more effective at reducing residual CO₂ and H₂O compared to processing with P/S. Fig. 2.16 compares spectral processing with Eq. 2.12 and by P/S without and with a purge system in place.

Significantly less CO₂, even when no purge system is in place indicated by the top figure, in comparison to P/S. Fig. 2.16 also illustrates spectral data when a purge system is in place.

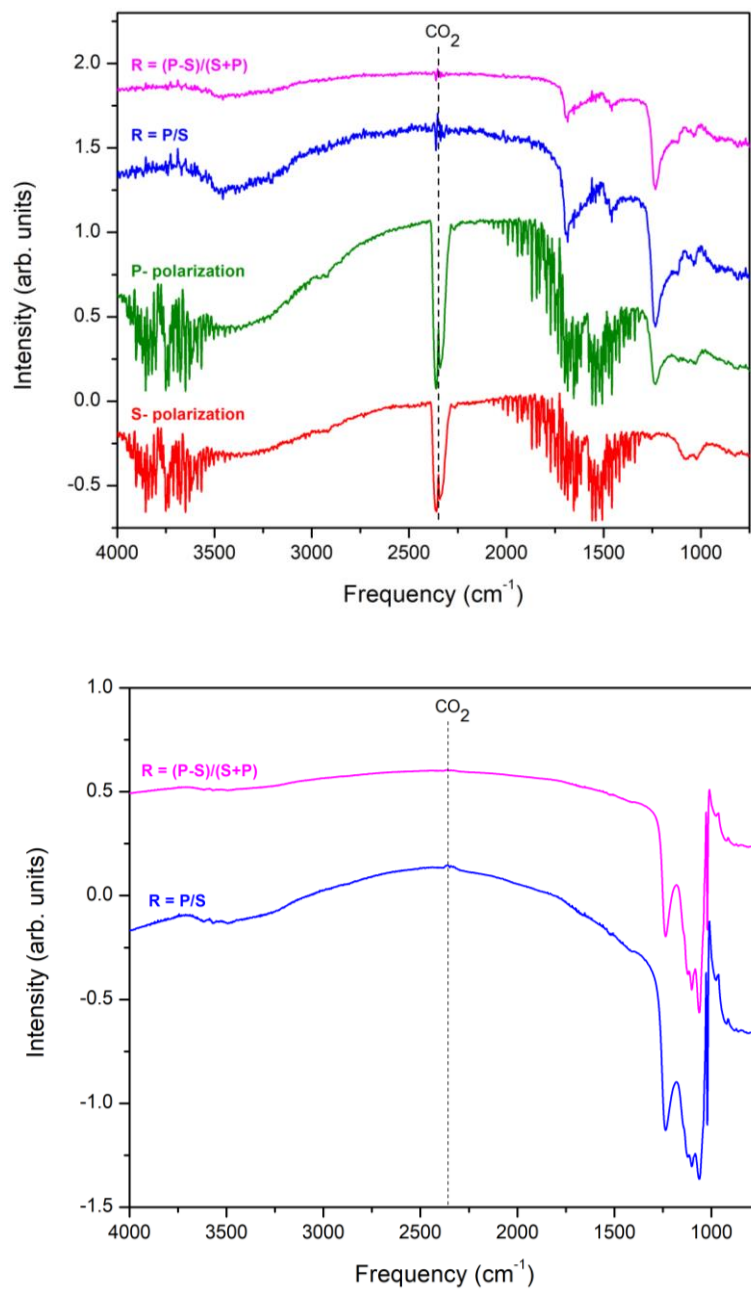


Fig. 2.16 Comparison of data processing methods, spectral data with no purge system (top) and data with purge system in place (bottom). Data processed with Eq. 2.2.4.3 produces a flatter baseline and eliminates CO₂ and H₂O more effectively than P/S.

Initial data collection for an experiment involved: 1) assessing the instrumental noise level before reaction of an HA film, and 2) decreasing the noise level to improve the background for subsequent reaction series for each film. Instrumental noise level was assessed by first collecting an R_b and then an R_s spectrum. R_b spectrum was processed by collecting an R spectrum with s- and p- polarizations, either by processing the data by P/S or by using Eq. 2.13 (since Eq. 2.13 was discovered during the last stage of this project). R_b and R_s spectrum were of unreacted HA films, the latter is taken first and analogous to a single-beam spectrum that would normally be taken without a polarizer, the former is analogous to a single-beam surface spectrum. R_b is the background spectrum for a reaction series of one specific film. After R_b and R_s spectrum were collected, an N_s spectrum was collected by dividing these spectra (represented in Eq. 2.15). N_s spectrum represented the instrument noise level, an ideal N_s spectrum was flat and had no CO_2 or H_2O present, if the spectrum was curved or had CO_2 or H_2O then the system was adjusted before starting a reaction series.

$$N_s = \frac{R_s}{R_b} \quad \text{Eq. 2.15}$$

Spectral data collected for a reaction was processed through a series of four steps that correspond to four R-spectra, which were arbitrarily termed: R-, D-, O-, and B-spectra. R-spectra for all experiments were obtained by processing reaction and background data (bare HA film) by Eq. 2.13 (where x represents a 1, 2, 3 or four hour experiment), and plotting them. The maximum intensity value corresponding to both reaction and background of the R-spectra was typically at 1235 cm^{-1} , and the intensity value of this wavenumber for the background spectrum was obtained. R-spectra for a

reaction series (including the background) were divided by this intensity value, to produce D-spectra, shown in Eq. 2.16. An O spectrum was obtained by locating the minimum intensity value of the D-spectra for a reaction series. This value (C_{min}) was then subtracted from every intensity value for a reaction series to produce O-spectra (Eq. 2.17). Finally, B-spectra were acquired by dividing O-spectra by the background spectrum (O-spectrum of the bare HA film), represent in Eq. 2.18.

$$D_x = \frac{R_x}{C_{bckgd@1235cm^{-1}}} = \frac{\left(\frac{P_x - S_x}{S_x + P_x}\right)}{constant} \quad \text{Eq. 2.16}$$

$$O_x = R_x - C_{min} = \left(\frac{P_x - S_x}{S_x + P_x}\right) - C_{min} \quad \text{Eq. 2.17}$$

$$B_x = \frac{O_x}{B_x} \quad \text{Eq. 2.18}$$

2.3 Characterization Methods

Characterization was used for two primary purposes: initially to confirm and optimize the synthesis of HA and later on to assess mineral corrosion. Mineral corrosion was assessed through solid and liquid characterization. Characterization of the solid mineral was performed through x-ray diffraction (XRD), scanning electron microscopy (SEM), and energy-dispersive x-ray spectroscopy (EDX). These methods provide information about the crystal structure, the surface morphology and film thickness, and the elemental composition, respectively. In addition to solid characterization, the solution was characterized or analyzed with nuclear magnetic resonance spectroscopy (NMR).

2.3.1 X-ray Diffraction (XRD)

X-ray diffraction (XRD) is an instrumental technique used to analyze the crystal structure of a sample, which aids in identification and composition analysis. This technique takes advantage of the defined atomic arrangement found in solids, by studying the crystal structure to understand crystal orientations and phases.¹⁵⁸

XRD bombards a solid sample with x-rays, these incident x-rays are then diffracted and reach the detector. The interaction of the x-rays with the sample can determine interplanar distance (d) between crystal planes, this interplanar distance serves as a fingerprint to identify each material. The interplanar distance is determined through Bragg's law; this equation elaborates on the conditions that allow X-rays to be diffracted and undergo constructive interference.^{158,159}

$$n\lambda = 2d \sin \theta \quad \text{Eq. 2.19}$$

Equation 2.19 represents Bragg's law, where λ describes the wavelength of the incoming X-rays, d is the interplanar distance or distance between crystal planes, θ is the diffraction angle (angle between the incident beam and the crystal plane), and n represents an integer or order of wavelength. In order for X-rays to be diffracted, θ must be varied to follow Bragg's law so that constructive interference occurs to produce high enough signal intensity for detection. Fig. 2.17 is a simplified illustration of X-ray diffraction, where the spheres represent atoms. θ represents the angle between the incident beam and the crystal plane, where θ is also equal to the angle between the crystal

plane and the reflected beam. Therefore, 2θ is the angle between the incident and reflected beam; this is used to gather information about the crystal plane.¹⁶⁰

Fig. 2.17 also illustrates how the crystal planes, x-ray beam, and θ can be used to establish a geometrical relationship to derive Bragg's law. The X-ray beam hits the incoming sample and is reflected at different points, the X-ray beam which hits the crystal Plane 2 (atoms in this plane) travels a longer distance compared the X-ray beam which is reflected at Plane 1. The extra distance travelled by the second X-ray is represented by Eq. 2.20:

$$XZ + ZY = n\lambda \quad \text{Eq. 2.20}$$

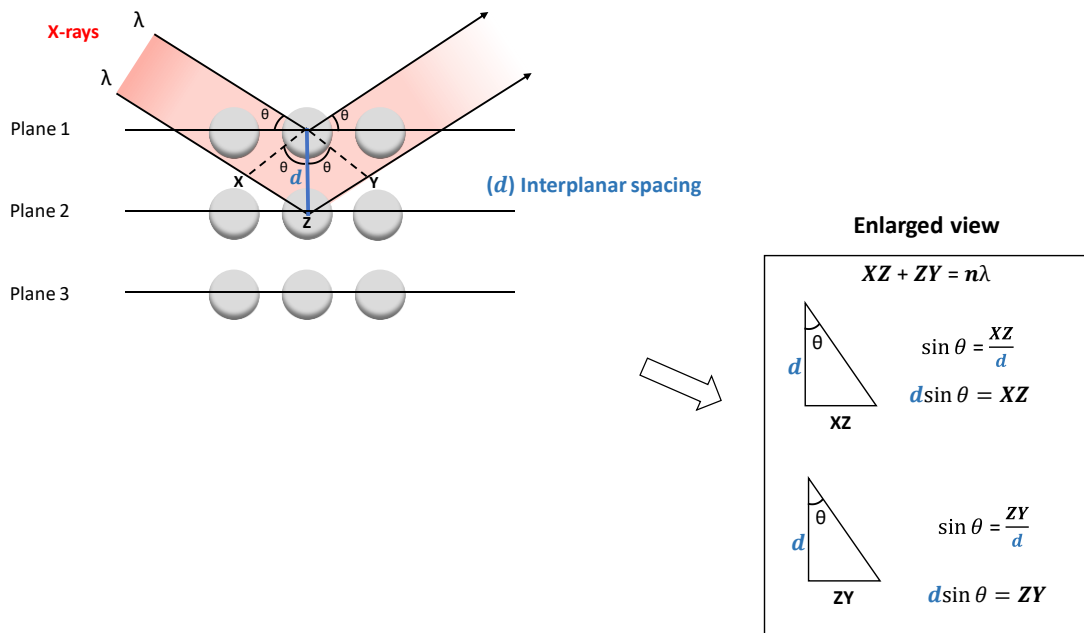


Fig. 2.17 Schematic of a crystal structure where X-rays are diffracted, and geometry of the enlarged view is used to understand and derive the equation for Bragg's Law. The interplanar spacing (represented in blue) is unique to each material.

In Fig. 2.17, the enlarged view shows the formation of two triangles that establish the relationships in Eq. 2.21 and 2.22.

$$d \sin \theta = XZ \quad \text{Eq. 2.21}$$

$$d \sin \theta = ZY \quad \text{Eq. 2.22}$$

Equations 2.21 and 2.22 can then be combined into Eq. 2.19 to give Bragg's law, as shown in Eq. 2.23

$$d \sin \theta + d \sin \theta = n\lambda \quad \text{Eq. 2.23}$$

The basic instrumental design for XRD involves the use of an X-ray tube, to generate X-rays that are then collimated and directed toward the sample on the sample stage and then directed towards a detector. The sample stage and detector rotate and data is obtained at 2θ at varying angles of diffraction to observe different diffraction patterns.¹⁵⁸

2.3.2 Scanning Electron Microscopy (SEM) & Energy Dispersive X-Ray Spectroscopy (EDX)

Scanning electron microscopy (SEM) is an analytical instrument that allows for morphological and topographical studies. SEM can determine defect and non-uniform sites on samples and when this instrument is coupled with energy-dispersive x-ray spectroscopy (EDX), insight into the elemental composition is given.

Unlike a light microscope, in which a combination of light and optical lenses allows for magnification and enhancement of image resolution, SEM is a type of electron microscope, where electrons rather than visible light are used to enhance resolution. The general SEM instrumental design involves an electron gun (electron source), condensing

lenses or electromagnetic lenses (control electron beam size), objective lense (controls distance from lens and samples or working distance), and detectors. This microscope is kept under vacuum to enhance image resolution and prevent damage. ¹⁶¹

Once the electron beam encounters the sample, there are various possible interactions between the electrons and the sample. The signals created by these interactions can be classified into five categories 1) transmitted electrons (elastic and inelastic electron scattering) 2) signals from backscattered, Auger, and secondary electrons 3) visible light 4) x-rays and 5) heat.¹⁶² The variety of these interactions comes from the electron beam scattering electrons from different depths of the sample. Secondary electrons are scattered electrons that are near the sample surface, caused by inelastic collisions. Backscattered electrons are scattered electrons that are found deeper in the sample, caused by elastic collisions. Secondary and backscattered electrons are used in image formation.¹⁶¹

As noted above, X-rays may be one of the byproducts of the interactions between the electron beam and the sample. X-rays are generated through inelastic collisions and, when the electron beam strikes the sample with sufficient energy to displace an electron, are found in the inner shell. This causes an electron from the outer shell to relax into the inner shell, and a photon in the x-ray region of the electromagnetic spectrum is released. The x-rays generated serve as unique markers for each element, because the energy associated with this is related to the atomic number through Mosley's Law. These X-rays are used for elemental analysis, in energy dispersive X-ray spectroscopy (EDX) or X-ray energy-dispersive spectroscopy (EDS).¹⁶² EDX provides information about the elemental

composition through atomic or weight percent, and it can be used for elemental mapping to observe the distribution of elements on the surface.

2.3.3 Nuclear magnetic resonance spectroscopy (NMR)

Nuclear magnetic resonance spectroscopy (NMR) is used for structural analysis and in combination with other analytical techniques may be used for positive identification of a molecule.¹⁶³ The working principle is based on the spin of an atom's nucleus or nuclear spin. Analysis with NMR requires that atomic nuclei have either an odd number of protons and neutrons or both, since these nuclei would have spins of $\frac{1}{2}$ and have an electromagnetic field.¹⁶⁴ Once the sample is prepared, a nucleus of interest is then chosen for analysis (*e.g.*, ^1H , ^{13}C , ^{31}P , and ^{14}N). The sample is sent to the main compartment of the NMR, which contains a strong magnet. The nucleus of interest interacts with the magnetic field of the strong magnet; the spin of the nucleus may align with or opposite of the magnetic field of the strong magnet. A thermodynamic preference exists for alignment with the magnetic field instead of against, and this preference is amplified as the strength of the magnet increases.¹⁶⁴

The atomic nuclei are irradiated with a particular radio frequency; this particular frequency causes resonance (*i.e.*, an increase in amplitude). This radio frequency (also known as a pulse) causes the number of nuclei aligned with and against the magnetic field to be equal. Once this pulse ends, there is a release of energy from the nuclei in the form of radio frequency. The frequency emitted may differ in parts per million from the original frequency applied. The difference in these two frequencies is known as a chemical shift. Chemical shift is dependent upon temperature, pH, magnet strength, and

concentration. A spectrum is obtained from different frequencies within the free induction decay (FID), which is the frequency strength.¹⁶⁴

The nuclei of interest for this project are phosphorus-31 and hydrogen-1. Both coupled and decoupled spectra were collected for phosphorus. Coupled mode refers to the splitting of peaks on the spectra, caused by neighboring atoms of that specific nuclei; in decoupled mode splitting of frequency is not possible and peaks in the spectra appear as singlets (*i.e.*, single peaks).¹⁶⁴

CHAPTER 3. SYNTHESIS, CHARACTERIZATION, & OPTIMIZATION OF HA

HA needs to be synthesized as a thin, uniform film on a conductive metal surface for surface analysis via PM-IRRAS. In IRRAS experiments light is reflected at a grazing incidence angle from a conductive surface. The light must induce a vibrational motion that changes the dipole moment of the adsorbed molecule. In order to obtain a strong signal, the film thicknesses must be less than 2.5 μm , and the underlying substrate must be a strong infrared reflector. A uniform film is desired because of the decreased complexity for R-spectral analysis, meaning fewer binding sites for adsorbed molecules (urea-rich solvents). Copper was the initial metal substrate because of its strong infrared reflectivity and high conductivity, which is important for IRRAS. As a preliminary procedure, synthesis of HA was optimized on Cu foils and this same method was then used for Cu discs. The experimental setup and design for PM-IRRAS required Cu discs with a $\frac{3}{4}$ " diameter, so the sample could be attached to a threaded rod and placed in the liquid-solid cell. Increase in HA film thickness was observed with visual inspection, PM-IRRAS analysis, and XRD analysis. As synthesis was optimized to produce ultrathin films, characterization with XRD was not possible. Therefore, these ultrathin phosphate films cannot be verified as HA, although once the same synthesis method is used but thicker films are produced, HA is confirmed by XRD. Common calcium phosphate phases include dicalcium phosphate dehydrate or brushite $\text{CaHPO}_4 \cdot 2\text{H}_2\text{O}$, dicalcium phosphate CaHPO_4 , octacalcium phosphate $\text{Ca}_8\text{H}_2(\text{PO}_4)_6 \cdot 5\text{H}_2\text{O}$, and amorphous calcium

phosphate $\text{Ca}_9(\text{PO}_4)_6\text{xH}_2\text{O}$. While Ca and P are confirmed by EDX, it may be possible for HA to exist as well as other calcium phosphate phases.¹⁶⁵

3.1 Influence of Electrochemical Parameters on HA films

To increase the infrared signal intensity for PM-IRRAS before electrodeposition, Cu foils and disks were mirror-finished. A mirror-finish was achieved with the use of a 9 μm polycrystalline diamond suspension (MetaDi Supreme from Buehler), UltraPad PSA, TriDent PSA, a 3 μm polycrystalline diamond suspension (MetaDi Supreme from Buehler), and MicroCloth, PSA from Buehler.

Several parameters affecting electrochemically deposited HA films have been tested, with the aim of acquiring thin, uniform, and reflective films. Parameters with a deep impact on these desired features include temperature, concentration of the electrolyte solution, additives (*e.g.*, NaNO_3), scan rate, number of cycles, and voltage range (*i.e.*, potential). Deposition was completed by cyclic voltammetry with baseline parameters of five cycles, a potential range of 0.0 to -1.7 V, 60 ± 5 °C, pH molar solution adjusted to 5.77, an additive of NaNO_3 , and a scan rate of 5 mV s^{-1} . These conditions were chosen primarily based on Ref. 134, which produced films that seem most similar to the desired specifications for our PM-IRRAS experiments. A selection of initial experiments are listed in Table 1.

Table 1. Electrochemical Deposition Conditions for HA/Cu Samples

SAMPLE	TEMPERATURE (°C)	SCAN RATE (mV s ⁻¹)	MAX CURRENT (mA)	POTENTIAL (V)	PH	CYCLES
11 ^a	60 – 65	5.	10.	0.0 - -1.7	4.628	5 ^a
12 ^a	58 – 62	5.	10.	0.0 - -1.7	5.811	5 ^a
13 ^a	56 – 60	5.	10.	0.0 - -1.7	5.771	5 ^a
21	60 – 65	5.	10.	0.0 - -1.7	5.774	5
22	61 – 65	5.	10.	0.0 - -1.7	5.773	5
23	63 – 65	5.	10.	0.0 - -1.7	5.770	5
24	56 – 64	10.	100.	0.0 - -1.6	5.780	5
25	60 – 64	10.	10.	0.0 - -1.6	5.814	3
26	59 – 60	10.	10.	0.0 - -1.6	5.814	3
27	61	15.	10.	0.0 - -1.6	5.690	3
28	62 – 63	20.	10.	0.0 - -1.6	~5-6	3
29	58 – 61	25.	10.	0.0 - -1.6	~5-6	3
30	59	25.	10.	0.0 - -1.6	~4	3
31	58 – 61	25.	10.	0.0 - -1.6	5.744	5
32 ^b	65	25.	10.	0.0 - -1.6	5.780	3
33 ^b	60	25.	10.	0.0 - -1.6	5.442	2
34 ^b	59 – 60	20.	10.	0.0 - -1.6	~5-6	2
36 ^b	58 – 59	25.	10.	0.0 - -1.6	~5-6	2
37 ^b	60 – 62	30.	10.	0.0 - -1.6	~5-6	2
38 ^b	58 – 60	30.	10.	0.0 - -1.6	~5-6	2

^a indicates NaNO₃ was added, ^b indicates 2% (w/w) H₂O₂ was added.

Based on visual inspection (HA films on Cu foils are represented in Fig. 3.1), optimal films for PM-IRRAS studies are achieved with electrochemical conditions of: approximately 58-60°C, a high scan rate (25-30 mVs⁻¹), decreased number of cycles (3-4 cycles), and a decreased potential. As the temperature increases, films become thicker and are not as conducive to surface analysis with PM-IRRAS. The temperature of the molar solution during electrochemical deposition affects the mass of HA deposited onto the WE. According to findings by Thanh and co-workers, there is an increase in film thickness (HA mass) as temperature increases from 60 to 70°C, while the thickness stays consistent from 71-85°C; however, the thickness is still much higher compared to 60°C (~9 mg vs. 4.5 mg).¹⁴⁰ Temperature affects the rate of reaction and ion diffusion rate, As temperature increases, there is a decrease in HA solubility, this allows for a faster growth rate on the WE or copper substrate rather than formation of HA in the molar solution, there is a cutoff point past 70°C, where HA is formed in solution due to a high diffusion rate. To adequately control temperature changes during synthesis, an oil bath was used.

Determination of HA film thickness by visual inspection and PM-IRRAS analysis is illustrated in Fig. 3.1, where infrared signals for corresponding samples are also listed. Fig. 3.1 includes a picture and infrared signal for a mirror-polished Cu foil, this is to illustrate that the highest infrared signal achievable (at that time for the system in place) was 10.5. An optimal infrared signal from PM-IRRAS would be close to the value of 10.5, as long as HA was still detected on the surface. Fig. 3.1 indicated that a decrease in the number of cycles allowed for thinner films although there is a balance in the number of cycles used; a decreased number of cycles allows for thinner films but also decreases film uniformity. For HA films on Cu foils, films became thinner as cycles were decreased

from 5 to 3, but decreased in uniformity with 2 cycles. As illustrated by Sample 23 and 26 (Fig. 3.1), cycles were decreased from 5 to 3 to achieve a thinner film, which was confirmed visually and with PM-IRRAS analysis. Sample 26 has a higher infrared signal of 5.5 compared to a lower infrared signal of 0.8 for Sample 23, indicating that Sample 26 is a thinner film. In order to increase film uniformity and achieve a thin film, the number of cycles may be reduced and the scan rate increased. Sample 23 had a scan rate of 5 compared to 25 mVs^{-1} for sample 29 and 5 cycles rather than 3; Sample 29 has a significantly higher infrared signal of 6.9 rather than 0.8.

Infrared studies of the HA surface, corresponding to Fig. 3.1 are illustrated in Fig. 3.2 with corresponding IR signals of: 3.3, 0.8, 0.3, 5.5, 2.6, and 6.9. These preliminary studies were conducted in air (before establishing a purge) and D-spectra were collected for only the HA surface by subtracting the Cu surface. Spectral peaks confirm the presence of HA, specifically peaks at 1142, 1140, 1050, and 1030 cm^{-1} indicate P-O asymmetric stretches, and the feature at 960 cm^{-1} is attributed to P-O symmetric stretches. Hydroxyl groups in HA correspond to broad stretches from 3500 to 3200 cm^{-1} . Since a purge had not yet been established the peak at 2350 cm^{-1} confirms the presence of CO_2 and peaks at approximately 1650 cm^{-1} suggest residual gas-phase water.

Mirror-Finished
Copper
10.5



Sample 21
3.3



Sample 23
0.8



Sample 24
0.3



Sample 26
5.5



Sample 27
2.6



Sample 29
6.9



Fig. 3.1 Bare mirror polished cu foil and HA films deposited onto Cu foils, sample names are listed above. The number below the sample name is the infrared signal intensity for each film, a high signal intensity with detection of HA is desirable.

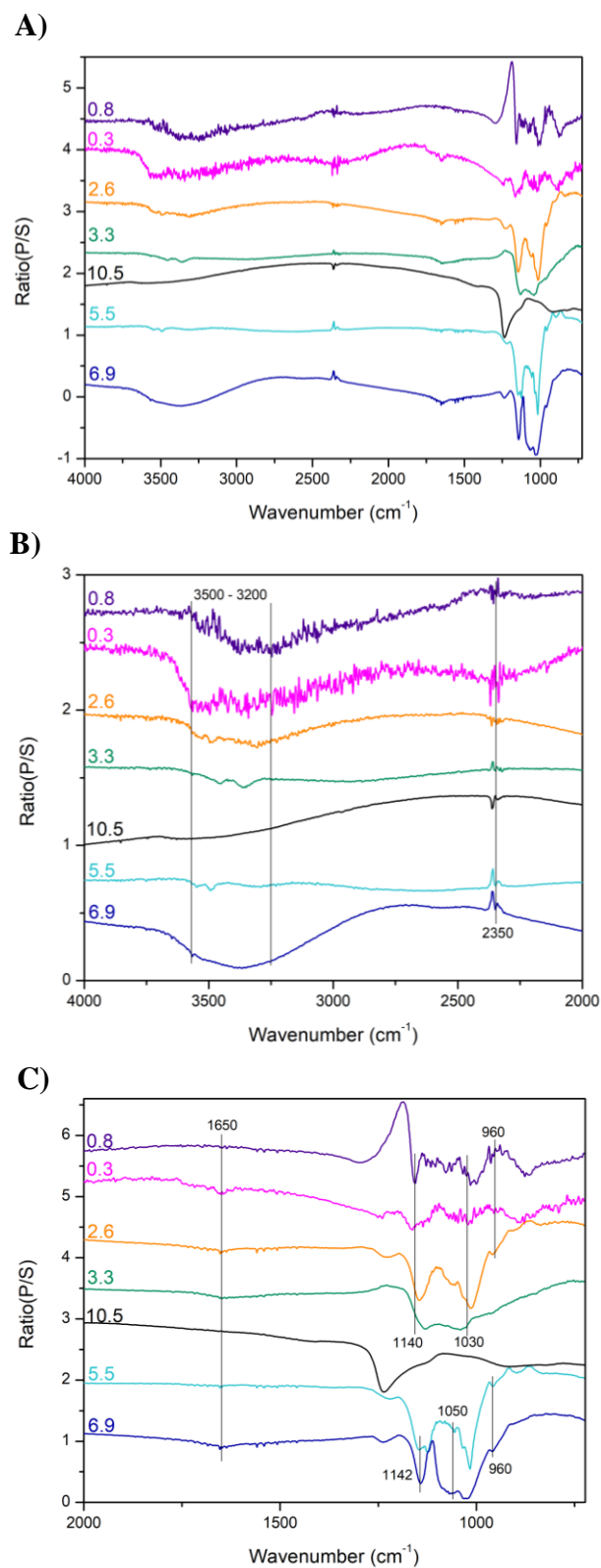


Fig 3.2 PM-IRRAS baseline corrected D-spectra of HA thin films in air at 298 K. Spectra are referenced to a single-beam spectrum of the Cu surface. A) 4000-725 cm^{-1} B) 4000-2000 cm^{-1} C) 2000-725 cm^{-1} .

As discussed in section 2.1.3, XRD gives information about crystallite size and percent crystallinity of the phase. XRD data shown in Fig. 3.3 contains peaks at approximately 26°, 32°, and 53° which coincide with HA crystal planes (002 and 211 crystal plane).^{140,166} Peaks at approximately 43° and 50° correspond to Cu. An underlying challenge with characterization was presented once thin film synthesis was optimized. Thinner HA films produced less intense HA peaks suggesting a smaller crystallite size, this is illustrated in Fig. 3.3 in Sample 11 compared to 31, where HA peaks are less intense. Fig. 3.3 also suggests that brushite was on the copper in samples 27 and 31, since there is a peak at 12°. ¹⁶⁶ EDX was used to ensure the presence of Ca and P on the metal substrate.

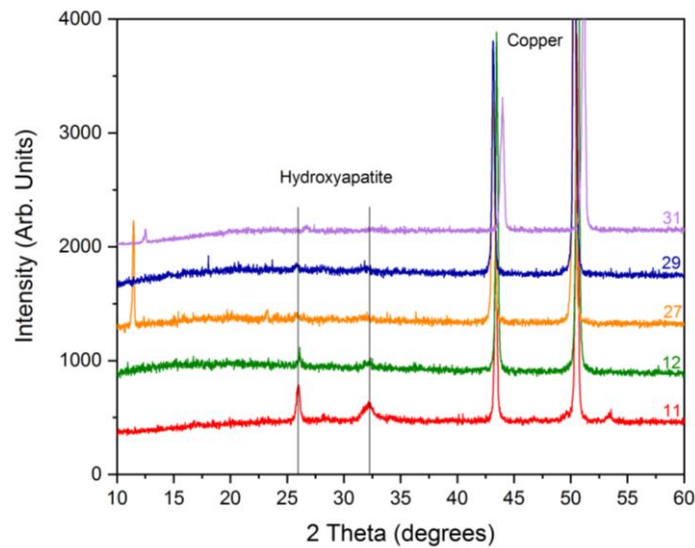


Fig. 3.3 XRD of HA/Cu samples with decreasing thickness. Sample numbers (see Table 1) are listed to the right of each spectrum.

EDX analysis provided information about elemental composition. Analysis confirmed the presence of O, Ca, P, and Cu. Fig. 3.4 has EDX information for Sample 31, and the atomic percentage for elements found in HA as well as the underlying metal

substrate. There are trace atomic percentages for F, N, and Si corresponding to 1.47%, 2.15%, and 0.09%. The detection limit for EDX is 0.1 – 1% for atomic %, suggesting that the actual presence and amount of these trace elements is not certain. An SEM image of Sample 31 at 1 mm is also present in Fig. 3.4, there is coverage of the entire Cu substrate based on the trace atomic % of 0.38 Cu. The SEM image for Sample 31 at 1 mm indicates a much more uniform film at lesser magnification. In contrast, at 500 μm this film appears to be porous and have areas with uneven distribution of HA, in this image, the center appears to have more HA, which is indicated by flaking (Fig. 3.5).

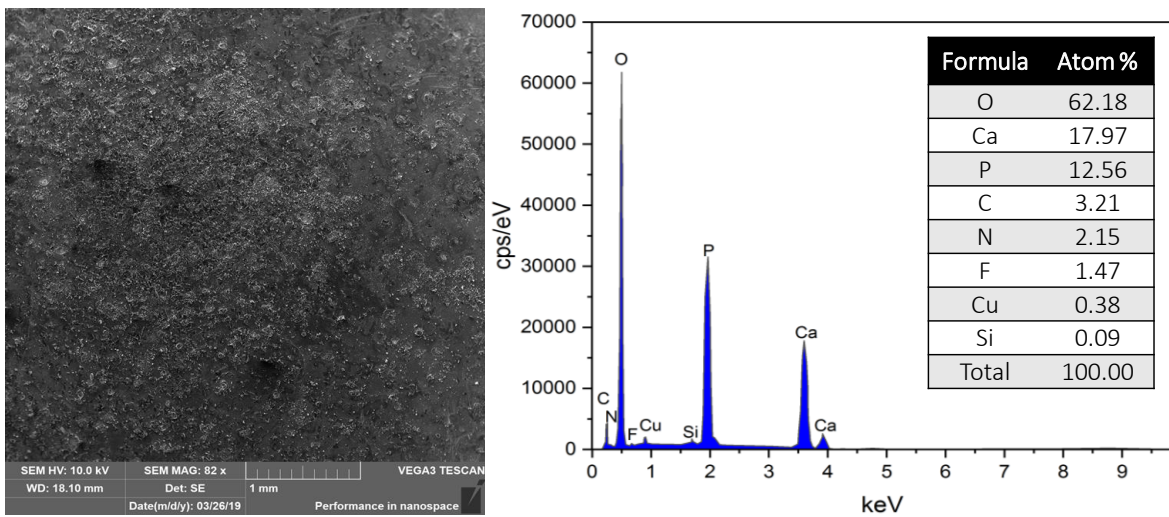


Fig. 3.4 SEM image on the left and corresponding EDX atomic % on the right for sample 31. Electrochemical deposition conditions for this sample are listed in Table 1.

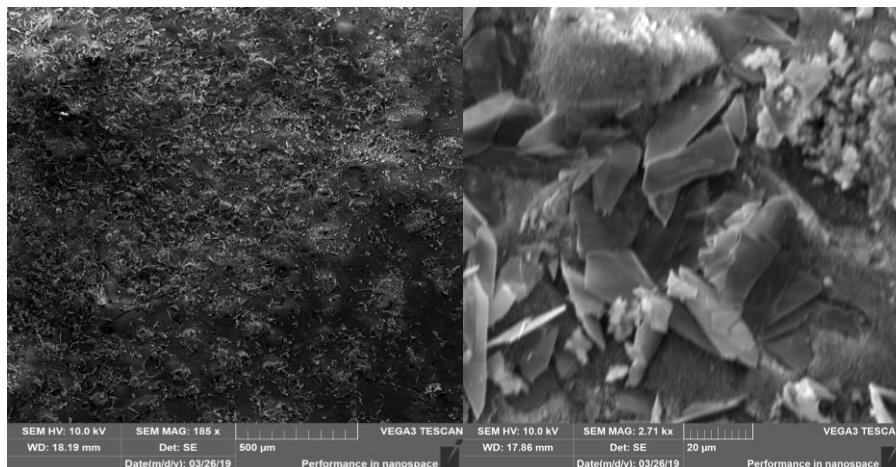


Fig. 3.5 SEM image for sample 31 at 1 mm and 20 μm . Electrochemical deposition conditions for this sample are listed in Table 1.

3.2 Influence of Additives, Temperature, and pH

To further optimize films, the role of additives and pH in the molar solution (0.0168 M $\text{Ca}(\text{NO}_3)_2 \cdot \text{H}_2\text{O}$ and 0.0100 M $\text{NH}_4\text{H}_2\text{PO}_4$) were studied. Additives incorporated into the molar solution at one point or another include: sodium nitrate (NaNO_3), hydrogen peroxide (H_2O_2), and sodium dodecyl sulfate (SDS, $\text{CH}_3(\text{CH}_2)_{11}\text{SO}_4\text{Na}$). These additives were not added all at once, but individually and SEM was used to study their effect on film morphology and topography.

Sodium nitrate was initially added to increase the ionic strength of electrolytes found in the molar solution.¹⁴⁰ This additive was only incorporated into the first three HA samples, since it decreased film uniformity and created uneven areas with more HA growth (Fig. 3.6). The pH of the molar solution was also investigated. The pH of the solution with no adjustments was approximately 4.4 and was pH adjusted to approximately 5.6-5.7 with NH_4OH . When no pH adjustment occurred, HA films

decreased in uniformity, as illustrated in Fig. 3.7. Likewise, when pH of the plating solution was adjusted to ~ 5.7 (a value chosen based on Ref 140) a precipitate formed, but this precipitate would go back into solution if the plating solution was continuously stirred. This precipitate was analyzed with FTIR-ATR and spectra obtained indicate that this precipitate is HA.



Fig. 3.6 An image of Sample 13 indicates that NaNO_3 decreased film uniformity.

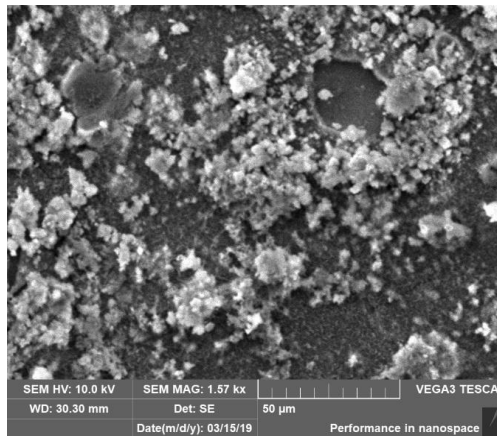


Fig. 3.7 SEM image of HA/Cu film with no pH adjustment.

SEM images of HA films indicate rod-like structures (Fig. 3.8), and film thickness was initially estimated with the use of Cu foils, creating a cross section. The film in Fig. 3.8 was estimated to have a cross-section of $\sim 25 \mu\text{m}$, but creating a cross-section for thinner films and Cu disks was not feasible. To transform the rod-like structures into a more desirable morphology, H_2O_2 was added. Plate-like structures are better suited for surface analysis because they presumably have fewer types of binding sites and, therefore, better infrared peak resolution. Crystal morphology was altered with H_2O_2 concentrations of 2%, 4%, 6%, and 8% (w/w). These concentration values were

chosen based on work done by Thanh et al.¹⁴⁰ The H₂O₂ concentrations used for HA film synthesis are presented in Fig. 3.9 and magnification is from 50 to 10 μm.

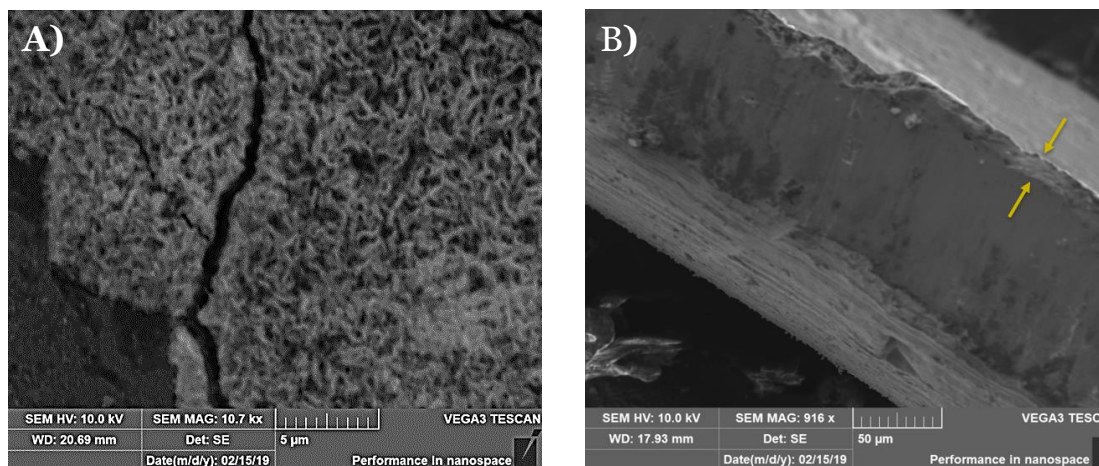


Fig. 3.8 SEM image of HA/Cu sample 12 **A)** surface **B)** cross-section. Electrochemical deposition conditions for this sample are listed in Table 1.

Morphological changes at 2% indicate plate-like structures, present even at 10 μm. Additionally, 4% and 6% concentration have different morphologies, Thanh et al. observed HA films at 200 nm and described blade-like structures at 4% and petiole-like structures at 6%.¹⁴⁰ For our experiments, the highest magnification possible while maintaining adequate resolution was at 10 μm. Despite this, panel G of Fig 3.9 at 10 μm shows rounder and more petiole shaped features, compared to panel F which appears to be less round and contains small spikes.

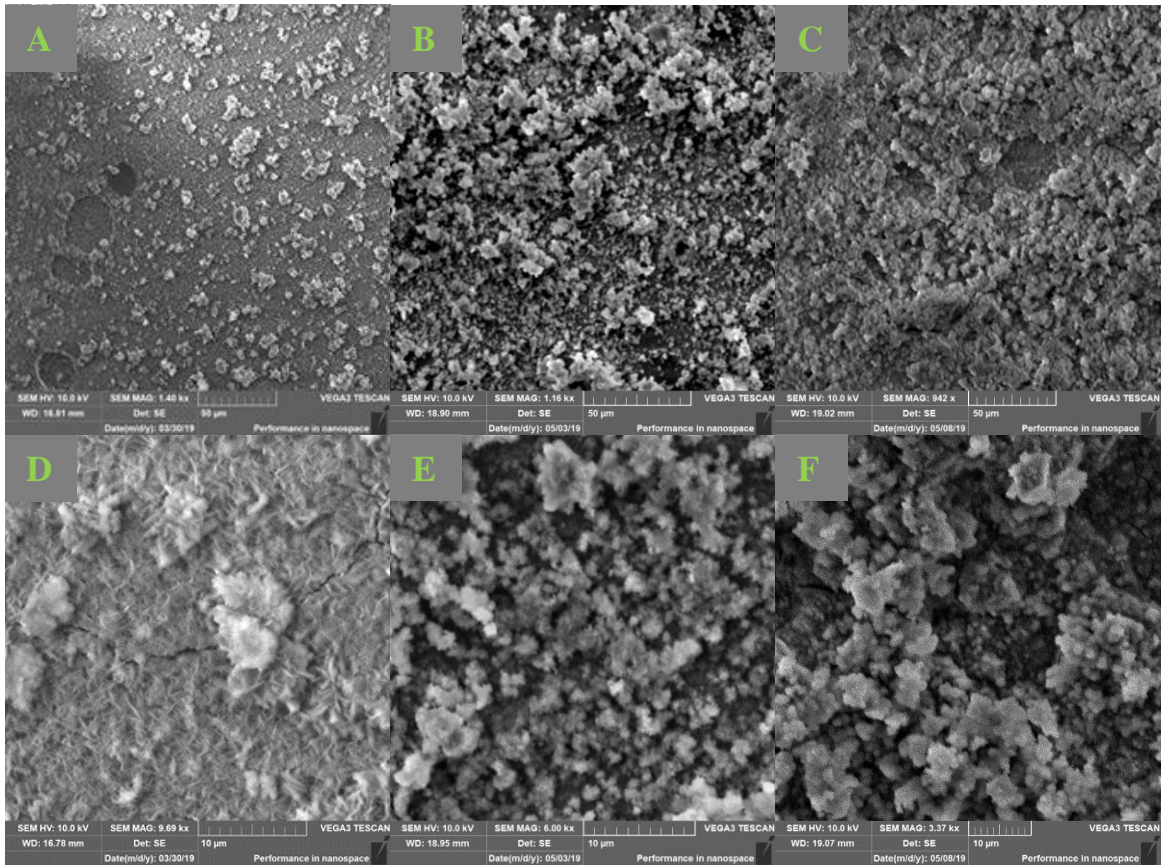


Fig. 3.9 SEM images of HA/Cu films, A-C have a magnification of 50 μm and D-F images have a magnification of 10 μm with H_2O_2 (w/w) 2% (A,D), 4% (B,E), 6% (C,F) respectively.

Despite morphological modification producing plate-like structures with 2% (w/w) H_2O_2 , this film had decreased uniformity compared to 0% (w/w) H_2O_2 (illustrated in Fig. 3.10). The SEM image at 200 μm shows the presence of holes and is a less uniform film compared to a film with no H_2O_2 . Therefore, permanent addition of H_2O_2 was not implemented.

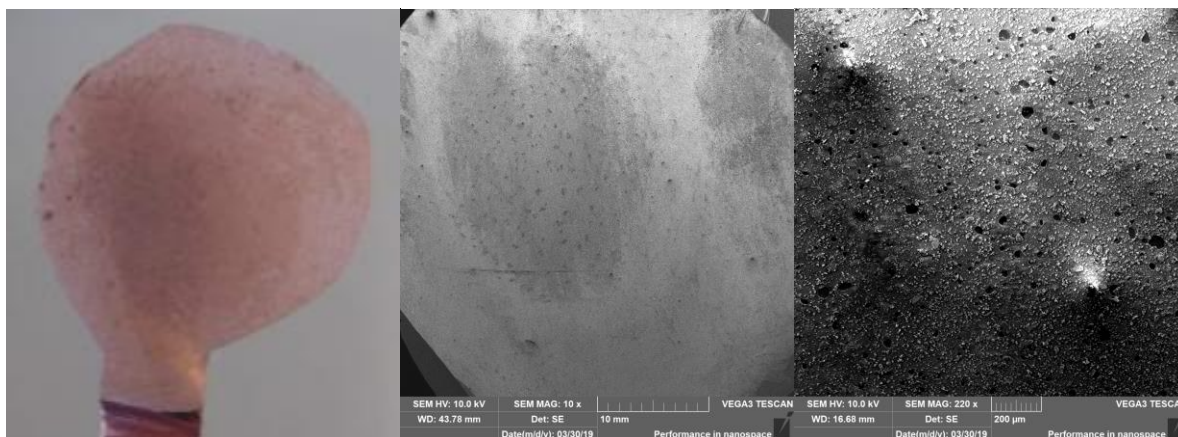


Fig. 3.10 Image of HA/Cu 2% H₂O₂ (w/w) sample (left), SEM image at 10 mm (middle), and SEM image at 200 μm.

To decrease film porosity and increase film uniformity, the surfactant sodium dodecyl sulfate (SDS, CH₃(CH₂)₁₁SO₄Na) was added to the plating solution (see Fig. 3.11). The surfactant was added in concentrations of 0.80 mM and 1.80 mM, and the role of pH was investigated. Previous research done by Yang et al. electrodeposited Cu₂O films on FTO glass substrates and investigated the effect of SDS concentrations on morphology and conductivity.¹⁶⁷ Research done by this group found that addition of SDS has no effect on the crystal morphology of Cu₂O, rather it affects the growth rate. This research found that with a high concentration of SDS, the number of crystals formed decreases but their size increases. When SDS was added to the plating solution, uneven growth was observed with both 0.80 mM and 1.80 mM but uniformity seemed to increase when the plating solution was pH adjusted. Overall the physical appearance of HA was much better without SDS.



Fig. 3.11 Image of HA/Cu sample with 0.80 mM SDS with pH adjustment of 5.80 (A), 1.80 mM no pH adjustment \sim 4.3 (B), and 0.80 mM no pH adjustment \sim 4.3 (C).

CHAPTER 4. REACTIVITY STUDIES

4.1 Reactivity of Copper

After optimizing HA synthesis on copper substrates (*i.e.*, foils and disks), preliminary testing was conducted by placing an HA/Cu disk into the liquid-solid cell and adding UAFW drop-wise to the surface. This resulted in an immediate and unexpected blue color change on the surface, indicating an undesirable side reaction. It became evident that the underlying copper substrate had reacted with the solution (Fig 4.1).



Fig. 4.1 Image of HA/Cu in liquid-solid cell after interaction with UAFW.

To determine if the reaction and subsequent color change were caused by the copper substrate, rather than HA, several control experiments were conducted (see Table 4.1). These reactivity experiments were performed with the help of undergraduate Anna Nastase. Experiments involved adding HA powder (Acros Organics), UAFW, and a mirror-polished Cu foil into a scintillation vial. These experiments resulted in a blue color change for all vials, suggesting that HA could have played a role in this blue color

change. However, an additional experiment containing no copper foils did not result in a color change.

Table 4.1 Summary of control experiments for UAFW, Cu, and HA.

UAFW (μL)	HA powder (g)	Mirror-polished Cu foils	Blue color change observed	Mirror-polished Cu foils	Blue color change observed
1500	0.2	yes	yes	no	no
1500	0.4	yes	yes	no	no
1500	0.6	yes	yes	no	no
1500	0.8	yes	yes	no	no
1500	1.0	yes	yes	no	no

Subsequent experiments focused on components of UAFW, to better understand which component reacted with copper oxide to produce a color change, since other urea-rich solvents could have been used (*e.g.*, urea, acetamide, and ammonium nitrate, UAcAN). 1500 μL of urea and water (UW), ammonium formate and water (AFW), and water were added to three separate clear plastic test tube vials each containing a HA/Cu sample. After 20 minutes had elapsed, the vial with AFW produced a blue color change, while the remaining vials were clear. The ammonium formate in UAFW reacted with copper oxide to produce a blue color change (see Fig. 4.2).

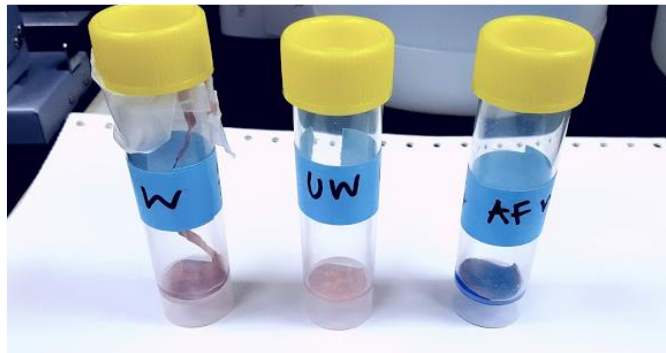


Fig. 4.2 HA/Cu samples with the left vial containing water, middle vial is urea and water, and the right vial contains ammonium formate and water. All control experiments were performed at room temperature.

4.2 Mitigation Strategies

4.2.1 Alternative Solvents

Initial mitigation strategies involved using alternative prebiotic solvents and increasing HA film thickness (increased film thickness is not favorable for surface analysis). The original aim of this study was to understand if phosphorylation of organic substances was primarily surface rather than solution based. Therefore, solvents used needed to be both prebiotic and allow for a significant yield of phosphorylated species. Alternative solvents were chosen based on previous research on urea-rich solvents interacting with HA.²²

Experiments involved alternative solvents replacing ammonium formate with acetamide in the urea-rich solution. A HA/Cu sample and 1500 μL of acetamide and water were added to a plastic test tube vial; this produced no color change within the first week; however, after eleven days a blue color change was observed. Other solvents tested included ammonium nitrate, with the same experimental conditions as mentioned above

and at room temperature; this solution became bright blue as well. Ammonium nitrate produced a blue color change after four days, compared to ammonium formate which produced a color change within 20 minutes of the experiment. This may be due to a stronger affinity of the nitrate anion to ammonium compared to weak affinity to formate. These findings suggested that ammonium and copper oxide interactions produced the blue color change. This hypothesis was tested by reacting ammonium hydroxide and water (1500 μL) with an HA/Cu sample, resulting in an immediate blue color change.

A mechanism for the reaction of copper oxide and ammonium formate was proposed by Anna Nastase, illustrated in Fig 4.3. In Step 1 of the proposed mechanism, ammonium formate dissociates into solution to produce a formate and ammonium ion. Copper (II) oxide then reacts with two ammonium ions to undergo a proton exchange twice, this proton exchange allows for water to become a leaving group. Once water leaves, a copper ion and two ammonia compounds are left and Step 3a depicts the reaction between a copper ion with four ammonia compounds to form a copper ammonia complex.

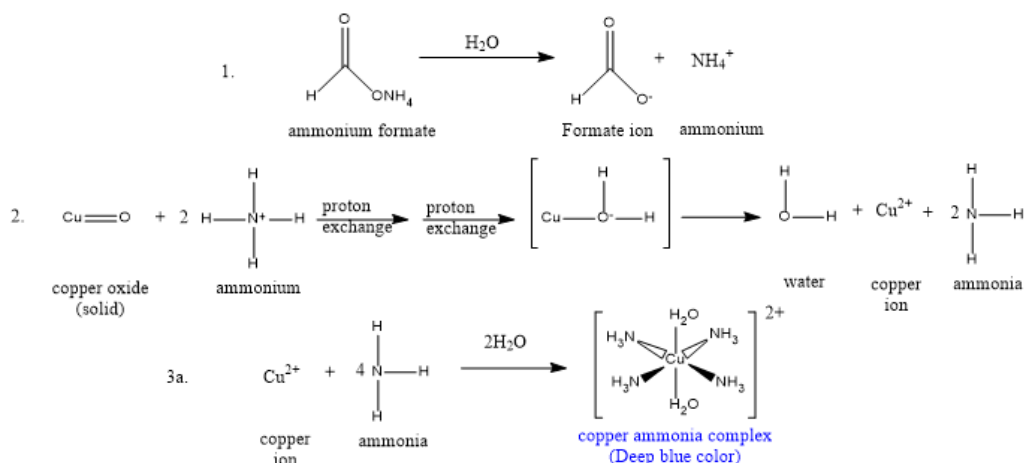


Fig. 4.3 Proposed reaction mechanism for ammonium formate reacting with HA/Cu foils. This mechanism could explain the blue solution. Image Credit: Anna Nastase.

Based on previous research by Eduard Schweizer, the reaction between ammonia and copper oxide produces and is characterized by a dark blue color. He discovered this copper ammonia complex in the 19th century as $[\text{Cu}(\text{NH}_3)_4](\text{OH})_2$ or tetraamine copper(II) hydroxide, now known as Schweizer's reagent.¹⁶⁸ Substances such as acetamide and ammonium compounds (*i.e.*, ammonium formate, ammonium nitrate, and ammonium hydroxide) may form ammonia in solution. Alternatively, UAFW was pH adjusted to slightly more acidic and basic conditions to pHs of 4, 5, and 9 in an attempt to limit or slow down this reaction (UAFW without adjustment has a pH of ~7). Acidic solutions experienced a slower color change, compared to the basic solution of pH 9, but the color change still proceeded (Fig. 4.4). A possible explanation for increased speed of this color change reaction for pH adjusted solutions, may be based on the reaction of ammonia and water (Fig. 4.5). An increase in hydroxide ions, shifts the equilibrium to the reactants side, causing an increase in ammonia and ammonia reacts with copper or metal oxides to produce a color change. Acidic solutions may shift reaction equilibrium (Fig. 4.5) to the right and produce ammonium rather than ammonia.

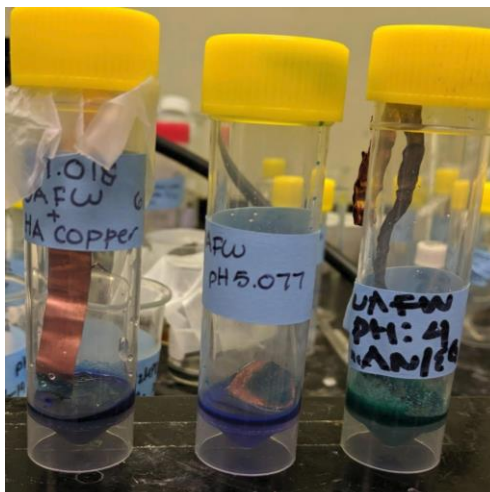


Fig. 4.4 Image of UAFW (pH~7) with HA/Cu samples, pH adjusted (from left to right) to ~9, ~5, and ~4.

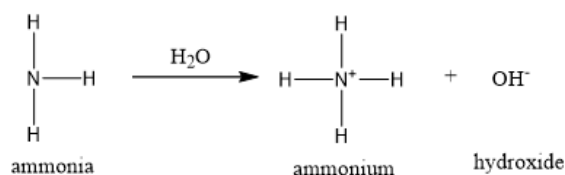


Fig. 4.5 Reaction of ammonia and water.

Image Credit: Anna Nastase.

4.2.2 Alternative metal substrates

Alternative solvents tested were chosen based on phosphorylation yields with HA²² and all solvents contained ammonia or amide that would react with copper oxide. Since surface analysis (*i.e.*, PM-IRRAS) was conducted with a liquid-solid cell explicitly machined for copper disks with a diameter of 0.75 inches, using an alternative metal would require purchasing this material and machining it to fit the liquid-solid cell.

Therefore, alternative solvents were investigated first rather than alternative metal substrates.

Reactivity experiments of metal substrates were performed at 65°C and not room temperature, since the original objective involved *in situ* surface analysis at elevated temperatures (*i.e.*, 65 and 85°C). (*n.b.*, Reactivity of copper was apparent at room temperature, so less focus was placed on its reactivity at elevated temperatures.)

Metals tested first included iron, due to its high reflectivity in the infrared region and stainless steel (ss) because of its stability. Experiments with these metals involved electrodeposition of HA, illustrated in Fig. 4.6. After electrodeposition, preliminary testing with PM-IRRAS was conducted, and the infrared signal was fairly low and difficult to achieve with no established mounting structure. These samples were also characterized with SEM/EDX, but rather than electrodepositing HA on various metals, quicker and more time efficient experiments moved to simply reacting the metals with UAFW at 65°C. Iron, stainless steel, and nickel were reacted in the conditions mentioned above, depicted in Fig. 4.7. Reactivity was assessed through physical observations (*i.e.*, color change) and quantified through EDX (as suggested by Dr. Poyraz). Quantification was performed with EDX because of its accessibility as a departmental instrument. EDX experiments were referred to as “drip pan experiments,” because the post-reacted solution of each metal was dried down at 65°C in aluminum sample pan lids (normally used for TGA experiments). This dried down product was then analyzed with EDX to determine if any metal ions were detectable in a significant amount. No certified standards were used for EDX quantification, and the detection limit of EDX is generally 0.1% wt.¹⁶⁹



Fig. 4.6 Image of HA/Fe (left) and HA/SS (right).



Fig. 4.7 Image, from left to right of iron, stainless steel, and nickel in UAFW. These experiments were heated to 65°C and all metals reacted in solution with ammonia.

EDX analysis of “drip pan experiments” for iron and stainless steel are shown in Table 4.2 and 4.3 below. Table 4.2 confirms the presence of iron in solution, with an atomic percentage of 7.79% and weight percent of 24.38%. Likewise, Table 4.3 confirms the reactivity of stainless steel, because Cr, Fe, and Ni were detected with weight percentages of 2.81%, 8.33%, and 1.05% and these elements are prevalent in stainless steel.

Afterward, aluminum was tested as an alternative and a flame atomic absorption spectrometer (AAS) rather than EDX was used to quantify aluminum ions in solution, because “drip pan experiments” were conducted on an aluminum pan, making quantification of aluminum ions difficult with EDX. The AAS is overseen by Dr. Koether and experiments for aluminum were conducted with her assistance and permission. An aluminum pan was reacted with 1500 μL of UAFW at 65°C. An external standard calibration method was chosen and a calibration method was developed using three

known aluminum standard solutions (from a 1000 ppm aluminum atomic absorption spectroscopy standard from Fischer Chemicals) with concentrations of: 50 ppm, 100 ppm, and 150 ppm. A 1:10 unknown solution was prepared, ~1000 μ L of the reacted UAFW solution was diluted to 10 mL in a volumetric flask. Calibration standards are plotted in Fig. 4.8, and this linear function is represented by the equation: $y = 0.0017x + 0.0059$. An absorbance value of 0.203 was obtained for the unknown solution and the solution was determined to have a concentration of 117 ppm Al.

Table 4.2: Elemental Analysis by EDX of reacted product on an aluminum TGA pan for iron.

Element	Weight %	Atom %
C	14.75 \pm 0.10	21.92
N	20.93 \pm 0.39	26.67
O	37.81 \pm 0.35	42.19
Al	2.15 \pm 0.02	1.42
Fe	24.38 \pm 0.09	7.79

Table 4.3. Elemental Analysis by EDX of reacted product on an aluminum TGA pan for stainless steel.

Element	Weight %	Atom %
C	16.59 ± 0.35	22.53
N	24.34 ± 1.69	28.34
O	41.43 ± 0.94	42.24
Al	5.12 ± 0.11	3.10
Si	0.32 ± 0.04	0.19
Cr	2.81 ± 0.09	0.88
Fe	8.33 ± 0.27	2.43
Ni	1.05 ± 0.11	0.29

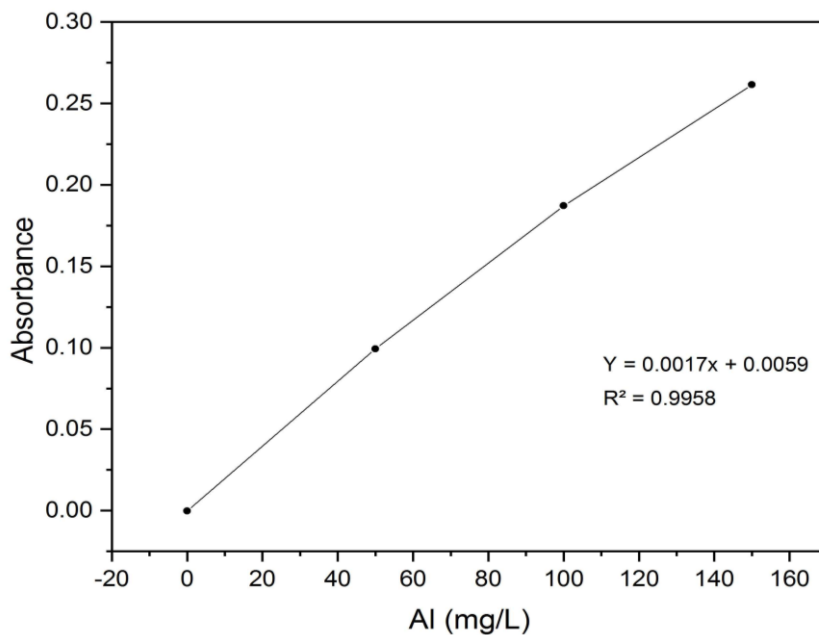


Fig. 4.8 Calibration plot using 50, 100, and 150 ppm (mg/L) of aluminum standard solutions for atomic absorption flame spectroscopy.

Since iron, stainless steel, aluminum, and nickel experienced a color change and released metal ions in solution when reacted with UAFW, the next metal tested was gold. Gold foils are more costly than gold-plated flat mirrors (normally used for optics), so this mirror (uncoated from Thorlabs) was reacted with 1500 μL of UAFW at 65°C. A “drip pan experiment was conducted with the solution, and the dried down product was analyzed with EDX, represented in Table 4.4. EDX analysis indicated no release of Au ions into solution and showed small quantities (under 0.1 wt%) of Cl, K, and Ca. The presence of Fe was most likely due to contamination of glassware. A summary of analytical techniques and observations for metal substrate reactivity with UAFW is found in Table 4.5.

Table 4.4 Elemental Analysis by EDX of reacted product on an aluminum TGA pan for an Au flat mirror.

Element	Weight %	Atom %
C	16.74 \pm 0.13	24.54
N	17.46 \pm 0.34	21.96
O	23.78 \pm 0.19	26.18
Al	41.52 \pm 0.15	27.11
Si	0.12 \pm 0.01	0.08
Cl	0.03 \pm 0.01	0.01
K	0.02 \pm 0.00	0.01
Ca	0.09 \pm 0.01	0.04
Fe	0.24 \pm 0.02	0.08

Table 4.5. Summary of observations and analytical techniques used for UAFW reacted solutions with several metal substrates. Image Credit: Anna Nastase.

Metal substrates	Physical Observations	Analytical Method	Results
HA/Copper foil	Dark blue solution with light blue precipitate	EDX	Cu in solution
Nickel foil	Translucent, turquoise solution	N/A	N/A
Stainless steel foil	Translucent, slate grey solution	EDX	Cr, Fe, Al and Ni in solution
Iron foil	Opaque rust red solution and precipitate	EDX	Fe in solution
Aluminum pan	Translucent, pale-yellow solution	Flame AA, EDX	Al in solution
Gold-plated mirror	Colorless solution	EDX	No gold in solution

4.3 Synthesis on Gold

After the gold-plated flat mirror was determined to be unreactive at 65°C, the next step involved electrodeposition of HA onto this substrate. The gold-plated flat mirror had a diameter of 1” and was too large for the three neck, round-bottom flask (24/40 joint size), so a new flask was acquired (side joints 24/40 and one 34/45 center joint). The order of the electrodes was altered, since the largest opening was the center joint, so the WE (Au) was placed here, which might have an effect on the accuracy of the potential reading. An alligator clip was attached to the flat mirror, and only half of the mirror was

submerged into the plating solution during synthesis for preliminary testing. Synthesis of an ultrathin HA film onto this gold-plated mirror was achieved, and the initial film produced on this substrate is depicted in Fig. 4.9. Electrochemical parameters, such as scan rate and potential remained the same as for copper.



Fig. 4.9. Image of gold-plated flat mirror (left) and an ultrathin HA film on the gold-plated flat mirror (right).

Initial synthesis of HA had limited surface coverage since only half the gold-plated mirror was coated, but coverage improved over time with repetition (Fig. 4.10 and Table 4.6). These films were characterized by SEM/EDX and PM-IRRAS; EDX analysis of an HA/Au film is listed in Table 4.7 and confirms the presence Ca and P. SEM images indicate that films are uniform and porous, a comparison of HA films on Au and Cu is represented in Fig. 4.11. Advantages of gold-plated flat mirrors compared to copper include an increased infrared signal intensity for PM-IRRAS, ~12 for gold and ~9 for copper, which may be due to a larger surface area (*i.e.*, 1 inch compared to 0.75 inches). A higher signal intensity with the bare HA surface is beneficial since signal intensity will decrease once a solvent interacts with this surface. Additionally, gold is more difficult to oxidize so it remains reflective for a longer period of time, while copper disks required constant mirror polishing to maintain their reflective finish.



Fig. 4.10 Image of HA films on gold-plated flat mirrors show improvement in surface coverage. From left to right: samples W, AA, and AG. Synthesis conditions are listed below in Table 4.5.

Table 4.6. Synthesis conditions for HA/Au samples, all had a potential of 0 to -1.6 V.

Sample	W	AA	AG
pH	5.653	5.413	5.725
Scan rate (mVs^{-1})	25	30	25
No. Cycles	4	4	4
Temperature ($^{\circ}\text{C}$)	58-61	59-64	57-58

Table 4.7. Elemental Analysis by EDX of HA/Au sample AF.^a

Element	Weight %	Atom %
C	2.71 ± 0.07	6.43
O	36.90 ± 1.29	65.71
Si	7.05 ± 0.08	7.15
P	7.18 ± 0.24	6.61
Ca	12.67 ± 0.11	9.01
Cr	0.61 ± 0.04	0.33
Au	32.88 ± 0.64	4.76

^a Synthesis conditions: pH: 5.649, scan rate: 25 mVs⁻¹, no. cycles: 4, temperature: 57-58, and potential: 0 to -1.6 V.

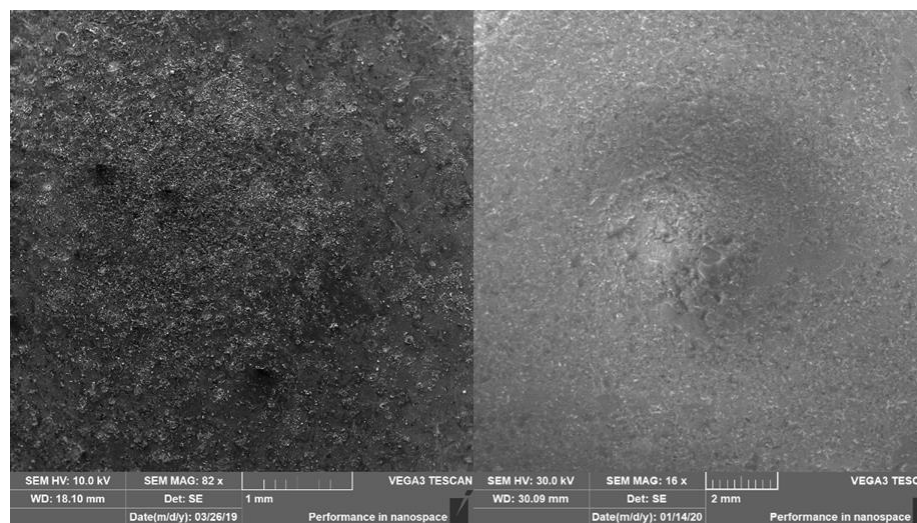


Fig. 4.11 From left to right, SEM images of HA/Cu Sample 31 and HA/Au sample AF. Electrochemical deposition conditions for these samples are listed in Table 1 and Table 4.6.

CHAPTER 5. UREA, AMMONIUM FORMATE, AND WATER ON HA

Once a synthesis protocol was developed, and the experimental setup was optimized for HA, reactivity studies were performed. The aim of these experiments were to investigate the activation of phosphorus on phosphate minerals and understand the molecular interactions of UAFW with HA. The overall aim was to observe structural changes on the mineral surface as a function of time. Given the number of chemical species involved, understanding the complex spectra that describes the interactions between UAFW and HA is challenging. In particular, spectral features may overlap or be attributable to more than one compound.

To better understand and assign spectral features of UAFW on HA, HA was reacted at room temperature (298 K) with several different combinations of the solvent: W (water), UW (urea and water in a 1:4 ratio), AFW (ammonium formate and water in a 1:2 ratio), and UAFW (urea, ammonium formate and water in a 1:2:4 ratio). The total reaction time was four hours, and spectra were collected at one hour intervals, when the surface was wet (*i.e.*, within 5 minutes of removing from the solution) and dry (*i.e.*, 45 minutes after removing from solution). The experimental setup for the reactivity studies is shown in Fig. 5.1.

Most of the spectra presented here are dry spectra, because they are easier to interpret. Wet surface spectra were more difficult to analyze because the spectra had to be acquired quickly, before the purge could be re-established, and the wet mineral surface was actively evaporating as the spectra was collected. Therefore, gas-phase CO₂ and H₂O signatures in the spectra are significant. Additionally, the liquid layer on the wet surface absorbed infrared light, lowering the overall signal intensity.

Supporting information for spectral analysis and mineral corrosion for the reaction between UW, AFW, and UAFW was acquired prior to and after reaction by SEM/EDX and PM-IRRAS, while NMR was solely used for post-reaction analysis of the supernatant. SEM/EDX characterization was performed with the help of undergraduate Christian Luda. NMR of the reacted solution, excluding water, was collected at the same one hour intervals when infrared spectra were acquired. NMR was used to understand the time frame for phosphate release into solution. (*n.b.*, Samples were not centrifuged or filtered since the solution remained clear.)



Fig. 5.1 Experimental setup for reactivity studies.

5.1 Data Analysis of Water (W) on HA at 298 K

As discussed in Chapter 2, there are numerous ways to present spectral data. PM-IRRAS spectra of H₂O adsorbed to HA, are presented as R-spectra in Fig. 5.2. Both R and O-spectra contain a spectrum of the mineral surface before reaction (background), which is significant in illustrating peaks solely contributed by HA.

Fig. 5.2 presents R-spectra from 4000-750 cm⁻¹ with peaks at 3612, 3551, and 3488 cm⁻¹ observable on HA even before reacting with water. After reaction, these peaks appear to decrease in intensity. If these peaks were solely from the contribution of moisture, they would increase in intensity and grow as they react with water over time. Because this is not the case, these peaks are attributed to hydroxyls in or on the mineral itself. These hydroxyl groups from the mineral are most likely in different orientations since their frequencies vary. A free hydroxyl group has a frequency of ~3696 cm⁻¹, when adsorbed to a surface the frequency is going to be red shifted.¹⁷⁰ Since HA was not confirmed by XRD, rather Ca, P, and O were confirmed by EDX various calcium phosphate phases could have been present. Spectral features from 3612 to 3488 cm⁻¹ are attributed to hydroxyl groups within HA, the shift in frequencies may be due to different connectivities due to the presence of various calcium phosphate phases. The more bonds an oxygen atom makes to other atoms, the more electron density is drawn away from the OH bond. This causes a decrease in frequency for the hydroxyl group (*i.e.*, it is red shifted).^{171,172} The region from 1250-950 cm⁻¹ contains PO stretches. As HA interacts with water, these peaks decrease in intensity (Fig 5.2B).

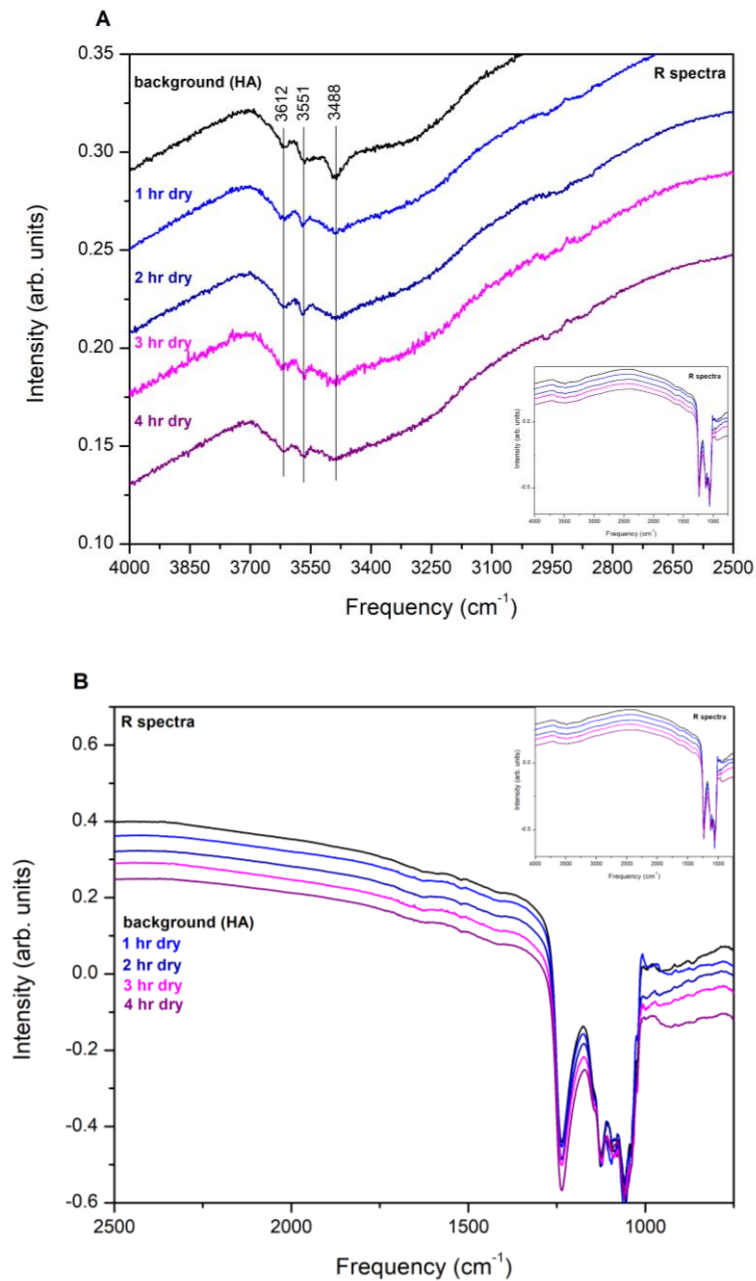


Fig. 5.2 PM-IRRAS spectra of H_2O adsorbed to HA at room temperature. Main panel is an R spectra from $4000\text{-}2500\text{ cm}^{-1}$, while the inset is an overview of the entire R spectra from $4000\text{-}750\text{ cm}^{-1}$.

Fig. 5.4 contains B-spectra of this data, where reacted-spectra are background corrected, and HA is represented as a dashed green line. Reacted-spectra were separated for clarity. Absorbance peaks are generally defined as peaks pointing upwards; peaks pointing downwards are compounds already present on the HA film. (*n.b.*, This is applicable for B-spectra only.) For example, Fig. 5.2A (R-spectra) contains OH stretches from $\sim 3612\text{-}3600\text{ cm}^{-1}$, which are pointing downwards indicating functional groups already present on the HA film, rather than pointing upwards, which would indicate their formation is caused by water. In order to verify and confirm these statements, B-spectra were rigorously compared to their counterparts in the R-spectra.

Fig. 5.3A contains B-spectra but also has an inset of R-spectra, containing an HA spectrum in black. In the spectra, peaks at 2919 and 2849 cm^{-1} are pointing upwards, suggesting that these peaks grew in as the mineral surface interacted with H_2O ; however, these peaks are present on the HA spectrum observed in the R-spectra. These features are present before interaction with H_2O and are most likely due to CH stretches, indicating contamination of the mineral film. Contamination may be due to the cleaning process of the gold-plated flat mirrors. These were rinsed with acetone and water before electrodeposition; residual acetone might have remained on the surface and been covered during the phosphate film deposition. Features at 2459 , 2364 , and 2327 cm^{-1} are assigned to interactions between P and OH, as P-OH stretches, these were not present on the mineral surface prior to reaction, and are caused by the interaction of water.^{173,174} Features from $2100\text{-}750\text{ cm}^{-1}$ are represented by B-spectra in Fig. 5.3B, where 1237 , 1127 , 1085 , 1020 , and 964 cm^{-1} correspond to PO stretches.^{173,175}

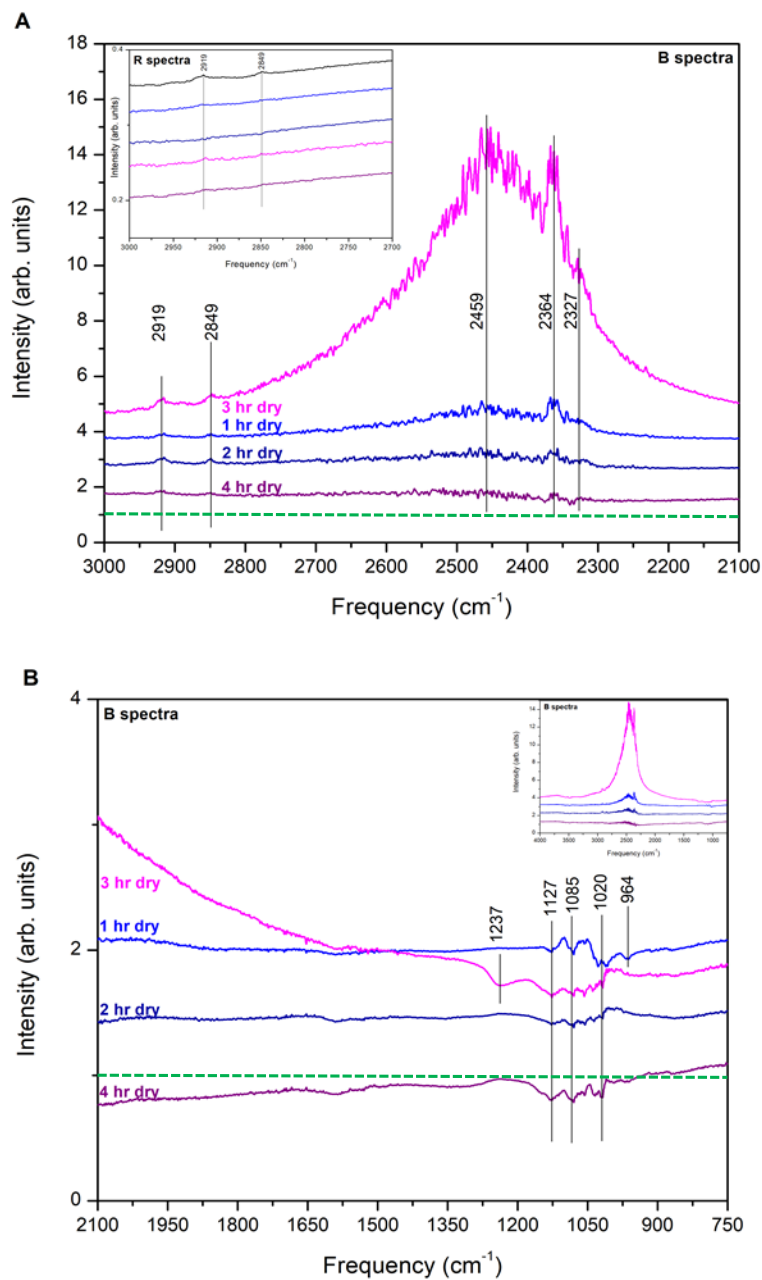


Fig. 5.3 PM-IRRAS spectra of H_2O adsorbed to HA, reaction occurred with 6 mL of H_2O at 298 K. A) 3000-2100 cm^{-1} , inset is the R spectra from 3000-2750 cm^{-1} , B) B spectra 2100-750 cm^{-1} , inset is an overview of the B spectrum from 4000-750 cm^{-1} .

5.2 Data Analysis of Urea-Water (UW) on HA at 298 K

6 mL of UW (1:4 molar ratio) were reacted with HA, Fig. 5.4 depicts PM-IRRAS data in terms of R-spectra. Fig. 5.5 illustrates the O-spectra, this allows for easier interpretation and distinguishes differences between the background and reacted-spectra. It is evident that features from 3600 to 2700 cm^{-1} and 1600 to 1250 cm^{-1} are peaks created by UW, because these peaks are absent in the background-spectra. A close up of the region from 1300 to 1000 cm^{-1} shows a decreased intensity for PO stretches compared to the background, resulting from the mineral interacting with UW.

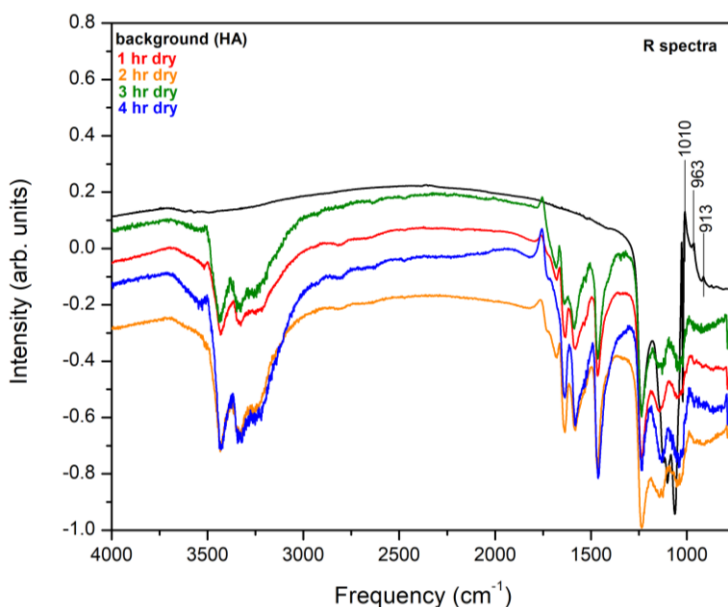


Fig. 5.4 PM-IRRAS spectra of UW adsorbed to HA, reaction occurred with 6 mL of UW at 298 K. R spectra from 4000-750 cm^{-1} .

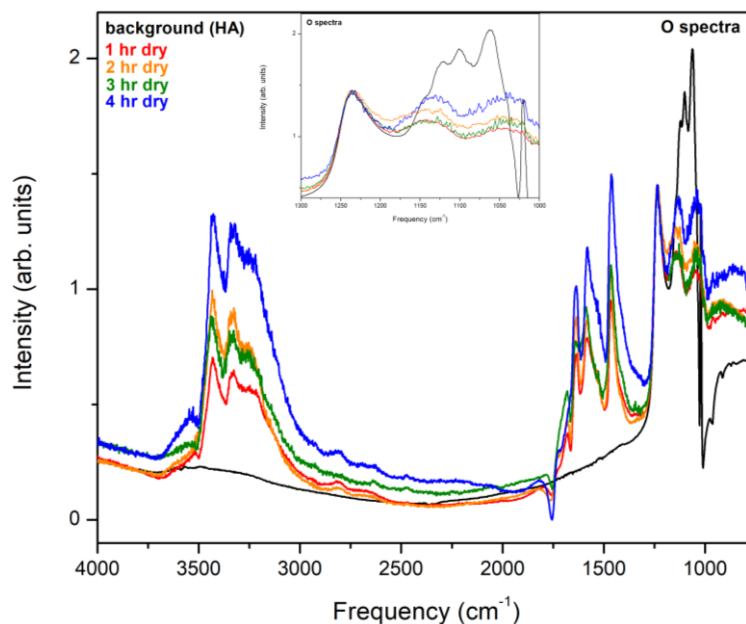


Fig. 5.5 PM-IRRAS spectra of UW adsorbed to HA, reaction occurred with 6 mL of UW at 298 K. O spectra from 4000-750 cm^{-1} , inset is a close up of PO stretches from 1300-1000 cm^{-1} .

Fig. 5.6 contains B-spectra, broken down into a high and low infrared region. Fig. 5.6A contains the region from 4000 to 2200 cm^{-1} and shows that peaks at 2798, 2636, 2469, and 2354 cm^{-1} grow in intensity with increased reaction time. They are most intense after four hours compared to the first hour. Increased intensity with time suggests that these features are due to interactions with water. Features at 2469 and 2354 cm^{-1} are assigned to P-OH stretches, as discussed in Section 5.1. Peaks at 2798 and 2636 are new and could possibly be assigned as C-H stretches. However, because they have a similar shape as P-OH stretches at 2469 cm^{-1} and 2354 cm^{-1} and they grow as reaction time increases, they are more likely additional P-OH stretches.¹⁷⁴ The change in frequency for these blue-shifted P-OH stretches may be different adsorption sites (*e.g.*, atop, bridge, threefold, and fourfold). The peak at 3521 cm^{-1} appears to be shifted and grows with time

to a frequency at 3527 cm^{-1} . This peak may be attributed to an OH stretch from water, because it is absent in the HA spectrum and appears to increase in intensity with reaction time.¹⁷⁰ However, it might also be attributable to an asymmetric stretch from NH_2 , which is present in urea.^{176,177} Features at 3430 , 3330 , and 3218 cm^{-1} are most likely caused by NH_2 groups from urea, where hydrogen binding between NH_2 and OH functional groups may cause shifts in the frequencies.¹⁷⁶⁻¹⁸⁰

Lower frequency values for the adsorption of urea and water are depicted in Fig. 5.6B. Here, the baseline is represented as a dashed line. The feature at 1754 cm^{-1} may be caused by the C=O stretch of the carbonyl group on urea, which is observed between 1670 and 1680 cm^{-1} in pure urea.¹⁸¹ A theoretical model predicted this feature at 1749 cm^{-1} with a Hartree-Fock method using a basis set of 6-31G with a Gaussian 86 program.¹⁷⁶ The feature at 1682 cm^{-1} can be attributed to either C=O or C-N symmetric stretches. Features at 1638 and 1585 cm^{-1} are attributed to NH_2 bends, while 1464 cm^{-1} is a combination of a C-N stretch, C=O bend, and an NH_2 rocking vibration from urea. The peaks at 1090 and 1060 cm^{-1} are PO stretches, which have also been observed on unreacted HA.¹⁷³⁻¹⁷⁶ Lastly, peaks at 963 and 913 cm^{-1} were present on HA before reaction (*c.f.*, the black spectrum associated with HA and the colored-spectra showing UW adsorption on HA as shown in Fig. 5.4). Therefore, these two features can be assigned to PO stretches or to hydroxyl groups bending with respect to the surface. The feature at 963 cm^{-1} is possibly caused by hydroxyl groups interacting with water, which might have been adsorbed to the surface prior to reaction suggesting that water was present before reaction.^{174,183} The feature at 786 cm^{-1} is assigned to a C-O out-of-plane bend in urea.^{176,177,182}

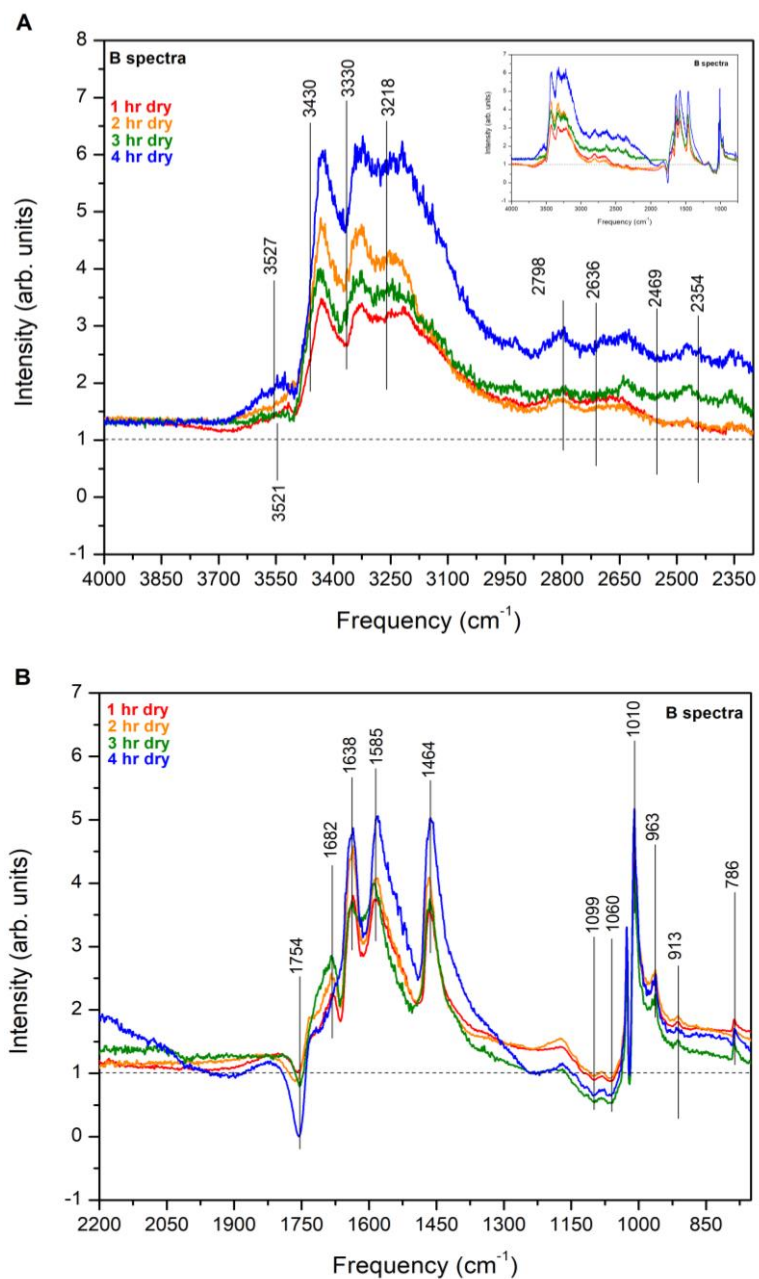


Fig. 5.6 PM-IRRAS B spectra (baseline corrected) of UW adsorbed to $\text{Ca}_{10}(\text{PO}_4)_6(\text{OH})_2$ (HA), reaction occurred with 6 mL of UW at 298 K. A) 4000-2200 cm^{-1} , inset is an overview of the entire R spectra from 4000-750 cm^{-1} , B) 2200-750 cm^{-1} .

EDX analysis of the mineral surface prior to reaction confirmed the presence of Ca and P with an atomic percentage of 8.22% and 5.81%, respectively. Elements of 1% or greater were also detected on the surface including: C, which is ascribed to contamination of the film, as well as Au and Si, which are the major components of the gold-plated flat mirrors (Table 8). Cr was also present on characterization of HA films prior to and after reaction. Cr is used as a binding layer between Au and the silica base in the mirrors.

Some of the gold-plated flat mirrors developed small bare Si patches from overuse. To determine if Cr might have gone into solution, inductively coupled plasma optical emission spectroscopy (ICP-OES, Perkin Elmer Avio 200) was performed. A chromium reference standard (Ricca Chemical Company) was used to create calibration standards with concentrations of 0.01, 0.05, and 1 ppm. Three samples were analyzed: 1) Sample 1 was a 6 mL solution of UAFW that interacted for four hours with a gold-plated flat mirror with bare Si patches, 2) Sample 2 had the same conditions as Sample 1 except 10 mL of UAFW were used, and 3) Sample 3 had the same conditions as Sample 1 except no bare patches exposing the underlying silica were observed. Samples 1, 2, and 3 were analyzed at 267.716 nm, and contained 11, 13, and 10 ppb of Cr in solution. These are very trace amounts of Cr and would likely not contribute to any side reactions between UAFW and HA. Additionally, there was no considerable difference in the observed reactivity between gold-plated flat mirrors containing patches of exposed silica and those without patches of exposed silica.

Post-reaction analysis of HA by EDX in Table 5.1 indicates that Ca and P are still present on the surface with atomic percentages of 2.61% and 1.75%, respectively. An elemental map overlaid on an SEM image is illustrated in Fig. 5.7. This image shows the

center of the HA film after it reacted with UW for four hours. Ca and P were still detected on the gold-plated flat mirror, and a small amount of N, where P appeared to have a larger coverage of the surface compared to Ca (see Fig. 5.7). ^1H -decoupled- ^{31}P -NMR analysis of the UW solution resulted in no phosphate detection, even after four hours of reaction with the UW solution (Fig. 5.8).

Table 5.1 Elemental Analysis by EDX of HA/Au After four hours of Reaction with Urea-Water Solution at Room Temperature.

Element	Atom % Pre-Reaction	Atom % Post-Reaction
C	7.17	23.11
N	--	39.82
O	63.30	29.38
Al	0.08	--
Si	10.20	1.94
P	5.81	1.75
Ca	8.22	2.61
Cr	0.39	0.07
Au	4.84	1.32
Total	100.00	100.00

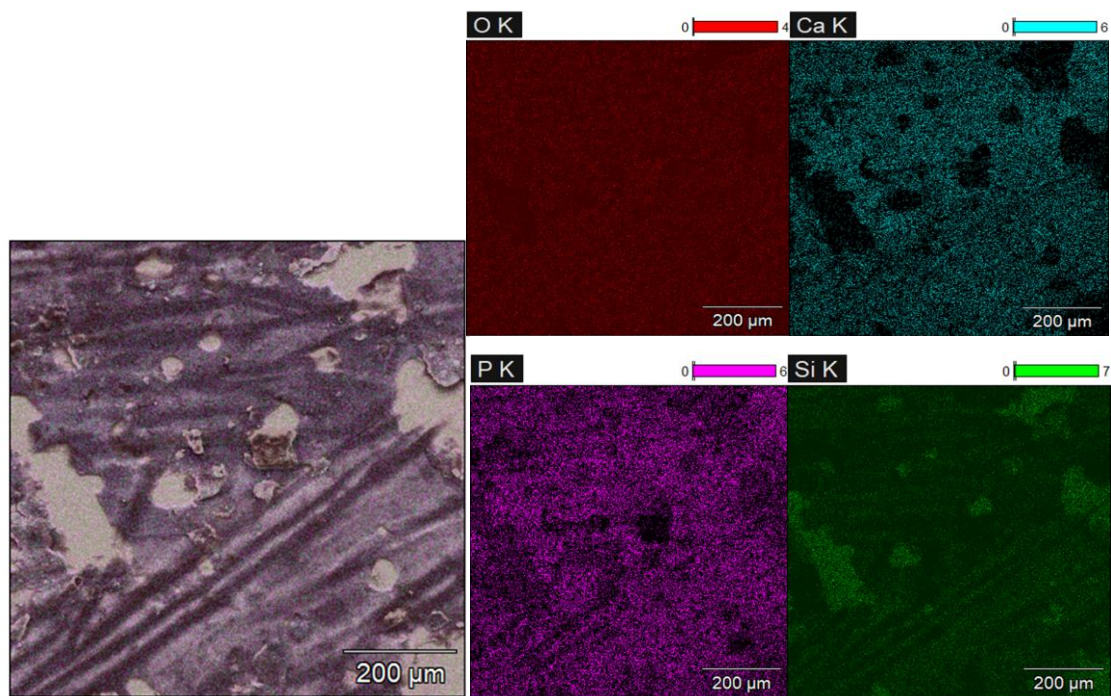


Fig. 5.7 EDX mapping of the HA/Au sample after four hours reacting with UW. Individual element maps of O, Ca, P, and Si are also shown.

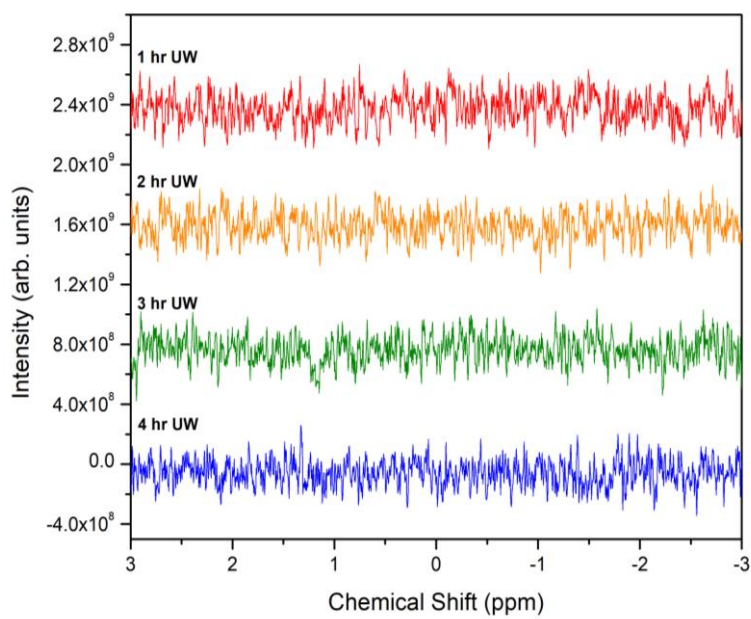


Fig. 5.8 ^1H -decoupled- ^{31}P -NMR spectra of UW at one hour intervals during reaction with HA at 298 K.

5.3 Data Analysis of Ammonium Formate-Water (AFW) on HA at 298 K

O-spectra from AFW and HA are depicted in Fig. 5.9, which also contains an inset from 1300-1000 cm^{-1} where PO stretches are found. In the reacted-spectra, the features in this region are less intense than in the bare HA spectrum, suggesting that the HA film has been dissolved by the AFW solution. This conclusion is supported by EDX analysis of the HA after reaction. The amount of P detected on the sample dropped from 3.69% to an undetectable amount (Table 5.2). The inset in Fig. 5.9 also shows a peak caused by the optical system in the experimental setup at $\sim 1230 \text{ cm}^{-1}$. Fig 5.10 contains R-spectra, where a spectrum was collected when no sample was in place as well as spectra for HA and Au. The spectrum with no sample contains a peak at $\sim 1230 \text{ cm}^{-1}$, suggesting that this feature is caused by the optical system.

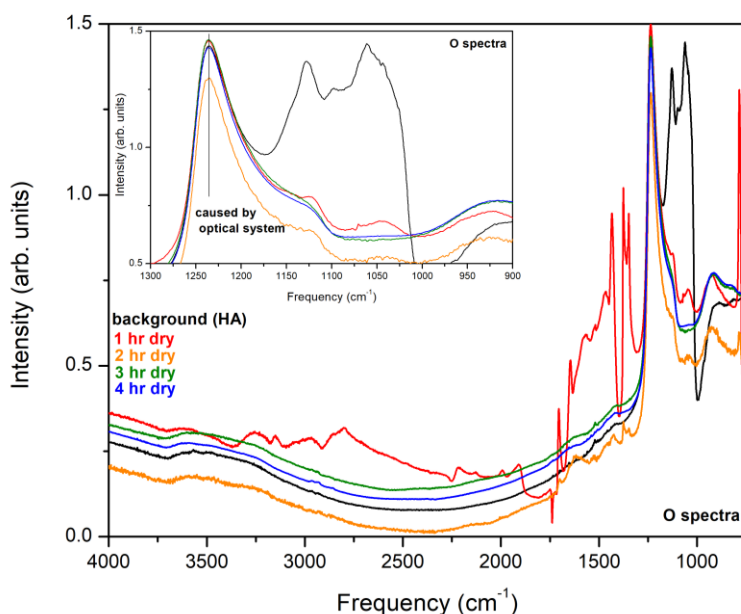


Fig. 5.9 PM-IRRAS spectra of AFW adsorbed to HA, reaction occurred with 6 mL of AFW at 298 K. O spectra from 4000-750 cm^{-1} , inset is a close up of PO stretches from 1300-1000 cm^{-1} .

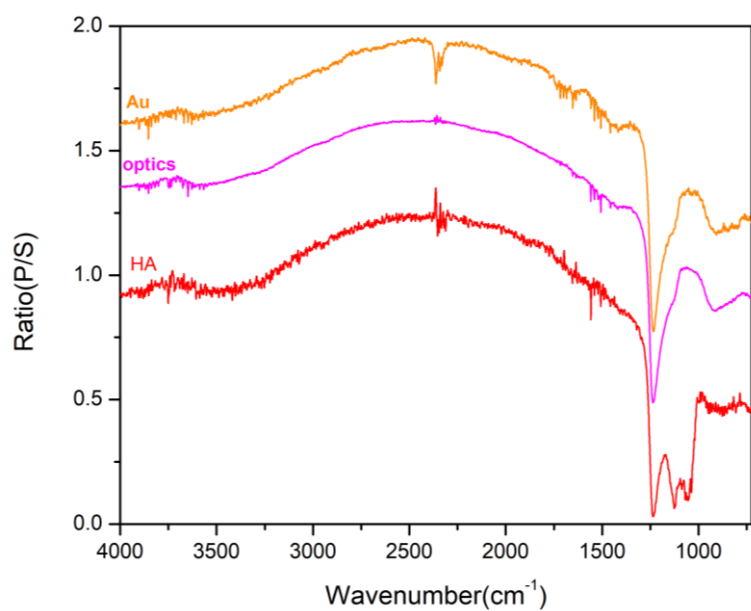


Fig. 5.10 PM-IRRAS R spectra of Au, optical system with no sample, and HA. Collected at room temperature.

Table 5.2 Elemental Analysis by EDX of HA/Au after a four hour reaction with ammonium formate/water at 298 K.

Formula	Atom % Pre-Reaction	Atom % Post-Reaction
C	8.31	52.69
O	63.35	37.10
Al	-	0.53
Si	13.25	8.59
P	3.69	-
Ca	5.92	-
Cr	0.50	0.37
Au	4.98	0.73
Total	100.00	100.00

Background corrected D-spectra are depicted in Fig. 5.11 in the regions of (A) 4000-2200 cm^{-1} and (B) 2200-750 cm^{-1} . The features observed in the one-hour spectrum shown in Fig. 5.11A vary significantly from the other reacted D-spectra and may have been caused by incomplete drying. While the spectra after one, three, and four hours of reaction were collected after 45 minutes of drying, the spectrum after two hours of reaction was collected after 90 minutes of drying because of an issue with the purge system. Since the spectrum for two hours was collected after a longer period of time drying, the peak at 2361 cm^{-1} , which dips below the baseline, was most likely created by water adsorbed to the mineral. The features at 2361, 2213 and 2176 cm^{-1} in the one-hour reaction spectrum are most likely due to POH stretches from the interaction of water and phosphate in the mineral. Since EDX analysis indicates no detection of P after four hours of reaction, features from ~ 3200 to ~ 2100 cm^{-1} must be a combination of POH stretches and other functional groups, which might be due to evaporation of ammonia. Features found at 2966 and 2797 cm^{-1} can be assigned to a combination of groups, including CH stretches from formate or possibly from P-OH stretches associated with the HA film, since these features were present on the film before reaction.^{174,184-186} There is an increased intensity for one hour, which appear to diminish in intensity between three and four hours as the reaction proceeds. The feature at 3150 in the one-hour reaction spectrum is likely a hydroxyl caused by water adsorption, since the spectrum for one-hour reaction appears to contain more solution.¹⁸⁷ Spectra for ammonium formate and water in Fig. 5.11 even after 45 minutes of drying, appear to contain solution on the surface, supported by the two-hour spectrum, which had an increased time for drying. R-spectra of a wet HA surface for the time dependent studies are depicted in Fig. 5.12,

specifically from 4000 to 2100 cm^{-1} to highlight the evaporation of ammonia. In Fig. 5.12, spectra for three and four hours do not contain any features from 3790 to 2530 (besides gas-phase water), unlike spectra for one and two hours, which have upward and downward facing peaks, respectively. This suggests that ammonia is evaporating off the surface and that the one hour spectrum contained more solution and was not quite as dry compared to two, three, and four hours.

Lower frequency values are illustrated in Fig. 5.11B. Peaks at 1737 and 1705 cm^{-1} are most likely due to the carbonyl on formate.¹⁸⁸ Peaks at 1644 and 1577 cm^{-1} are most likely from the COO^- and CO stretches of the formate.^{184,189} Features at 1470 and 1434 cm^{-1} can be attributed to a CH bend and an OCO stretch, respectively, while 1375 cm^{-1} is a combination of a CH bend and OCO stretch, 1348 cm^{-1} is likely an OCO stretch.¹⁸⁸⁻¹⁹⁰ Lastly, PO stretches from phosphate groups are attributed to features at 1311, 1095, and 1059 cm^{-1} .¹⁷⁴ Post-reaction analysis with NMR revealed phosphate in solution after two hours, suggesting that ammonium formate rather than urea plays a critical role in phosphate dissolution (Fig. 5.13). The spectra presented here suggest that AF and HA have a complex interaction that is highly sensitive to the amount of hydration present and the amount of evaporation that occurs. Given significant variations in the time-dependent spectra, additional replications of the experiment are necessary to fully characterize the AF and HA interaction.

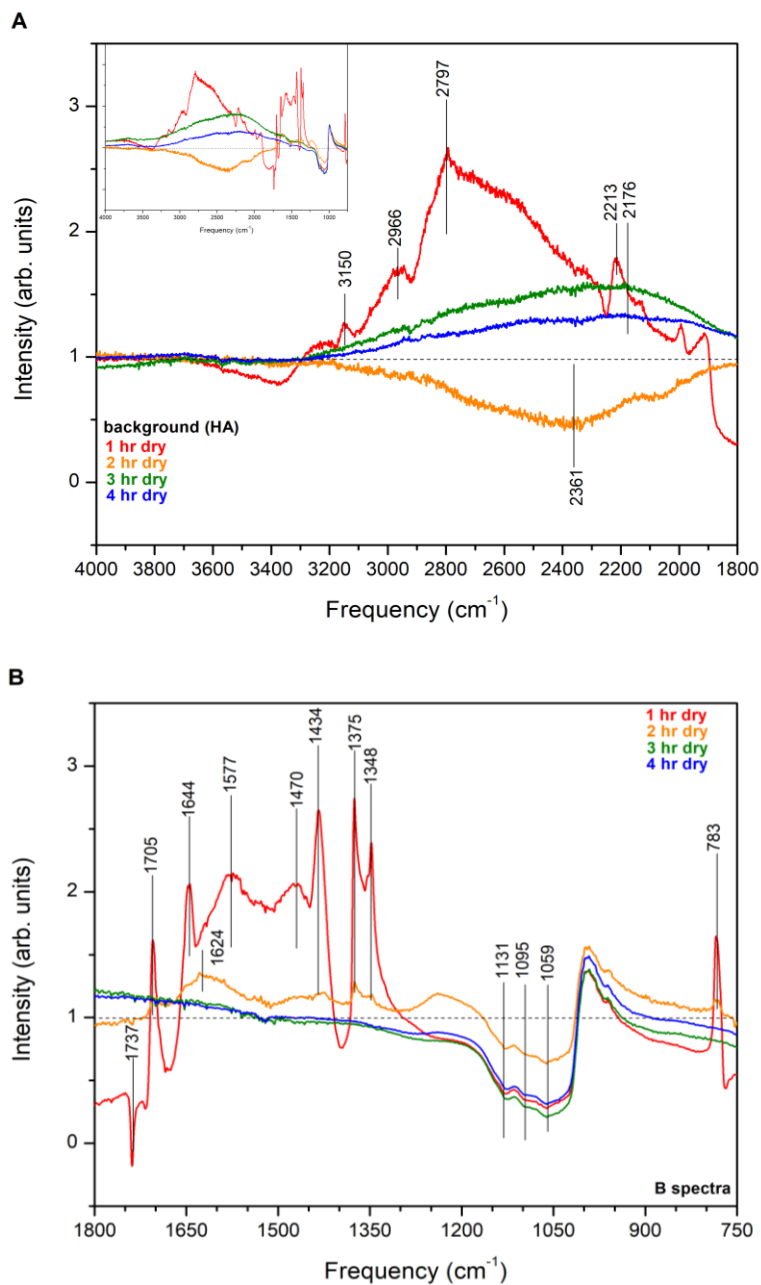


Fig. 5.11 PM-IRRAS B spectra (background corrected) of AFW adsorbed to HA, reaction occurred with 6 mL of UW at 298 K. A) 4000-2200 cm^{-1} , inset is an overview of the entire R spectra from 4000-750 cm^{-1} , B) 2200-750 cm^{-1} .

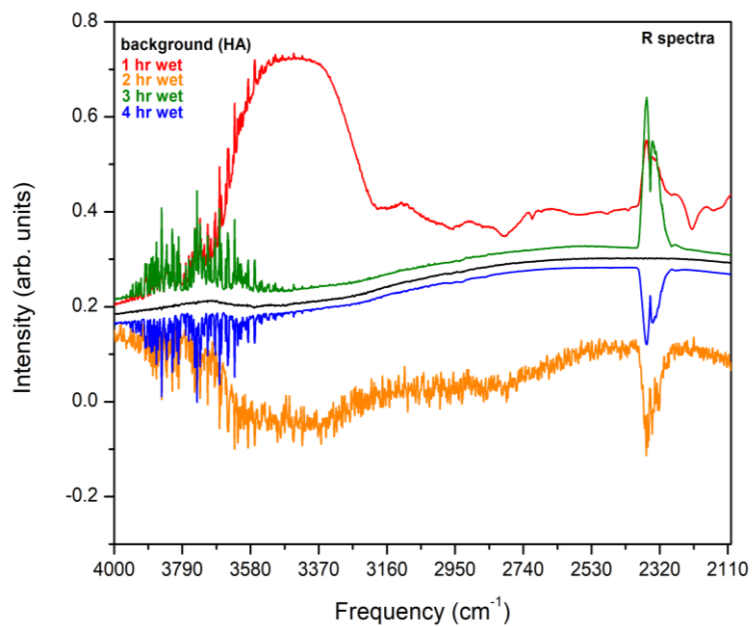


Fig. 5.12 PM-IRRAS R spectra of AFW adsorbed to a *wet* HA surface, from 4000-2100 cm^{-1} .

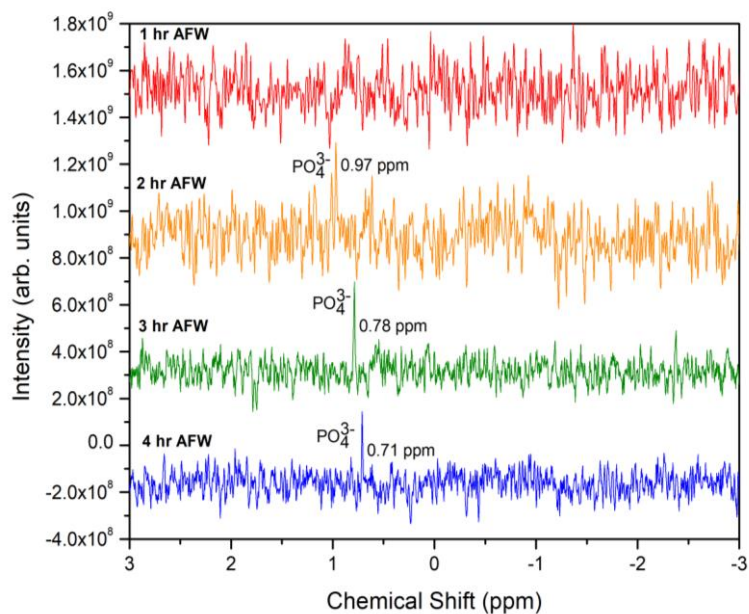


Fig. 5.13 ^1H -decoupled- ^{31}P -NMR spectra of AFW at one hour intervals during reaction with HA at 298 K.

5.4 Data Analysis of Urea-Ammonium Formate-Water (UAFW) on HA at 298 K

With spectral analysis of HA, W, UW, and AFW completed with assignments for most peaks, data for UAFW on HA was collected and features were assigned based on comparison to the control systems. Using the same conditions as previous experiments for AFW and UW, spectral data was collected and processed. Analysis of R-spectra suggests that the HA film reacted with the UAFW may have had some contamination, as illustrated in the black background spectrum in Fig. 5.14. The peak from 1765 to 1730 cm^{-1} is mostly commonly associated with carbonyl groups, possibly from carbonate contamination. Carbonate contamination is prevalent in hydroxyapatite as observed in Wang *et al.*¹⁹¹ Carbonate contamination was also observed in the electrochemical deposition method adapted from Thanh *et al.*,¹⁴⁰ A possible explanation for carbonate contamination is that CO_2 could have dissolved into the plating solution during electrochemical deposition and formed carbonic acid (H_2CO_3). The resulting H_2CO_3 then reacted with the calcium nitrate ($\text{Ca}(\text{NO}_3)_2$) in the plating solution to form calcium carbonate (CaCO_3), which precipitated onto the film. This can be avoided in future experiments by ensuring the flat-gold plated mirror is hung completely vertically, and thoroughly washing the surface of the film after it is removed from solution. Lower carbonate contamination levels were also achieved by using temperatures from 70-85°C compared to 60°C in Thanh *et al.*,¹⁴⁰

When analyzing B-spectra, spectral features were less pronounced as the reaction progressed to four hours, specifically from 4000 to 2000 cm^{-1} (Fig. 5.15). This is most likely due to HA dissolving in solution over time, as in the AFW experiment, and is

supported by post-reaction elemental analysis by EDX where no P and only 0.06% of Ca were detected on the gold-plated flat mirrors (Table 5.3). Peaks on UAFW corresponded to a combination of features assigned to HA, W, UW, and AFW in the previous sections. For example, the broad feature from 2718 to 2300 cm^{-1} may be a combination of CH stretches from formate, CH stretches from contamination of HA by acetone, and P-OH stretches on HA. The only features that appeared to not be found in any of the

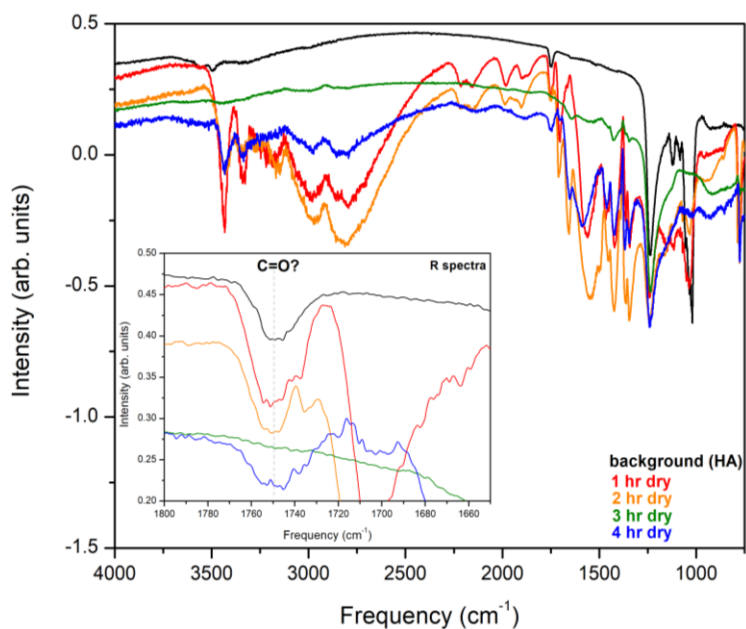


Fig. 5.14 PM-IRRAS R spectra of UAFW adsorbed to HA, reaction occurred with 6 mL of UAFW at 298 K. R spectra from 4000-750 cm^{-1} with an inset from 1800-1600 cm^{-1} .

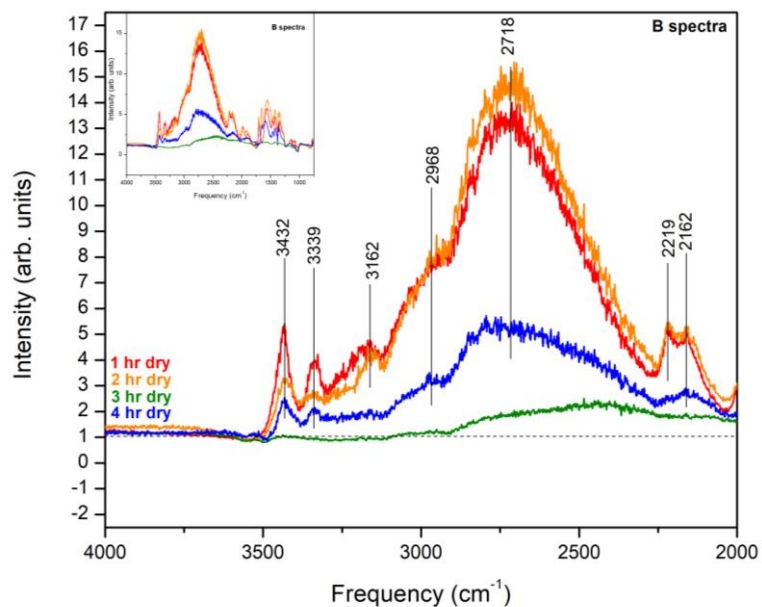


Fig. 5.15 PM-IRRAS B spectra of UAFW adsorbed to HA, reaction occurred with 6 mL of UAFW at 298 K. B spectra from 4000-2000 cm^{-1} with an inset from 4000-750 cm^{-1} .

components were at 1980 and 1881 cm^{-1} . After the data was re-analyzed, these peaks were found to be present in AFW. While a specific assignment is difficult to make without further studies, there is a possibility that these features are related to an organic contaminant such as carbonate.¹⁸⁸

Table 5.3 Elemental Analysis by EDX of HA/Au after a four hour reaction with urea, ammonium formate, and water at 298 K.

Formula	Atom % Pre- Reaction	Atom % Post- Reaction
C	6.52	30.66
N	--	30.59
O	66.70	37.55
Al	--	0.06
Si	6.80	0.55
P	6.25	--
Ca	8.73	0.06
Cr	0.32	0.03
Au	4.68	0.50
Total	100.00	100.00

Spectra for UW, AFW, and UW can be compared for the first hour of reaction, represented in Fig. 5.16 for one hour and Fig. 5.17 for four hour. The one-hour spectra for UW, AFW, and UAFW in Fig. 5.17 provide visual clarity, in terms of corresponding features found in UAFW to either AFW or/and UW. Comparison of one-hour spectra was chosen since both AFW and UAFW caused HA to dissolve off the surface, so interactions between the mineral surfaces were more apparent at one hour. Spectral features in UAFW are attributable to either ammonium formate, urea, or possible carbon contamination (C-H stretches at 1980 and 1881 cm^{-1}). Some features, such as 1638, 1588 cm^{-1} found on UW/HA and 1644, 1577 cm^{-1} for AFW/HA, are slightly more resolved compared to peaks in UAFW for this region, which are broader at 1566 cm^{-1} . Features at 1375 and 1348 cm^{-1} in AFW/HA are found for UAFW but are shifted to lower frequency values of 1363 and 1343 cm^{-1} , this might suggest different adsorption sites. In general,

most frequencies found in UAFW are attributed to its components in the previous control experiments with some slight spectral shifts.

An interesting aspect for UW/HA spectra is the region from 4000-2000 cm^{-1} in hour 4, compared to hour 1. The increased intensity for hour 4 in UW suggests these features may be caused by interaction of urea-water and HA. POH stretches were observed for W/HA between ~ 2700 to $\sim 2300 \text{ cm}^{-1}$, these were broad peaks, while in UW/HA these peaks around the same region but sharper. These sharper peaks could suggest that the interaction of urea with HA is enhancing these features. Additionally, HA remains on the surface for UW, which might explain why signal intensity does not decrease even at four hours.

No phosphate was observed in solution when HA reacted with UW, but phosphate was observed when HA reacted with AFW by NMR analysis. NMR-spectra indicates that phosphate was released after two hours with AFW/HA compared to one hour for UAFW/HA. This time dependence suggests improved solubility in UAFW compared to AFW, suggesting that ammonium formate and urea both play a role in phosphate solubility, with ammonium formate holding the primary role based on NMR analysis (Fig. 5.18). However, these NMR experiments would need to be repeated in order to establish this claim, which would be enhanced if P was quantified by ICP or phosphate quantification by NMR.

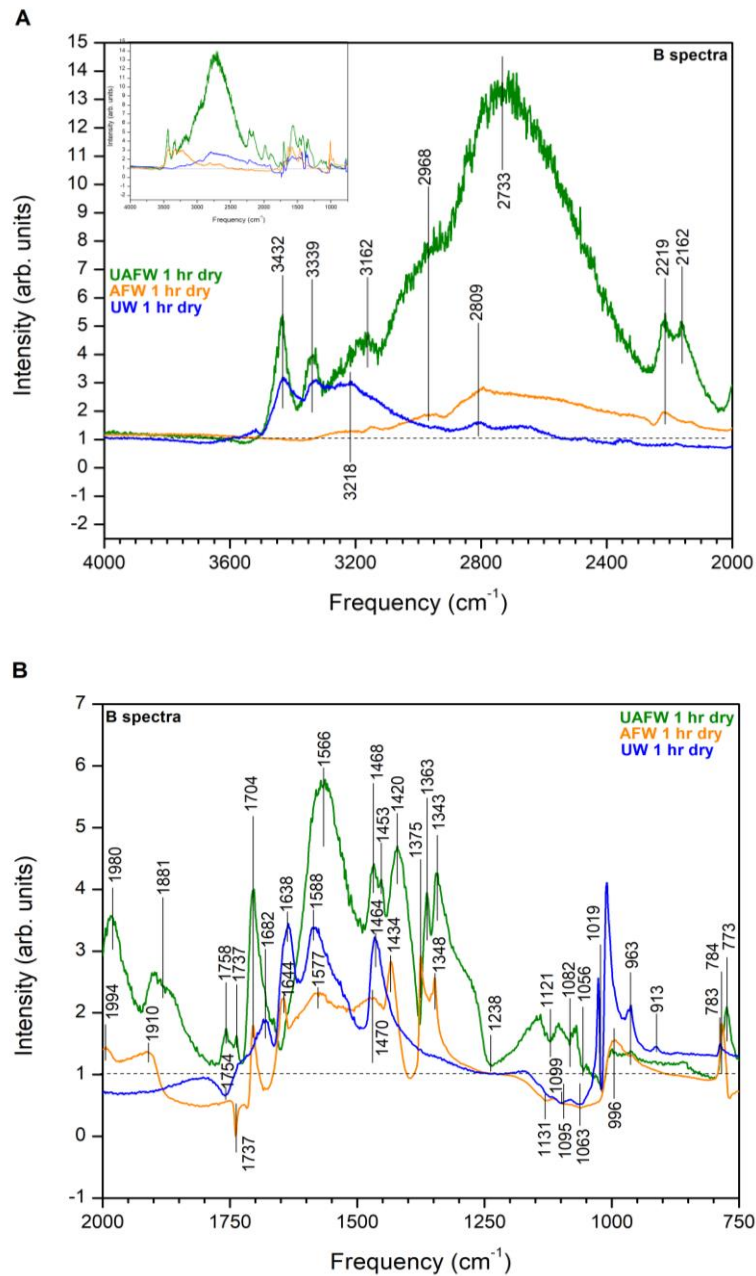


Fig. 5.16 Comparison of PM-IRRAS B spectra (background corrected) for UAFW, AFW, and UW adsorbed to HA for one hour at 298 K. B spectra from 4000-2000 cm^{-1} with an inset from 4000-750 cm^{-1} .

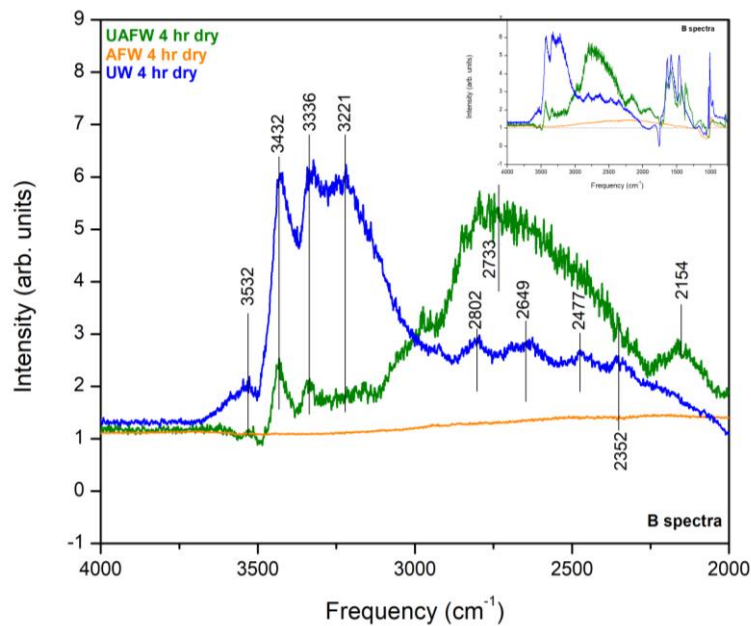


Fig. 5.17 Comparison of PM-IRRAS B spectra of UAFW, AFW, and UW adsorbed to HA for four hours at 298 K. B spectra from 4000-2000 cm^{-1} with an inset from 4000-750 cm^{-1} .

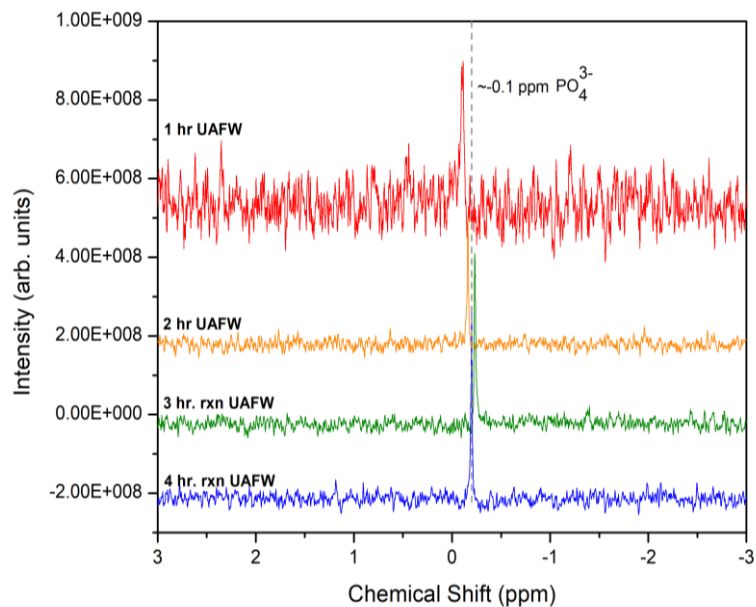


Fig. 5.18 ^{31}P NMR decoupled-spectra of UAFW at one hour intervals during reaction with HA at 298 K.

5.5 Data Analysis of MgSO₄ and UAFW on HA

After broad-spectral assignments for UAFW and an estimated time frame for phosphate release into solution were made, the next step involved investigating the effect of magnesium sulfate (MgSO₄) on the interaction of the UAFW with HA. Previous research has indicated that when MgSO₄ is added to UAFW, the amount of phosphorus in solution increases, although the form of this phosphorus may not necessarily be as phosphate.²¹ If P is released as phosphate then this ion has a strong affinity for divalent cations. These cations would most likely bind to magnesium ions and a magnesium phosphate compound is more soluble compared to a calcium phosphate compound.³² This ion exchange also produces more soluble phosphate due to the strong affinity of calcium for sulfate. Another role that MgSO₄ could play is in the mineral transformation of HA into more soluble phosphate minerals (*e.g.*, struvite, NH₄MgPO₄·6H₂O and newberyite, Mg(HPO₄)·3H₂O).^{22, 32} Previous reactivity experiments mentioned in Sections 5.1-5.4 used 6 mL of solution; for these experiments 6 mL and 10 mL solutions were used with 10 mL solutions providing the best results for PM-IRRAS (complete dissolution of MgSO₄).

Concentrations of 249 and 747 mM MgSO₄ in UAFW were used to observe changes in surface features and HA solubility as the concentration of MgSO₄ increased. Fig. 5.19 presents a comparison between these different concentrations and pure UAFW at one hour. In Fig.5.19A the spectrum for 249 mM MgSO₄ appears more intense compared to UAFW in the high frequency region because more water is present, which might be explained by MgSO₄ precipitating onto the film and absorbing water (MgSO₄ is hygroscopic). As the concentration of MgSO₄ increased, the solution became more

saturated and limited the dissolution of HA into solution. When the solution was very concentrated with MgSO₄, the sample lost infrared reflectivity and spectra became difficult to acquire because of low signal intensity. An SEM image of a 5 M MgSO₄ in UAFW solution is shown in Fig. 5.20. Cuboid-like structures formed with excess MgSO₄ and PM-IRRAS was not possible for this sample since it was very unreflective. Fig. 5.21 presents spectra of pure UAFW, 249 mM of MgSO₄ in UAFW, and 747 mM of MgSO₄ in UAFW in the spectra range of 2000 to 750 cm⁻¹. A majority of features found in the UAFW are also present in the low concentration MgSO₄ solution (*i.e.*, 249 mM) while some features are less intense in the high concentration MgSO₄ solution (*i.e.*, 747 mM). For example, peaks 1980 and 1881 cm⁻¹ appear on pure UAFW and of 249 mM MgSO₄ but are absent in 747 mM MgSO₄. Additionally, peaks have better resolution in UAFW, as an example peaks 1363 and 1343 cm⁻¹ are more resolved compared to similar features on 249 mM MgSO₄ at 1376 and 1348 cm⁻¹. Generally, peaks on the 747 mM MgSO₄ spectrum are broader and less intense, such as 1641 and 1577 cm⁻¹, which are more broad compared to the same features on UAFW and 249 mM MgSO₄ at 1577 and 1566 cm⁻¹ (see Fig. 5.21 C). A distinguishable spectral feature for the 747 mM MgSO₄ one hour spectrum is at 1083 cm⁻¹ which is less intense for the 249 mM and pure UAFW spectra (see Fig. 5.21 D). The feature at 1083 cm⁻¹ is found in the background spectra of the 249 mM and 747 mM MgSO₄ spectra (see Fig. 5.23D). However, it is not observed in the pure UAFW spectrum. The peak at 1083 cm⁻¹ is a PO stretch for HA and is present before reaction for reactivity experiments of 249 mM and 747 mM MgSO₄. Infrared features for MgSO₄ deposited onto the HA surface are not directly observed for the spectra collected, which may be attributed to two factors. One possibility is that peaks

associated with SO_4 (*e.g.*, 1123, 1172 and 946 cm^{-1}) are hidden because of PO stretches are found in this region.¹⁹² Another possibility is that the sulfate ion is sensitive to water; an anhydrous sample has less intense and decreased linewidth compared to liquid samples.¹⁹³

Although the synthesis of these films were performed under the same conditions, the HA films are not identical. Fig. 5.23 contains O-spectra with three HA background-spectra corresponding to each experiment (UAFW, 249 mM, and 747 mM MgSO_4). Generally, spectral features from $4000\text{-}1300\text{ cm}^{-1}$ do not appear on the background-spectra (*e.g.*, see Fig. 5.22 and 5.23). (*n.b.*, The intensity of infrared vibrational peaks does not scale with concentration, even if signal intensity is drastically different for each spectra.)

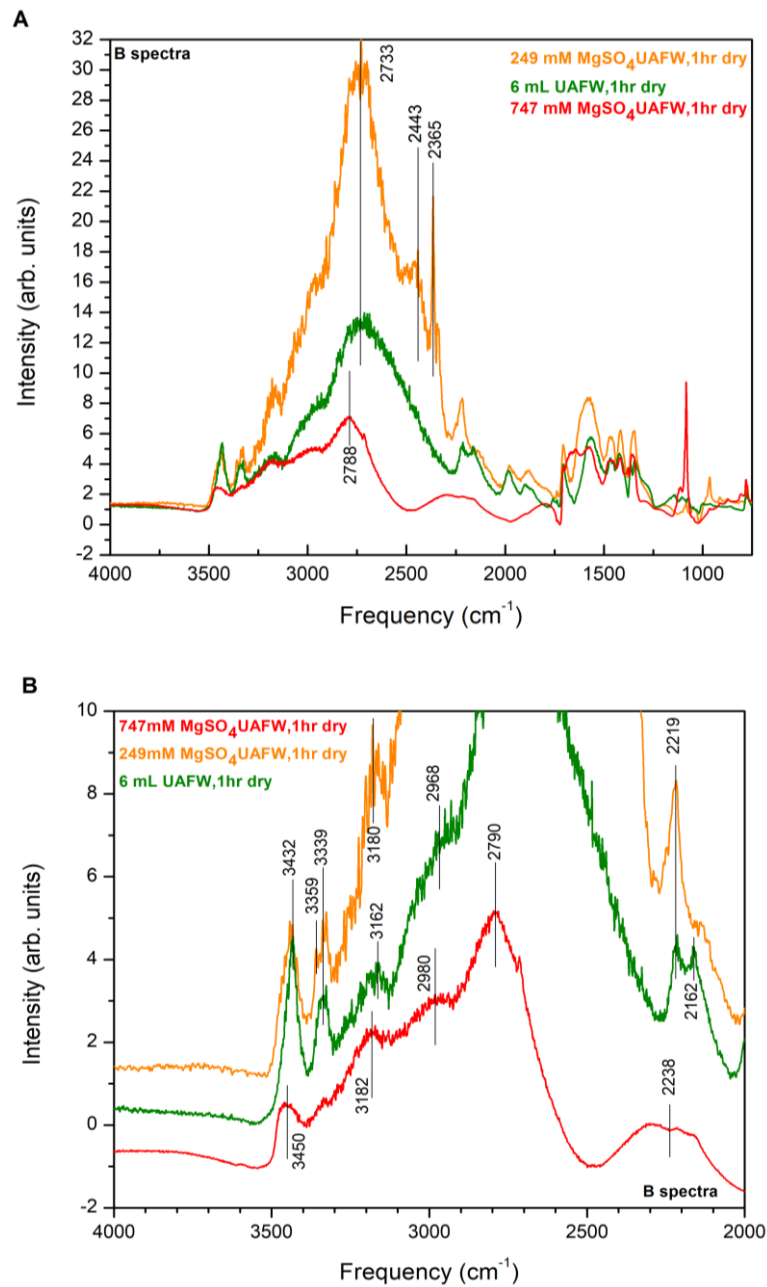


Fig. 5.19 PM-IRRAS B spectra of 249 mM MgSO₄ UAFW, 747 mM MgSO₄ UAFW, and UAFW adsorbed to HA at 298 K. A) spectra from 4000-750 cm⁻¹. B) spectra from 4000-2000 cm⁻¹.

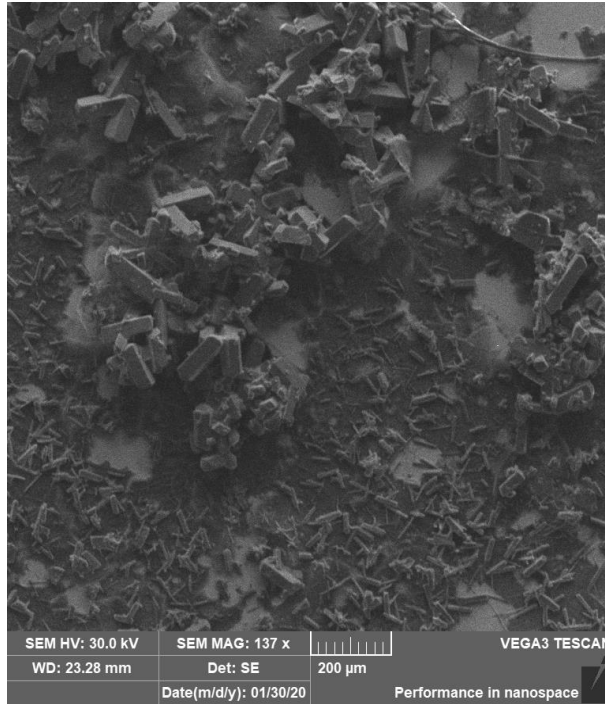


Fig. 5.20 SEM image of a HA/Au sample after a four hour reaction with a saturated MgSO_4 solution (5 M).

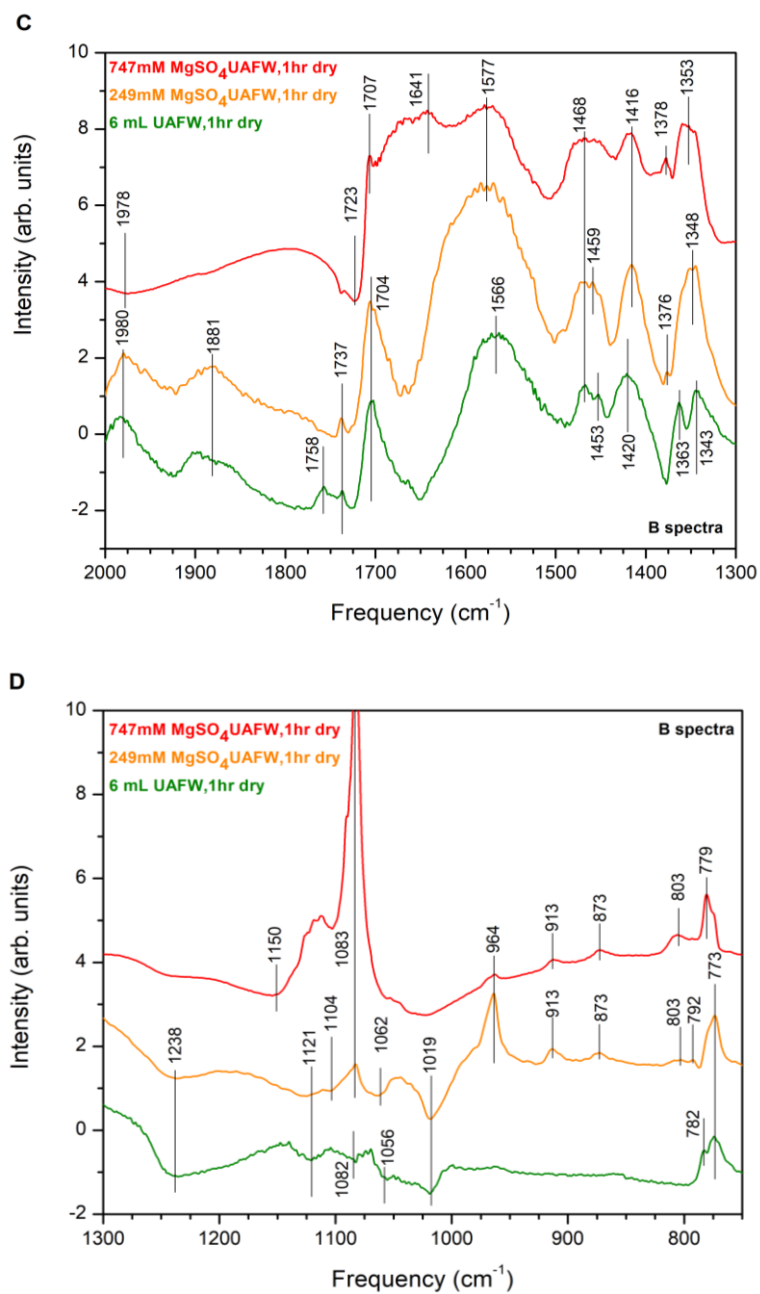


Fig. 5.21 PM-IRRAS B spectra of 249 mM MgSO_4 UAFW, 747 mM MgSO_4 UAFW, and UAFW adsorbed to HA at 298 K after one hour, C) spectra from 2000-1300 cm^{-1} . D) spectra from 1300-750 cm^{-1} .

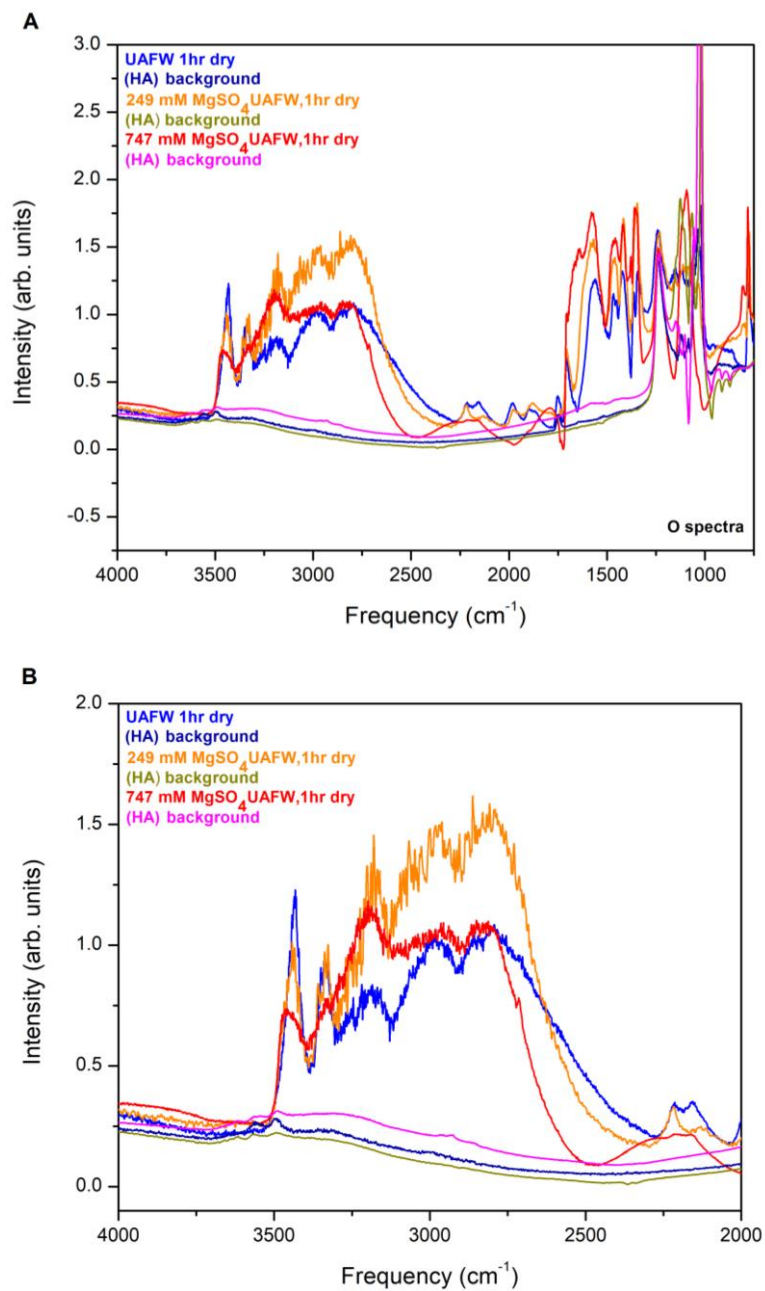


Fig. 5.22 PM-IRRAS O spectra of 249 mM MgSO_4 UAFW, 747 mM MgSO_4 UAFW, and UAFW adsorbed to HA at 298 K after one hour, A) spectra from 4000-750 cm^{-1} . B) spectra from 4000-2000 cm^{-1} .

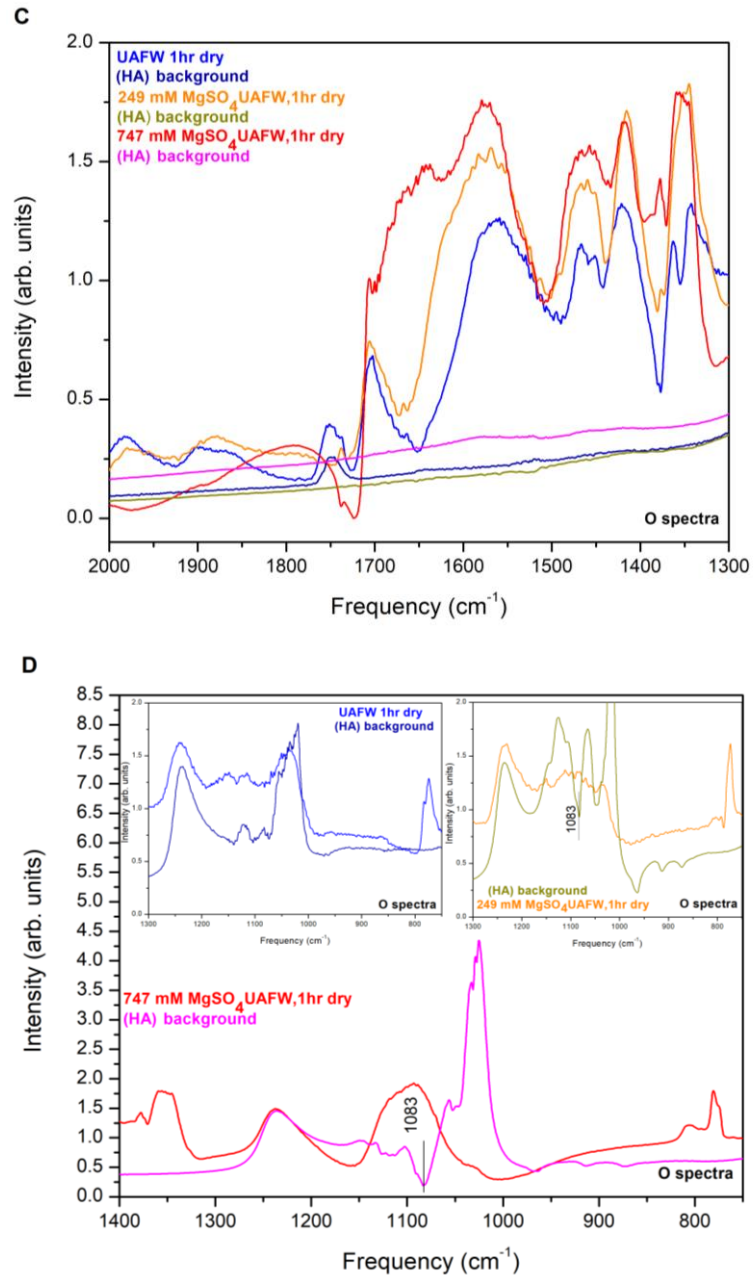


Fig. 5.23 PM-IRRAS O spectra of 249 mM MgSO_4 UAFW, 747 mM MgSO_4 UAFW, and UAFW adsorbed to HA at 298 K after one hour, C) spectra from 2000-1300 cm^{-1} . D) spectra from 1300-750 cm^{-1} .

Post-reaction analysis for 249 and 747 mM MgSO₄ was enhanced by EDX analysis (Table 5.4). The results show a significant amount of carbon, which is most likely attributable to a layer of organics on the mirror surface as a result of cleaning with acetone. After four hours of reaction in UAFW containing 249 mM of MgSO₄, Mg²⁺ remains on the surface, P was not detected, and only 0.01% of Ca was detected on the substrate. When HA reacted with AFW and UAFW, no solid was visible on the surface of the gold-plated mirror, but reactions with MgSO₄ did leave visible solid on the surface. Elemental mapping of the HA/Au sample after reaction with 249 mM of MgSO₄ indicates a solid on the surface at 5 mm. EDX performed on this solid at 250 μm revealed the solid's composition consisted of N, O, C, S, Mg, and Ca (see Fig. 5.24). For the sample exposed to UAFW with a concentration of 747 mM of MgSO₄, more solid remained on the surface of the gold-plated flat mirror compared to the 249 mM MgSO₄ solution. The solid remaining on the substrate after reaction with the high concentration of MgSO₄ was composed primarily of N, O, C and Mg (see Fig. 5.25).

NMR analysis of the supernatant was replicated twice for the solutions of 249 mM MgSO₄ without and with centrifuging and syringe filtering. Both experiments revealed phosphate in solution (see Fig. 5.26). NMR analysis was only replicated once for solutions of 747 mM MgSO₄ in UAFW, and there was no detection of P in solution by ³¹P-NMR (see Fig. 5.27). NMR analysis of solutions with higher concentration than 249 mM MgSO₄ (*i.e.*, 416 and 831 mM MgSO₄) detected phosphate in solution, and one- and two-hour NMR-spectra were only collected for 831 mM MgSO₄, because the solution became supersaturated (see Fig. 5.28). NMR analysis of the 747 mM MgSO₄ solution is

inconclusive based on these results and would need to be replicated in the future. A summary of relative assignments for PM-IRRAS peaks of HA, W, UW, AFW, UAFW, 249, and 747 mM MgSO₄ is presented in Tables 5.5, 5.6, and 5.7.

Table 5.4 Elemental Analysis by EDX of HA/Au after a four hour reaction with 249 mM MgSO₄ UAFW and 747 mM MgSO₄ UAFW at 298 K.

Formula	Atom % Pre- Reaction 249 mM a UAFW	Atom % Post- Reaction 249 mM MgSO₄ UAFW	Atom % Pre- Reaction 747 mM MgSO₄ UAFW	Atom % Post- Reaction 747 mM MgSO₄ UAFW
C	8.94	20.41	10.21	19.00
N	--	32.34	--	22.32
O	64.42	42.52	63.24	56.90
Si	9.18	0.08	8.10	--
S	--	1.45	--	--
Al	--	0.02	--	0.07
Tl	--	--	--	0.08
P	4.64	--	5.55	--
Ca	7.21	0.01	7.87	--
Cr	0.37	0.01	0.34	--
Au	5.24	0.21	4.70	0.02
Mg	--	2.94	--	1.61

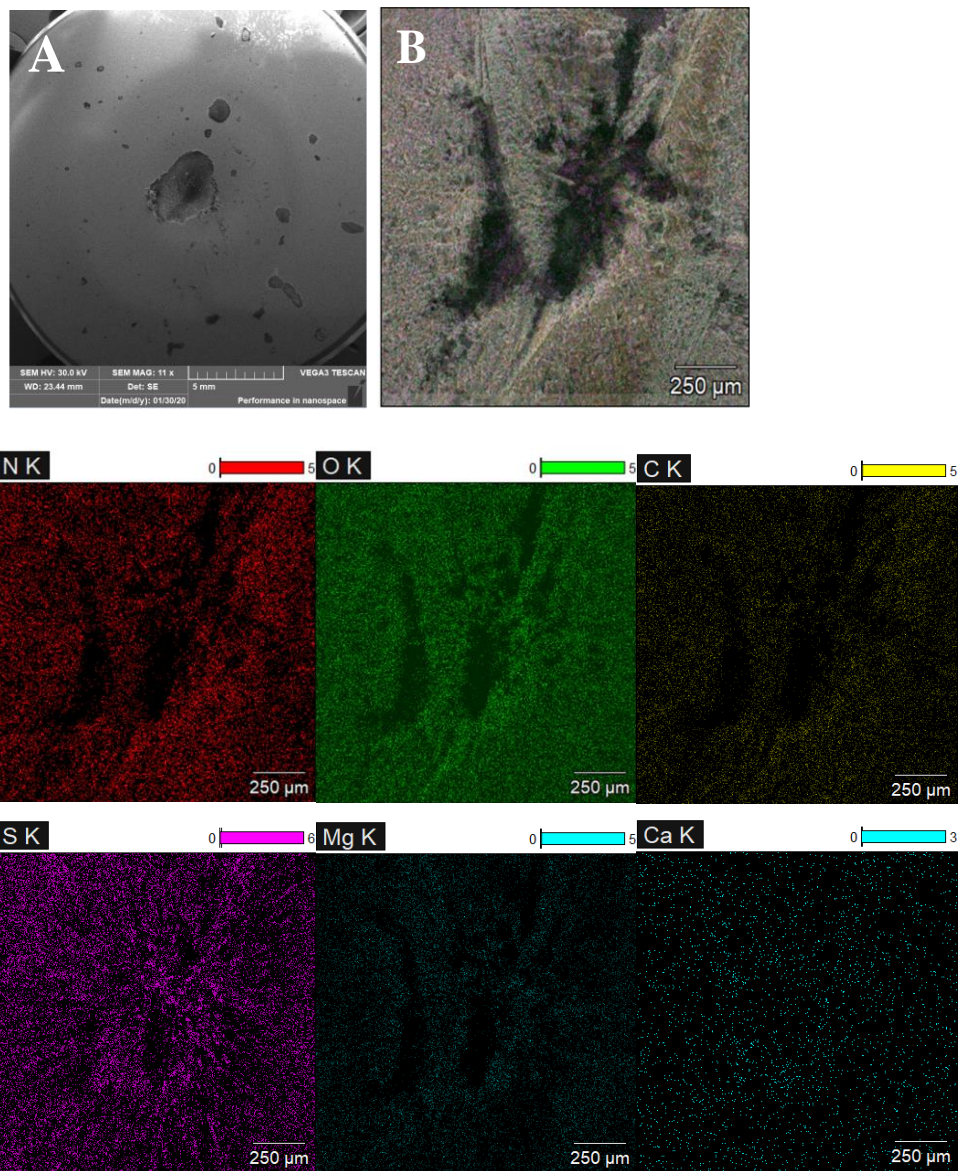


Fig. 5.24 EDX mapping of the HA/Au sample after a four hour reaction with 249 mM MgSO₄ UAFW at 298 K. A) HA/Au sample at 5 mm B) Center of the sample with solid present. Individual element maps of N, O, C, Si, Mg, and Ca are presented.

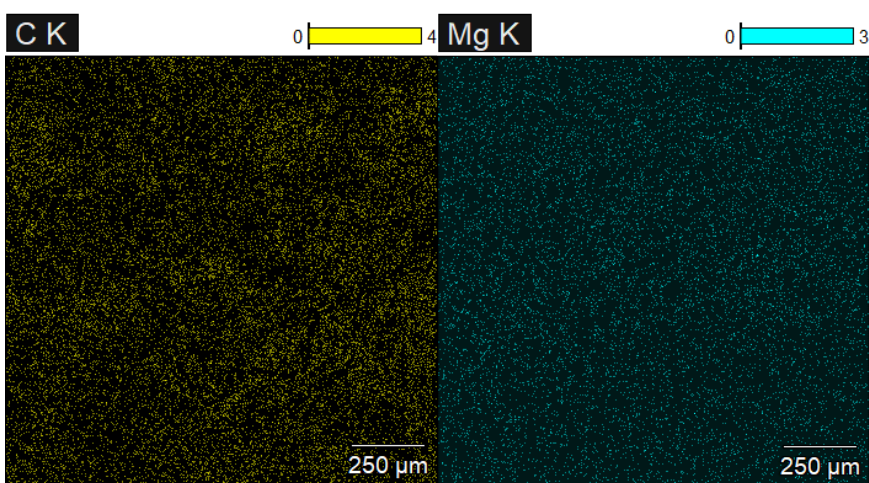
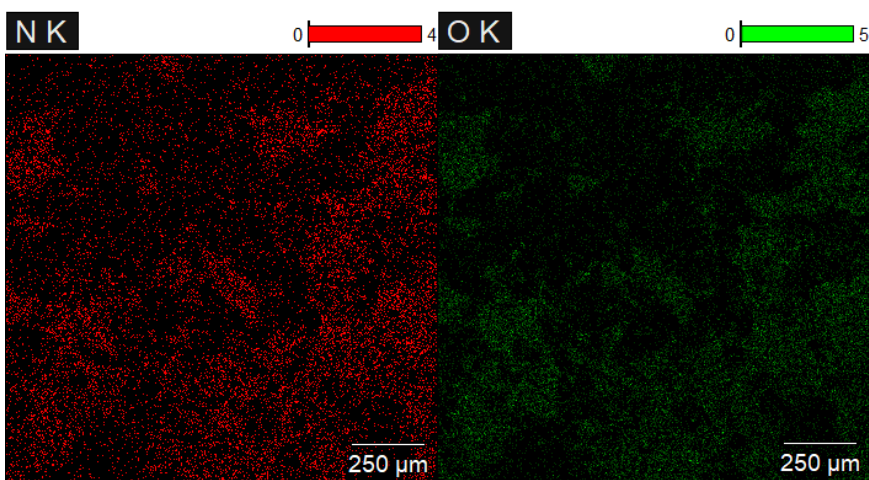
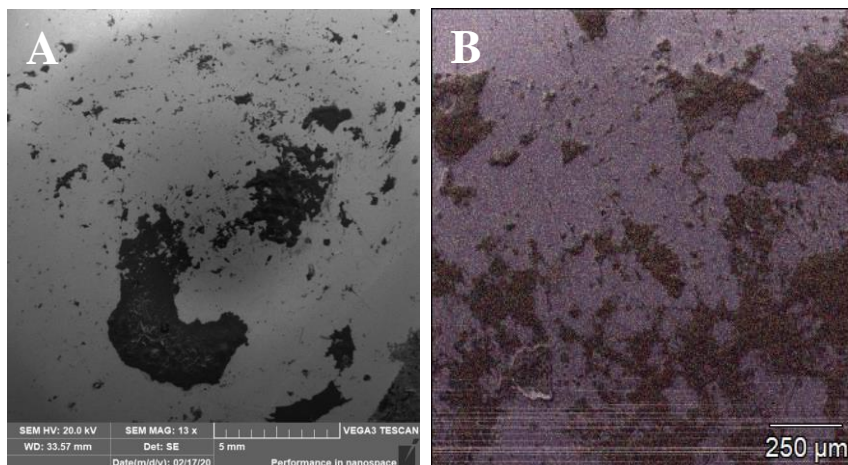


Fig. 5.25 EDX mapping of the HA/Au sample after a four hour reaction with 747 mM MgSO₄ UAFW at 298 K. A) HA/Au sample at 5 mm B) Center of the sample with solid present. Individual element maps of N, O, C, and Mg are presented. Purple represents Au.

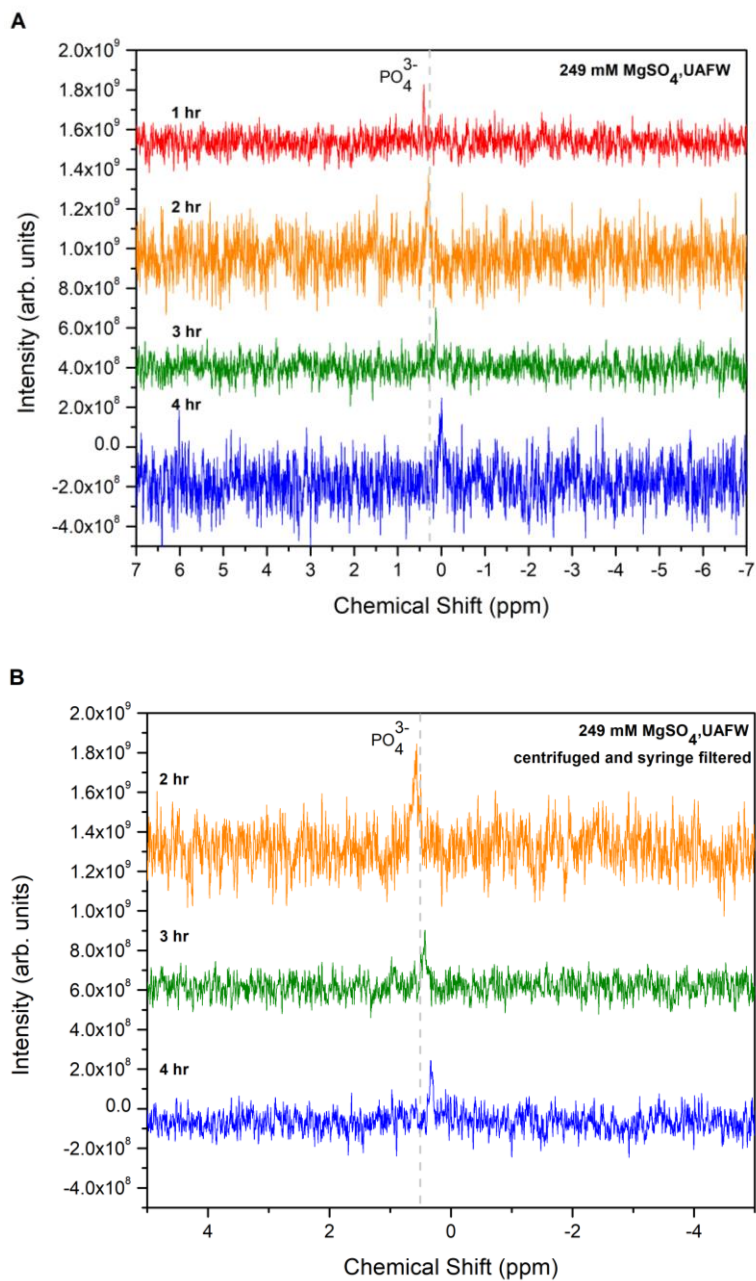


Fig. 5.26 ^{31}P NMR decoupled spectra of 249 mM MgSO_4 during reaction with HA at 298 K. A) Samples were not centrifuged or syringe filtered, B) Samples were centrifuged or syringe filtered.

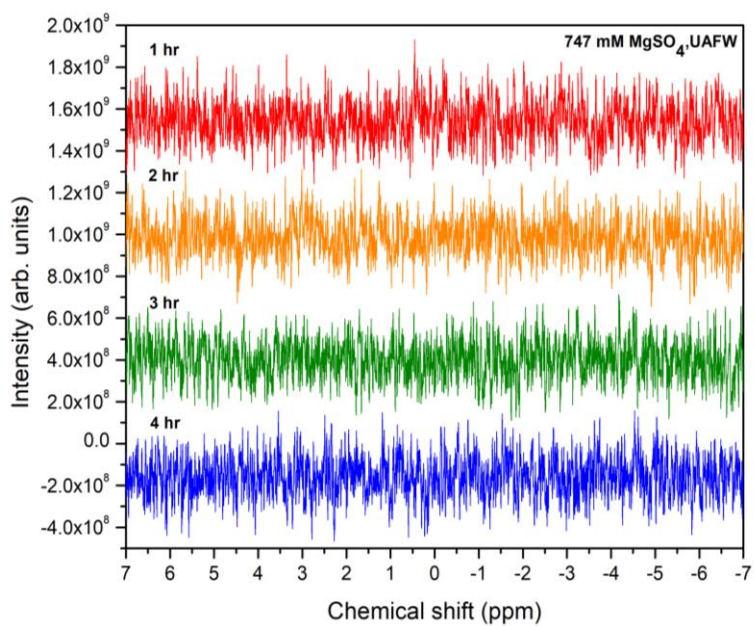


Fig. 5.27 ^{31}P NMR decoupled-spectra of 747 mM MgSO_4 during reaction with HA at 298 K.

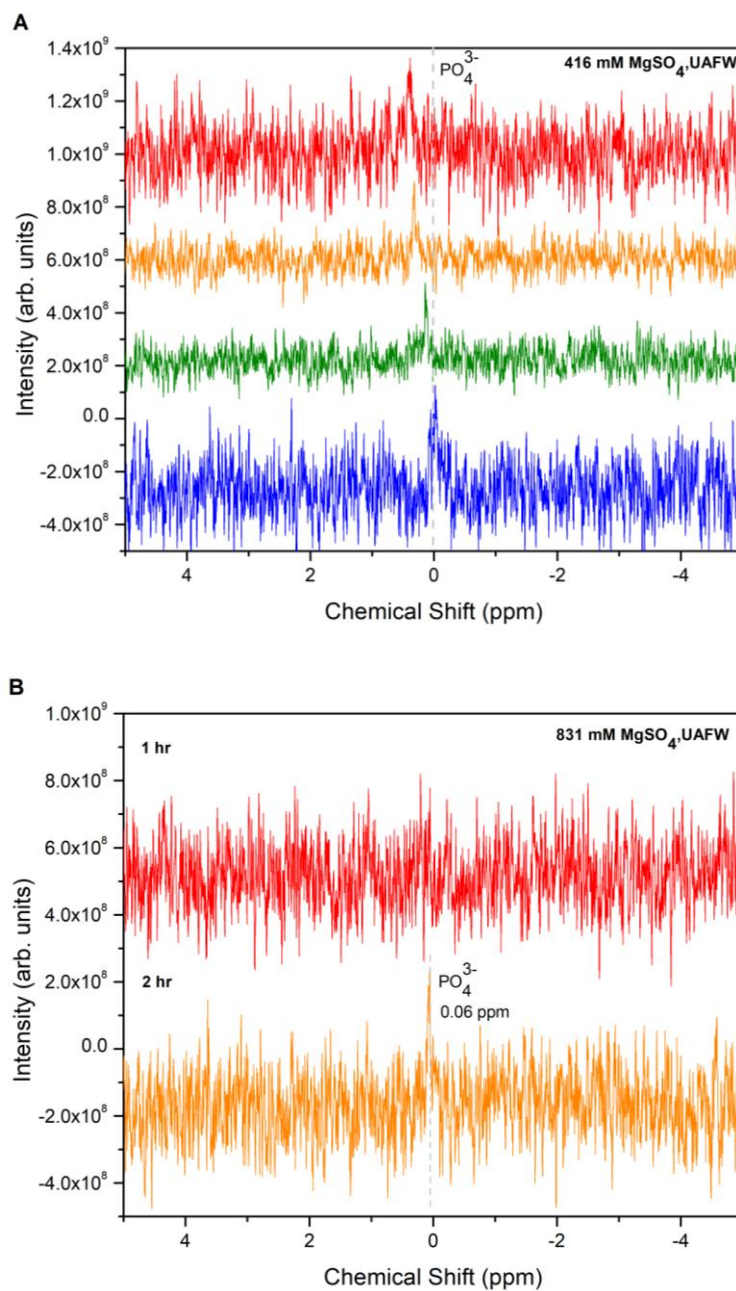


Fig. 5.28 ³¹P NMR decoupled spectra of: A) 416 mM MgSO₄ and B) 831 mM MgSO₄ during reaction with HA at 298 K.

Table 5.5 Summary of Vibrational assignments for HA, W, UW, AFW, UAFW, 249 and 747 mM MgSO₄ at 298 K for

1 hr dry PM-IRRAS baseline corrected spectra from 4000-2500 cm⁻¹.

Assigned Vibrations	HA (cm ⁻¹)	W/HA (cm ⁻¹)	AFW/HA (cm ⁻¹)	UW/HA (cm ⁻¹)	UAFW/HA (cm ⁻¹)	249 mM MgSO ₄ /HA (cm ⁻¹)	747 mM MgSO ₄ /HA (cm ⁻¹)	Reference (cm ⁻¹)
OH stretch	3612, 3551, 3488							3527 ¹⁷⁰ , 3476 ¹⁷⁰ , 3579 ¹⁷⁰
NH ₂ stretch and OH stretch				3527				3545 ¹⁷⁶ , 3548 ¹⁷⁷
NH ₂ stretch				3430 3330 3218	3434, 3339	3432, 3339, 3359	3450, 3339	3485 ¹⁷⁸ , 3449 ¹⁷⁹ 3440 ^{176,177} , 3352 ¹⁷⁸ , 3347 ¹⁷⁹ 3258-3265 ¹⁸⁰
OH stretch			3150		3162	3180	3182	3150 -3550 ¹⁸⁷
CH stretch	2915, 2848		2966		2968	2968	2980	2959 ¹⁸⁴
POH stretch and CH stretch			2797	2798, 2636	2733	2733	2790, 2788	~2800 ¹⁸⁴ , 2801 ¹⁸⁵ , 2841 ¹⁸⁶ , 2870 ¹⁸⁶ , 2725-1600 ¹⁷⁴

Table 5.6 Summary of Vibrational assignments for HA, W, UW, AFW, UAFW, 249 and 747 mM MgSO₄ at 298 K for 1 hr dry PM-IRRAS baseline corrected spectra for 2500-1600 cm⁻¹.

Assigned Vibrations	HA (cm ⁻¹)	W/HA (cm ⁻¹)	AFW/HA (cm ⁻¹)	UW/HA (cm ⁻¹)	UAFW/HA (cm ⁻¹)	249 mM MgSO ₄ /HA (cm ⁻¹)	747 mM MgSO ₄ /HA (cm ⁻¹)	Reference (cm ⁻¹)
POH stretch	2459, 2364, 2327	2469, 2354				2443, 2365		2725-1600 ¹⁷⁴
POH stretch			2213, 2176		2219, 2162	2219, 2162	2238	2725-1600 ¹⁷⁴
CO stretch, carbonate (contamination?)				1980, 1881	1980, 1881	1980, 1881	1978	1956 ¹⁸⁸ , 1852 ¹⁸⁸ , 1936 ¹⁸⁸ , 1850 ¹⁸⁸
C=O stretch	1754		1737, 1705		1758, 1737, 1704	1737, 1704	1723 (loss), 1707	1730 ¹⁸⁸ , 1705 ¹⁸⁸
C=O stretch and C-N symmetric stretch		1754, 1682		1758, 1737, 1704	1758, 1737, 1704	1737, 1704	1723 (loss), 1707	1734 ¹⁷⁷ , 1615 ¹⁷⁸ , 1687 ¹⁷⁹ , 1749 ¹⁸² , 1740 ¹⁷⁶
COO stretch			1624, 1644					1630 ¹⁸⁸

Table 5.7 Summary of Vibrational assignments for HA, W, UW, AFW, UAFW, 249 and 747 mM MgSO₄ at 298 K for 1 hr dry PM-IRRAS baseline corrected spectra for 1600-1300 cm⁻¹.

Assignment	HA (cm ⁻¹)	W (cm ⁻¹)	AFW/HA (cm ⁻¹)	UW/HA (cm ⁻¹)	UAFW/HA (cm ⁻¹)	249 mM MgSO ₄ /HA (cm ⁻¹)	747 mM MgSO ₄ /HA (cm ⁻¹)	Reference (cm ⁻¹)
NH ₂ bend				1638, 1585				1638 ¹⁸² , 1657 ¹⁸² , 1590 ¹⁷⁷ , 1594 ¹⁷⁷ ,1615 ¹⁷⁸ , ,1632 ¹⁷⁹ ,1606 ¹⁷⁹
CO stretch and COO stretch		1577		1577	1577	1577	1641, 1577	1580 ¹⁸⁹ , 1536 ¹⁸⁸ ,1390 ¹⁸⁸ , 1590 ¹⁸⁸
CH bend		1470		1468, 1453	1468, 1459	1468	1460 ¹⁹⁰	
C-N + C=O bend + NH ₂ rock			1464	1468, 1453	1468, 1459	1468		1461 ¹⁸² , 1393 ¹⁷⁶ , 1394 ¹⁷⁷ , 1463 ¹⁷⁸ , 1467 ¹⁷⁹
OCO stretch		1434		1420	1416	1416	1440 – 1360 ¹⁹⁰	1381 ¹⁸⁹ , 1380 ¹⁸⁸ , 1440- 1360 ¹⁹⁰ ,1360 ¹⁹⁴
CH bend or OCO stretch		1375		1363	1376	1378		

Table 5.8 Summary of Vibrational assignments for HA, W, UW, AFW, UAFW, 249 and 747 mM MgSO₄ at 298 K

for 1 hr dry PM-IRRAS baseline corrected spectra for 1300-750 cm⁻¹.

Assignment	HA (cm ⁻¹)	W (cm ⁻¹)	AFW/HA (cm ⁻¹)	UW/HA (cm ⁻¹)	UAFW/HA (cm ⁻¹)	249 mM MgSO ₄ /HA (cm ⁻¹)	747 mM MgSO ₄ /HA (cm ⁻¹)	Reference (cm ⁻¹)
OCO stretch; PO stretch (1311)			1348, 1311		1343	1348	1353	1348 ¹⁹⁴ , 1360 ¹⁹⁴ , 1374 ¹⁹⁴ , 1358 ¹⁹⁴ , 1330 ¹⁹⁰
PO stretch	1237, 1127, 1085, 1020		1095, 1063	1099, 1060, 1010	1238, 1104, 1082, 1056, 1019	1308, 1238, 1121, 1104, 1083, 1062, 1019	1308, 1238, 1150, 1104, 1083, 1019	1155 ¹⁷³ , 1320-1140 ¹⁷⁴ , 1100-900 ¹⁷⁵
P-OH bend or PO stretch	964			963		964	964	949 ¹⁷⁵ , 965 ¹⁸³ , 912 ¹⁸³
PO stretch or OH	913		913			913	913	912 ¹⁸³
Carbonate vibrational band						873	873	873 ¹⁹⁵
MgCO ₃ feature?						803	803	803 ¹⁹⁶
OCO bend; CO out of plane bend			783	786	773, 782	773, 792	779	778 ¹⁸² , 785 ¹⁷⁶ , 790 ¹⁷⁷

CHAPTER 6. CONCLUSION AND FUTURE WORK

This study investigated surface interactions of hydroxyapatite (HA), a prebiotic plausible phosphate mineral source on the early Earth, with urea-rich solvents and magnesium sulfate. Synthesis of HA was performed by electrochemical deposition with a gold-plated flat mirror serving as the substrate. PM-IRRAS, a polarization modulation infrared technique, was developed and enhanced for these surface-sensitive studies. A liquid-solid cell was built and altered along with a purge and optical system, serving to enhance infrared signal and limit interference from background gases such as H₂O and CO₂. The mineral surface was characterized prior to reaction by SEM/EDX and PM-IRRAS. SEM/EDX analysis revealed a porous, thin, phosphate film on the surface and confirmed the presence of calcium and phosphorus. PM-IRRAS analysis prior to reaction suggested that hydroxyls have multiple orientations on the mineral surface and that carbonate may be a minor contaminant on the surface. Reactivity studies focused on reactions of HA with urea-rich solvents up to four hours. Infrared analysis of the surface was performed with dried samples. Based on reactions with water, urea-water, and ammonium formate-water at room temperature, features of a 1:2:4 urea/ammonium formate/water solution were roughly assigned when this solution was adsorbed to HA. It was found that ammonium formate binds to HA to mobilize phosphate and increase dissolution. This result was corroborated by proton decoupled ³¹P NMR analysis. Addition of MgSO₄ revealed similar PM-IRRAS results as that of UAFW, but as the

concentration of MgSO_4 increased, solid (most likely precipitated MgSO_4) remained on the metal substrate.

Surface chemistry is complex. Solid materials do not always have a well-ordered crystalline surface, and even when they do, it can still be challenging to interpret their reactivity as discussed in Chapter 1. Synthesizing and studying single macroscopic crystal surfaces allows for facile analysis of molecular adsorption, since these surfaces are well-ordered. Single crystals are cut in specific orientations, creating surfaces with a high degree of order (periodicity) and simple structure. Various single crystals of metal can be synthesized and contamination (*e.g.*, oxidation) may be minimized by using ultrahigh vacuum chambers (UHV).¹¹³ For this project, growth of single-crystal phosphate films on a metal substrate would have been time and cost exhaustive. It would have required matching lattice parameters in the hydroxyapatite and the underlying metal, adding a considerable layer of complexity to the project. While the ultrathin use in this work were porous and not completely consistent between batches, they were very representative of the imperfection of natural minerals, which are also porous and irregular.

Future steps will include isotopic experiments to clarify the assignments based on spectral shifts. Additionally, inconsistencies between spectra necessitate several replications of the: 1) PM-IRRAS experiments and 2) NMR experiments when MgSO_4 is added. Phosphorus quantification with inductively coupled plasma optical emission spectroscopy (ICP-OES) would also aid in the interpretation of the infrared assignments. Quantification of phosphorus would enhance supernatant analysis and determine if more phosphorus is released when AFW or UAFW interacts with hydroxyapatite. An

additional modification to this study would be a liquid-solid cell re-design for *in situ* experiments at variable temperatures.

REFERENCES

- ¹ Sagan, C. *Pale Blue Dot: A Vision of the Human Future in Space*; Ballantine Books, 1997.
- ² Shaw, M. A. *Astrochemistry: From Astronomy to Astrobiology*; Wiley, 2006.
- ³ Nemchin, A. A.; Pidgeon, R. T.; Whitehouse, M. J. Re-evaluation of the origin and evolution of > 4.2 Ga zircons from the Jack Hills metasedimentary rocks. *Earth Planet. Sci. Lett.* **2006**, *244* (1-2), 218.
- ⁴ Kruczynski, W. L.; Fletcher, P. J. *Tropical Connections South Florida's Marine Environments* **2012**, 19.
- ⁵ Kasting, J. F. Earths Early Atmosphere. *Science* **1993**, *259* (5097), 920-926.
- ⁶ Seewald, J. S.; Zolotov, M. Y.; McCollum, T. Experimental investigation of single carbon compounds under hydrothermal conditions. *Geochim. Cosmochim. Acta* **2006**, *70* (2), 446.
- ⁷ Kelley, D. S.; Karson, J. A.; Fruh-Green, G. L.; Yoerger, D. R.; Shank, T. M.; Butterfield, D. A.; Hayes, J. M.; Schrenk, M. O.; Olson, E. J.; Proskurowski, G.; Jakuba, M.; Bradley, A.; Larson, B.; Ludwig, K.; Glickson, D.; Buckman, K.; Bradley, A. S.; Brazelton, W. J.; Roe, K.; Elend, M. J.; Delacour, A.; Bernasconi, S. M.; Lilley, M. D.; Baross, J. A.; Summons, R. T.; Sylva, S. P. A Serpentinite-Hosted Ecosystem: The Lost City Hydrothermal Field. *Science* **2005**, *307* (5714), 1428.

- ⁸. Shaw, G. H. Earth's atmosphere – Hadean to early Proterozoic. *Chemie der Erde* **2008** 68 (3), 235.
- ⁹. Arndt, T.N. *Archean Crustal Evolution*, ed. By K.C. Condie; Elsevier Science, 1994.
- ¹⁰. Kamber, B. S. The evolving nature of terrestrial crust from the Hadean, through the Archaean, into the Proterozoic. *Precambrian Res.* **2015**, 258, 48.
- ¹¹. Miller, S. L. A production of Amino Acids under Possible Primitive Earth Conditions. *Science* **1953** 117 (3046), 528-529.
- ¹². De Duve, C. *Vital Dust: Life as a Cosmic Imperative*; Basic Books, **1995**, 362.
- ¹³. Parker, E. T.; Cleaves, J. H.; Burton, A. S.; Glavin, D. P.; Dworkin, J. P.; Zhou, M.; Bada, J. L.; Fernández, F. M. Conducting Miller-Urey Experiments. *Journal of Visualized Experiments* **2014**, (83).
- ¹⁴. Pasek, M. A.; Gull, M.; Herschy, B. Phosphorylation on the early Earth. *Chemical Geology* **2017**, 475, 149-170.
- ¹⁵. Breslow, R. On the mechanism of the formose reaction. *Tetrahedron Lett.* **1959**, 1 (21), 22-26.
- ¹⁶. Oro, J.; Basile, B.; Cortes, S.; Shen, C.; Yamrom, T. The prebiotic synthesis and catalytic role of imidazoles and other condensing agents. *Orig. Life* **1984** 14 (1-4), 237-242.
- ¹⁷. Orgel, L. E. Prebiotic chemistry and the origin of the RNA world. *Crit. Rev. Biochem. Mol. Biol.* **2004** 39 (2), 99-123.
- ¹⁸. Hazen, R. M.; Sverjensky, D. A. Mineral surfaces, geochemical complexities, and the origins of life. *Cold Spring Harb. Perspect. Biol.* **2010** 2 (5), 1-22.

- ¹⁹. Bohnen, H.-W.; Cornils, B. Hydroformylation of alkenes: An industrial view of the status and importance. *Adv. Synth. Catal.* **2002**, *47* (1).
- ²⁰. Vries, J. G. D.; Jackson, S. D. Homogeneous and Heterogeneous Catalysis in Industry. *Catalysis Science & Technology* **2012**, *2* (10), 2009.
- ²¹. Lago, J.; Burcar, B.; Hud, N. V.; Febrian, R.; Mehta, C.; Bracher, P. J.; Atlas, Z. D.; Pasek, M. A. The Prebiotic Provenance of Semi-Aqueous Solvents. Origins of Life and Evolution of Biospheres **2020**, *in review*.
- ²². Burcar, B.; Castañeda, A.; Lago, J.; Daniel, M.; Pasek, M.; Orlando, T.; Hud, N. V.; Menor-Salvàn, C. A Stark Contrast to Modern Earth: Phosphate Mineral Transformation and Nucleoside Phosphorylation in an Iron- and Cyanide-Rich Early Earth Scenario. *Angew. Chem.* **2019** *58* (47). 16981-16987.
- ²³. Horiguchi, M.; Kandatsu, M. Isolation of 2-aminoethane phosphonic acid from rumen protozoa. *Nature* **1959**, *184* (4690), 901-902.
- ²⁴. Srinivasan, V.; Morowitz, H. J. Analysis of the intermediary metabolism of a reductive chemoautotroph. *Biol. Bull.* **2009**, *217* (3), 222–232.
- ²⁵. Westheimer, F. H. Why nature chose phosphates. *Science* **1987**, *235* (4793), 1173-1178.
- ²⁶. Pasek, M. A.; Kee, T. P. On the Origin of Phosphorylated Biomolecules. In *Origins of Life: The Primal Self-Organization*; Egel, R.; Lankenau, D. H.; Mulkiđjanian, A.Y.; Eds.; Springer-Verlag: Berlin/Heidelberg, Germany, 2011; 57–84.
- ²⁷. Benner, S. A.; Ricard, A.; Carrigan, M. A. Is there a common chemical model for life in the universe? *Curr. Opin. Chem. Biol.* **2004**, *8* (6), 672-689.

- ²⁸. Davis, B. D. On the importance of being ionized. *Arch. Biochem. Biophys.* **1958**, 78 (2), 497–509.
- ²⁹. Orgel, L. E. Was RNA the first genetic polymer? **1989**, In: Evolutionary Tinkering in Gene Expression, Springer US, 215-224.
- ³⁰. Hermanson, G.T. *Bioconjugate Techniques*; 3rd ed., Academic Press, London, 2013, 1146.
- ³¹. Lohrmann, R.; Orgel, L. E. Prebiotic Synthesis: Phosphorylation in Aqueous Solution. *Science* **1968**, 161 (3836), 64–66.
- ³². Burcar, B.; Pasek, M.; Gull, M.; Cafferty, B.J.; Velasco, F.; Hud, N.V.; Menor-Salvan, C. Darwin's Warm Little Pond: A One-Pot Reaction for Prebiotic Phosphorylation and the Mobilization of Phosphate from Minerals in a Urea-Based Solvent. *Ang. Chem. Int.* **2016**, 55 (42), 13249-13253.
- ³³. Schoffstall, A. M.; Laing, E. M. Phosphorylation Mechanisms in Chemical Evolution. *Origins of Life and Evolution of the Biosphere* **1985**, 15 (2), 141–150.
- ³⁴. Nelson, D. L.; Lehninger, A. L.; Cox, M. M. *Lehninger Principles of Biochemistry* **2008**.
- ³⁵. Benner, S. A.; Kim, H. J.; Carrigan, M. A. Asphalt, water, and the prebiotic synthesis of ribose, ribonucleosides, and RNA. *Acc. Chem. Res.* **2012**, 45 (12), 2025-2034.
- ³⁶. Cafferty, B. J.; Hud, N. V. Abiotic synthesis of RNA in water: a common goal of prebiotic chemistry and bottom-up synthetic biology. *Curr. Opin. Chem. Biol.* **2014**, 22, 146-157.
- ³⁷. Rabinowitz, J.; Woeller, F.; Flores, J.; Krebsbach, R. Electric discharge reactions in mixtures of phosphine, methane, ammonia and water. *Nature* **1969**, 224 (5221), 796-798.

- ³⁸. Gulick, A. Phosphorus as a factor in the origin of life. *Amer. Sci.* **1955**, 43 (3), 479-489.
- ³⁹. Schwartz, A. W. Phosphorus in prebiotic chemistry. *Phil. Trans. R. Soc. B-Biol. Sci.* **2006**, 361 (1474), 1743-1749.
- ⁴⁰. Pereto, J.; Bada, L. J.; Lazcano A. Charles darwin and the origin of life. *Orig. Life Evol. Biosph.* **2009**, 39 (5), 396 – 406.
- ⁴¹. Fuchs, H. L. *Meteorite Research Astrophysics and Space Science Library* **1969**, 683–695.
- ⁴². Koga, T.; Naraoka, H. A new family of extraterrestrial amino acids in the Murchison meteorite. *Sci. Rep.* **2017**, 7 (1), 636-8.
- ⁴³. Schmitt-Kopplin, P.; Gabelica, Z.; Gougeon, D. R.; Fekete, A.; Kanawati, B.; Harir, M.; Gebefuegi, I.; Eckel, G.; Hertkorn, N. High molecular diversity of extraterrestrial organic matter in Murchison meteorite revealed 40 years after its fall. *PNAS* **2009**, 107(7), 2763–2768.
- ⁴⁴. Hazen, R. M. Paleomineralogy of the Hadean Eon: A preliminary species list. *Am. J. Sci.* **2013**, 313 (9), 807–843.
- ⁴⁵. Cooper, G. W.; Onwo, W. M.; Cronin, J. R. Alkyl phosphonic acids and sulfonic acids in the Murchison meteorite. *Geochim. Cosmochim. Acta* **1992** 56 (11), 4109–4115.
- ⁴⁶. Blum, H. F. *Time's arrow and evolution*; Princeton University Press. **1951**.
- ⁴⁷. Lohrmann, R.; Orgel, E. L. Prebiotic synthesis: phosphorylation in aqueous solution. *Science.* **1968**, 161 (3836), 64-66.

- ⁴⁸. Leman, J. L.; Orgel, E. L.; Ghadiri, R. M. Amino acid dependent formation of phosphate anhydrides in water mediated by carbonyl sulfide. *J. Am. Chem. Soc.* **2006**, *128* (1), 20-21.
- ⁴⁹. Krishnamurthy, R.; Guntha, S.; Eschenmoser, A. Regioselective α -phosphorylation of aldoses in aqueous solution. *Angew. Chem. Int.* **2000**, *39* (13), 2281–2285.
- ⁵⁰. Hagan, W. J. Uracil-catalyzed synthesis of acetyl phosphate: a photochemical driver for protometabolism. *Chembiochem* **2010** *11* (3), 383–387
- ⁵¹. Sherwood, E.; Oro J. Cyanamide mediated syntheses under plausible primitive earth conditions II. The polymerization of deoxythymidine 50-triphosphate. *J. Mol. Evol.* **1977** *10* (3), 183–192.
- ⁵². Halmann, M.; Schmidt, H. L. Cyanogen-induced synthesis of ¹⁸O-labelled Bribofuranose-1-phosphate and its acid catalysed hydrolysis. *J. Chem. Soc. C* **1970** *9*, 1191–119.
- ⁵³. Yamagata Y.; Mohri T. Formation of cyanate and carbamyl phosphate by electric discharges of model primitive gas. *Orig Life Evol. Biosph.* **1982** *12* (1), 41–44.
- ⁵⁴. Weber, A. L. Formation of pyrophosphate, tripolyphosphate, and phosphorylimidazole with the thioester, N, S-diacetylcysteamine, as the condensing agent. *J. Mol. Evol.* **1981**, *18* (1), 24–29.
- ⁵⁵. Steinman, G.; Lemmon, R. M.; Calvin, M. Cyanamide: a possible key compound in chemical evolution. *PNAS* **1964** *52* (1), 27–30.
- ⁵⁶. Keefe, D.A.; Miller, L. S. Are polyphosphates or phosphate esters prebiotic reagents? *J. Mol. Evol.* **1995**, *41* (6), 693-702.

- ⁵⁷. Beck, A.; Orgel, L.E. The formation of condensed phosphate in aqueous solution. *PNAS* **1965**, *54* (3), 664-667.
- ⁵⁸. Brown, M. R.; Kornberg, A.; Joyce, G. Inorganic polyphosphate in the origin and survival of species. *PNAS* **2004**, *101* (46), 16085-16087.
- ⁵⁹. Fernandez-Garcia, C.; Coggins, A. J.; Powner, M. W. A Chemist's Perspective on the Role of Phosphorus at the Origins of Life. *Life* **2017**, *7* (3), 31.
- ⁶⁰. Rabinowitz, J.; Chang, S.; Ponnampereuma, C. Phosphorylation on the primitive earth: Phosphorylation by way of inorganic phosphate as a potential prebiotic process. *Nature* **1968**, *218*, 442-443.
- ⁶¹. Hermes-Lima, M. Model for prebiotic pyrophosphate formation: Condensation of precipitated orthophosphate at low temperature in the absence of condensing or phosphorylating agents. *J. Mol. Evol.* **1990**, *31* (5), 353-358.
- ⁶². Schwartz, A. W.; Ponnampereuma, C. Phosphorylation on the primitive earth: Phosphorylation of adenosine with linear polyphosphate salts in aqueous solution. *Nature* **1968**, *218* (5140), 443.
- ⁶³. Saffhill, R. Selective phosphorylation of the cis-2',3'-diol of unprotected ribonucleosides with trimetaphosphate in aqueous solution. *J. Org. Chem.* **1970** *35* (9), 2881-2883.
- ⁶⁴. Lohrmann R. Formation of nucleoside-5'-phosphoramidates under potentially prebiological conditions. *J. Mol. Evol.* **1977**, *10* (2), 137-154.
- ⁶⁵. Kolb, V.; Zhang, S. B.; Xu, Y.; Arrhenius, G. Mineral-induced phosphorylation of glycolate ion—a metaphor in chemical evolution. *Orig. Life Evol. Biosph.* **1997**, *27* (56), 485-503.

- ⁶⁶. Krishnamurthy, R.; Arrhenius, G.; Eschenmoser, A. Formation of glycolaldehyde phosphate from glycolaldehyde in aqueous solution. *Orig. Life Evol. Biosph.* **1999**, *29* (4), 333–354.
- ⁶⁷. Gao, K.; Orgel, L. E. Polyphosphorylation and non-enzymatic template-directed ligation of oligonucleotides. *Orig. Life Evol. Biosph.* **2000**, *30* (1), 45–51.
- ⁶⁸. Changmei, C.; Chang, F.; Rong, W.; Chunyuan, T.; Zhiwei, M.; Jing, C.; Yufen, Z. Phosphorylation of Adenosine with Trimetaphosphate Under Simulated Prebiotic Conditions. *Orig. Life Evol. Biosph.* **2002** *32* (3), 219–224.
- ⁶⁹. Mullen, L. B.; Sutherland, J. D. Formation of potentially prebiotic amphiphiles by reaction of b-hydroxy-n-alkylamines with cyclotriphosphate. *Angew. Chem. Int.* **2007**, *46* (22), 4166–4168.
- ⁷⁰. Turian, G.; Rivara-Minten, E. Prebiotic phosphoramidation of nucleobases by Mg²⁺-triggered decyclization of trimetaphosphate. *Arch des Sciences* **2001**, *54* (3), 233–238.
- ⁷¹. Kolb, V.; Zhang, S.; Xu, Y.; Arrhenius, G. Mineral induced phosphorylation of glycolate ion-A metaphor in chemical evolution. *Orig. Life Evol. Biosph.* **1997**, *27*, 485–503.
- ⁷². Karki, M.; Gibard, C.; Bhowmik, S.; Krishnamurthy, R. Nitrogenous derivatives of phosphorus and the origins of life: plausible prebiotic phosphorylating agents in water. *Life* **2017**, *7* (3), 32.
- ⁷³. Keefe, D.A.; Miller, L.S. Are polyphosphates or phosphate esters prebiotic reagents? *J. Mol. Evol.* **1995**, *41* (6), 693-702.
- ⁷⁴. Lazcano, A.; Miller, L.S. The origin and early evolution of life: prebiotic chemistry, the pre-RNA world, and time. *Cell* **1996**, *85* (6), 793-798.

- ⁷⁵. Yamagata, Y.; Watanabe, H.; Saitoh, M.; Namba, T. Volcanic production of polyphosphates and its relevance to prebiotic evolution. *Nature* **1991**, *352* (6335), 516-519.
- ⁷⁶. Bizzarri, B. M.; Šponer, J. E.; Šponer, J.; Cassone, G.; Kapralov, M.; Timoshenko, G. N.; Krasavin, E.; Fanelli, G.; Timperio, A. M.; Mauro, E. D.; Saladino, R. Meteorite-Assisted Phosphorylation of Adenosine Under Proton Irradiation Conditions. *ChemSystemsChem* **2019**, *1*, e190003 1–11.
- ⁷⁷. Konigsberger, E.; Konigsberger, L. *Biom mineralization: Medical Aspects of Solubility* **2006**.
- ⁷⁸. Herschy, B.; Chang, J. S.; Blake, R.; Lepland, A.; Abbott-Lyon, H.; Sampson, J.; Atlas, Z.; Kee, T. P.; Pasek, M. A. Archean phosphorus liberation induced by iron redox geochemistry. *Nat. Commun.* **2018**, *9* (1).
- ⁷⁹. Miller, S. L.; Lazcano, A. The origin of life-did it occur at high temperatures? *J. Mol. Evol.* **1995**, *41* (6), 689-692.
- ⁸⁰. Bada, J. L.; Lazcano, A. Some like it hot, but not the first biomolecules. *Science* **2002**, *296* (5575), 1982-1983.
- ⁸¹. Steinman, G.; Kenyon, D. H.; Calvin, M. Dehydration condensation in aqueous solution. *Nature* **1965**, *206* (4985), 707-708.
- ⁸². Ponnampertuma, C.; Mack, R. Nucleotide synthesis under possible primitive earth conditions. *Science* **1965**, *148* (3674), 1221-1223.
- ⁸³. Gull, M. Prebiotic Phosphorylation Reactions on the Early Earth. *Challenges* **2014**, *5* (2), 193-212.

- ⁸⁴. Pasek, M. A.; Harnmeijer, J. P.; Buick, R.; Gull, M.; Atlas, Z. Evidence for reactive reduced phosphorus species in the early Archaean ocean. *PNAS* **2013**, *110* (25), 10089-10094.
- ⁸⁵. Gull, M.; Mojica, M. A.; Fernández, F. M.; Gaul, D. A.; Orlando, T. M.; Liotta, C. L.; Pasek, M. A. Nucleoside Phosphorylation by the Mineral Schreibersite. *Scientific Reports* **2015**, *5* (1).
- ⁸⁶. Saladino, R.; Crestini, C.; Pino, S.; Costanzo, G.; Mauro, E. D. Formamide and the origin of life. *Phys. Life Rev.* **2012**, *9* (1), 84-104.
- ⁸⁷. Hubbard, J. S.; Voecks, G. E.; Hobby, G. L.; Ferris, J. P.; Williams, E. A. Nicodem D. E. Ultraviolet gas phase and ultraviolet-photocatalytic synthesis from CO and NH₃. *J. Mol. Evol.* **1975**, *5* (3), 223-241.
- ⁸⁸. Marsh, J. D. F.; Martin, M. J. The hydrolysis and polymerization of hydrogen cyanide in alkaline solutions. *J. Appl. Chem.* **1957**, *7* (4), 205-209.
- ⁸⁹. Sanchez, R. A.; Ferris, J. P.; Orgel, L. E. Studies in prebiotic synthesis. II. Synthesis of purine precursors and amino acids from aqueous hydrogen cyanide. *J. Mol. Biol.* **1967**, *30* (2), 223-253.
- ⁹⁰. Schoffstall, M.A. Prebiotic phosphorylation of nucleosides in formamide. *Orig. Life Evol. Biosph.* **1976**, *7* (4), 399-412.
- ⁹¹. Costanzo, G.; Saladino, R.; Crestini, C.; Ciciriello, F.; Mauro, E. D. Nucleoside phosphorylation by phosphate minerals. *J. Biol. Chem.* **2007**, *282* (23), 16729-16735.
- ⁹². Schoffstall, A. M.; Barto, R. J.; Ramos, D. L. Nucleoside and deoxynucleoside phosphorylation in formamide solutions. *Orig. Life Evol. Biosph.* **1982**, *12* (2), 143-151.

- ⁹³. Gull, M.; Cafferty, J. B.; Hud, V.N.; Pasek, A.M. Silicate-promoted phosphorylation of glycerol in non-aqueous solvents: a prebiotically plausible route to organophosphates. *Life* **2017** *7* (3), 29.
- ⁹⁴. Schoffstall, A. M.; Laing, E. M. Phosphorylation mechanisms in chemical evolution. *Orig. Life Evol. Biosph.* **1985**, *15* (2), 141-150.
- ⁹⁵. Gull, M.; Zhou, M.; Fernández, F.M.; Pasek, M.A. Prebiotic phosphate ester syntheses in a deep eutectic solvent. *J. Mol. Evol.* **2014**, *78* (2), 109–117.
- ⁹⁶. Lohrmann, R. Formation of urea and guanidine by irradiation of ammonium cyanide. *J. Mol. Evol.* **1972**, *1* (3), 263-269.
- ⁹⁷. Bada, J. L.; Chalmers, J. H.; Cleaves, H. J. Is formamide a geochemically plausible prebiotic solvent? *Phys. Chem. Chem. Phys.* **2016**, *18* (30), 20085-20090.
- ⁹⁸. Pasek M. A.; Block, K. Lightning-induced reduction of phosphorus oxidation state. *Nat. Geosci.* **2009**, *2* (8), 553–556.
- ⁹⁹. Pasek, M. A.; Lauretta, D. S. Extraterrestrial flux of potentially prebiotic C, N, and P to the Early Earth. *Orig. Life Evol. Biosph* **2008**, *38* (1), 5-21.
- ¹⁰⁰. Bryant, D. E.; Kee T. P. Direct evidence for the availability of reactive, water soluble phosphorus on the early earth. H-phosphinic acid from the Nantan meteorite. *Chem. Commun.* **2006**, *22*, 2344–2346
- ¹⁰¹. La Cruz, N. L.; Qasim, D.; Abbott-Lyon, H.; Pirim, C.; McKee, A. D.; Orlando, T.; Gull, M.; Lindsay, D.; Pasek, M. A. The evolution of the surface of the mineral schreibersite in prebiotic chemistry. *Phys. Chem. Chem. Phys.* **2016**, *18* (2), 20160-20167.
- ¹⁰². Pirim, C.; Pasek, M. A.; Sokolov, D. A.; Sidorov, A. N.; Gann, R. D.; Orlando, T. M. Investigation of schreibersite and intrinsic oxidation products from Sikhote-Alin, Seymchan,

and Odessa meteorites and Fe₃P and Fe₂NiP synthetic surrogates. *Geochim. Cosmochim. Acta* **2014**, *140*, 259–274.

¹⁰³ Bryant, D. E.; Greenfield, D.; Walshaw, R. D.; Johnson, B. R. G.; Herschy, B.; Smith, C.; Pasek, M. A.; Telford, R.; Scowen, I.; Munshi, T.; Edwards, H. G. M.; Cousins, C. R.; Crawford, I. A.; Kee, T. P. Hydrothermal modification of the Sikhote-Alin iron meteorite under low pH geothermal environments. A plausibly prebiotic route to activated phosphorus on the early Earth. *Geochim Cosmochim Acta* **2013**, *109*, 90–112.

¹⁰⁴ Pasek, M. A.; Lauretta, D. S. Aqueous Corrosion of Phosphide Minerals from Iron Meteorites: A Highly Reactive Source of Prebiotic Phosphorus on the Surface of the Early Earth. *Astrobiology* **2005**, *5* (4), 515–535.

¹⁰⁵ C. Pedersen, A. K. Armalcolite-Bearing Fe-Ti Oxide Assemblages in Graphite-Equilibrated Salic Volcanic Rocks with Native Iron from Disko, Central West Greenland. *Contributions to Mineralogy and Petrology* **1981**, *77* (4), 307–324.

¹⁰⁶ Britvin, S. N.; Murashko, M. N.; Vapnik, Y.; Polekhovsky, Y. S.; Krivovichev, S. V. Earth's Phosphides in Levant and insights into the source of Archean prebiotic phosphorus. *Sci. Rep.* **2015**, *5* (1), 8355.

¹⁰⁷ Pasek, M, A.; Dworkin, J. P.; Lauretta, D.S. A radical pathway for organic phosphorylation during schreibersite corrosion with implications for the origin of life. *Geochimica et Cosmochimica Acta* **2007**, *71* (7), 1721-1736.

¹⁰⁸ Pasek, M. A.; Kee, T. P.; Bryant, D. E.; Pavlov, A. A; Lunine J. L. Production of potentially prebiotic condensed phosphates by phosphorus redox chemistry. *Angew. Chem. Int.* **2008**, *47* (41), 7918-7920.

- ¹⁰⁹. Qasim, D.; Vlasak, L.; Pital, A.; Beckman, T.; Mutanda, N.; Abbott-Lyon, H. Adsorption of Water, Methanol, and Formic Acid on Fe₂NiP, a Meteoritic Mineral Analogue. *J. Phys. Chem. C* **2017**, *121* (25), 13645-13654.
- ¹¹⁰. Walling C. Fenton's reagent revisited. *Acc. Chem. Res.* **1975**, *8* (4), 125–131.
- ¹¹¹. Bryant, D. E.; Marriott, K. E. R.; MacGregor, S. A.; Fishwick, C. W. G.; Pasek, M. A.; Kee, T. P. On the prebiotic potential of reduced oxidation state phosphorus: the H-phosphinate–pyruvate system. *Chem. Commun.* **2010**, *46* (21), 3726–3728.
- ¹¹². Slavicinska, K.; Khweis, S.; Aldihri, F. Pasek, M. and Abbott-Lyon, H.L.; “Reactivity of Metal Phosphites”, *Chemistry: A European Journal*, manuscript in preparation, 2020.
- ¹¹³. McCash, M. Elaine. *Surface Chemistry*; Oxford: New York, 2001.
- ¹¹⁴. Libretexts. 18.11: Heterogeneous Catalysis.
[https://chem.libretexts.org/Bookshelves/General_Chemistry/Book:_ChemPRIME_\(Moor_e_et_al.\)/18Chemical_Kinetics/18.11:_Heterogeneous_Catalysis](https://chem.libretexts.org/Bookshelves/General_Chemistry/Book:_ChemPRIME_(Moor_e_et_al.)/18Chemical_Kinetics/18.11:_Heterogeneous_Catalysis) (accessed Sep 24, 2019).
- ¹¹⁵. Usman, M. A.; Alaje, T. O.; Ekwueme, V. I.; Awe, E. A. Investigation of the Catalytic Performance of a Novel Nickel/Kit-6 Nanocatalyst for the Hydrogenation of Vegetable Oil. *ISRN Chemical Engineering* **2012**, *2012*, 1–6.
- ¹¹⁶. Pushkarev, V. V.; Kovalchuk, V. I.; d'Itri J. L. Probing Defect Sites on the CeO₂ Surface with Dioxygen. *J. Phys. Chem. B* **2004** *108* (17), 5341-5348.
- ¹¹⁷. Gellings, P. J.; Bouwmeester, H. J. M. Solid state aspects of oxidation catalysis. *Catal. Today* **2000**, *58* (1), 1.

- ¹¹⁸. Ortiz-Medina, J.; Wang, Z.; Cruz-Silva, R.; Morelos-Gomez, A.; Wang, F.; Yao, X.; Terrones, M.; Endo, M. Defect Engineering and Surface Functionalization of Nanocarbons for Metal-Free Catalysis. *Adv. Mater.* **2019** *31* (13), 1805717, 1-16.
- ¹¹⁹. Farias, M. J. S.; Feliu, J. M. Determination of Specific Electrocatalytic Sites in the Oxidation of Small Molecules on Crystalline Metal Surfaces. *Topics in current chemistry* **2019** *377* (1), 5, 1-25.
- ¹²⁰. Butt, H-J.; Graf, K.; Kappl, M. *Physics and Chemistry of Interfaces*; Wiley-VCH: Germany, 2013.
- ¹²¹. Nix, R. *Surface Science*.
[https://chem.libretexts.org/Bookshelves/Physical_and_Theoretical_Chemistry_Textbook_Maps/Book:_Surface_Science_\(Nix\)/1:_Structure_of_Solid_Surfaces](https://chem.libretexts.org/Bookshelves/Physical_and_Theoretical_Chemistry_Textbook_Maps/Book:_Surface_Science_(Nix)/1:_Structure_of_Solid_Surfaces). (accessed Sep 24, 2019).
- ¹²². Brady, P. V. *The Physics and Chemistry of Mineral Surfaces*; CRC Press: New Mexico, 1996.
- ¹²³. Hazen, R. M. Chiral Crystal Faces of Common Rock-Forming Minerals. *Progress in Biological Chirality* **2004**, 137–151.
- ¹²⁴. Appel, C.; Ma, L. Q.; Rhue, R. D.; Kennelley, E. Point of Zero Charge Determination in Soils and Minerals via Traditional Methods and Detection of Electroacoustic Mobility. *Geoderma* **2003**, *113* (1-2), 77–93.
- ¹²⁵. Bernal, J. D. The physical basis of life. *Proc. Phys. Soc. A* **1949** *62* (9), 537–558.
- ¹²⁶. Hazen, R. M.; Sverjensky, D. A. Mineral Surfaces, Geochemical Complexities, and the Origins of Life. *Cold Spring Harb Perspect Biol.* **2010** *2* (5), 1-21.

- ¹²⁷. Shock, E. L. Hydrothermal dehydration of aqueous organic compounds. *Geochim Cosmochim Acta* **1993** 57 (14), 3341–3349.
- ¹²⁸. Huang, W.; Ferris, J. P. One-Step, Regioselective Synthesis of up to 50-mers of RNA Oligomers by Montmorillonite. *Catalysis. J. Am. Chem. Soc.* **2006** 128 (27), 8914-8919.
- ¹²⁹. Pitsch, S.; Eschenmoser, A.; Gedulin, B; Hui, S.; Arrhenius, G. Mineral induced formation of sugar phosphates. *Orig. Life Evol. Biosph.* **1995** 25 (4), 297-334.
- ¹³⁰. Lahav, N.; White D; Chang, S. Peptide formation in the prebiotic era: Thermal condensation of glycine in fluctuating clay environments. *Science* **1978** 201 (4350), 67–69.
- ¹³¹. Marshall-Bowman, K.; Ohara, S.; Sverjensky, D. A.; Hazen, R. M.; Cleaves, J. H. Catalytic peptide hydrolysis by mineral surface: Implications for prebiotic chemistry. *Geochimica et Cosmochimica Acta.* **2010** 74 (20), 5852-5861.
- ¹³². Jonsson, C. M.; Jonsson, L. C.; Sverjensky, D. A.; Cleaves, H. J.; Hazen, R. M. Attachment of L-Glutamate to Rutile (alpha-TiO₂): A Potentiometric, Adsorption, and Surface Complexation Study. *Langmuir* **2009** 25 (20), 12127–12135.
- ¹³³. Erastova, V.; Degiacomi, M. T.; Fraser, D. G.; H. Chris Greenwell, H. C. Mineral surface chemistry control for origin of prebiotic peptides. *Nat. Commun.* **2017** 8 (1), 2033, 1-9.
- ¹³⁴. Biondi, E.; Branciamore, S.; Maurel, M.-C.; Gallori, E. Montmorillonite protection of an UV-irradiated hairpin ribozyme: evolution of the RNA world in a mineral environment. *BMC Evol. Biol.* **2007** 7, S2.
- ¹³⁵. Ertl, G.; Küppers, J. *Low Energy Electrons and Surface Chemistry*; Verlag Chemie: Weinheim, 1989.

- ¹³⁶. Woodruff, D. P.; Delchar, T. A. *Modern Techniques in Surface Science*; Cambridge Solid State Science Series; Cambridge University Press: Cambridge, 1986.
- ¹³⁷. Freund, H. J.; Dillmann, B.; Ehrlich, D.; Haßel, M.; Jaeger, R. M.; Kühlenbeck, H.; Ventrice, C. A.; Winkelmann, F.; Wohlrab, S.; Xu, C.; Bertrams, T.; Brodde, A.; Neddermeyer, H. Adsorption and Reaction of Molecules on Surfaces of Metal-metal Oxide Systems. *J. Mol. Catal.* **1993**, 82 (2-3), 143-169.
- ¹³⁸. Kühlenbeck, H.; Shaikhutdinov, S.; Freund, H.-J. Well-Ordered Transition Metal Oxide Layers in Model Catalysis-A series of Case Studies. *Chem. Rev.* **2013**, 113 (6), 3986- 4034.
- ¹³⁹. Gshalaev, V. S.; Demirchan, A. C. *Hydroxyapatite synthesis, properties, and applications*; Nova Science Publishers: New York, 2012; p 92.
- ¹⁴⁰. Thanh, D. T. M.; Nam, P. T.; Phuong, N. T.; Que, L. X.; Anh, N. V.; Hoang T.; Lam, T. D. Controlling the electrodeposition, morphology, and structure of hydroxyapatite coating on 316L stainless steel.” *Mater. Sci.Eng.* **2013**, C 33, 2037-2045.
- ¹⁴¹. Mallik, A.; Ray, B. C. Evolution of Principle and Practice of Electrodeposited Thin Film: A Review on Effect of Temperature and Sonication. *International Journal of Electrochemistry*, **2011**, 1–16.
- ¹⁴². Kakooei, S.; Ismail, M. C.; Wahjoedi, B. A. Electrochemical Study of Iridium Oxide Coating on Stainless Steel Substrate. *International Journal of Electrochemical Science.* **2013**, 8(3), 3290 – 3301.
- ¹⁴³. Fornell, J.; Feng, Y. P.; Pellicer, E.; Surinach, S.; Baro, M.D.; Sort, J. Mechanical behaviour of brushite and hydroxyapatite coatings electrodeposited on newly developed FeMnSiPd alloys. *J. Alloys Compd.* **2017**, 729, 231-239.

- ¹⁴⁴. Jamesh, M.; Kumar, S.; Narayanan, T. S. N. S. Electrodeposition of Hydroxyapatite Coating on Magnesium for Biomedical Applications. *Journal of Coatings Technology and Research* **2011**, 9 (4), 495–502.
- ¹⁴⁵. Mallik, A.; Ray, B. C. Evolution of Principle and Practice of Electrodeposited Thin Film: A Review on Effect of Temperature and Sonication. *International Journal of Electrochemistry* **2011**, 1–16.
- ¹⁴⁶. Pasa, A. A.; Munford, M. L. In *Encyclopedia of Chemical Processing*; Taylor & Francis Group: New York, NY, 2006; Vol. 3, pp 821–832.
- ¹⁴⁷. Pletcher, D. *A First Course in Electrode Processes*, 2nd ed.; RSC Publishing: Cambridge, UK, 2009; pp 137-143.
- ¹⁴⁸. Survila, A. *Electrochemistry of Metal Complexes: Applications from Electroplating to Oxide Layer Formation*; Wiley-VCH Verlag GmbH & Co. KGaA: Weinheim, Germany, 2015.
- ¹⁴⁹. Meier, D. M.; Urakawa, A.; Mäder, R.; Baiker, A. Design and Performance of a Flow-through Polarization-Modulation Infrared Reflection-Absorption Spectroscopy Cell for Time-Resolved Simultaneous Surface and Liquid Phase Detection under Concentration and Temperature Perturbations. *Review of Scientific Instruments* **2009**, 80 (9), 094101.
- ¹⁵⁰. Yates, J. T. *Vibrational spectroscopy of molecules on surfaces*; Plenum Pr.: New York u.a., 1987.
- ¹⁵¹. Monyoncho, E. A.; Zamlynyy, V.; Woo, T. K.; Baranova, E. A. The Utility of Polarization Modulation Infrared Reflection Absorption Spectroscopy (PM-IRRAS) in Surface and in Situ Studies: New Data Processing and Presentation Approach. *The Analyst* **2018**, 143 (11), 2563–2573.

- ¹⁵². Greenler, R. G. Reflection Method for Obtaining the Infrared Spectrum of a Thin Layer on a Metal Surface. *The Journal of Chemical Physics* **1969**, *50* (5), 1963–1968.
- ¹⁵³. Faguy, P. W.; Richmond, W. N. Real-Time Polarization Modulation Infrared Spectroscopy Applied to the Study of Water and Hydroxide Ions at Electrode Surfaces. *Journal of Electroanalytical Chemistry* **1996**, *410* (1), 109–113.
- ¹⁵⁴. Rowe, D. J., Smith, D., & Wilkinson, J. S. (2017). Complex refractive index spectra of whole blood and aqueous solutions of anticoagulants, analgesics and buffers in the mid-infrared. *Scientific Reports*.
- ¹⁵⁵. Downing, H. D. & Williams, D. (1975). Optical Constants of Water in the Infrared. *Journal of Geophysical Research*, *80*(12).
- ¹⁵⁶. Lucarini, V., Saarinen, J. J., Peiponen, K.-E. & Vartiainen, E. M. *Kramers-Kronig Relations in Optical Materials Research*; Springer: Berlin, Germany, 2005.
- ¹⁵⁷. Kubota, J.; Ma, Z.; Zaera, F. In Situ Characterization of Adsorbates in Solid–Liquid Interfaces by Reflection–Absorption Infrared Spectroscopy. *Langmuir* **2003**, *19* (8), 3371–3376.
- ¹⁵⁸. Bunaciu, A. A.; Udriștioiu, E. g.; Aboul-Enein, H. Y. X-Ray Diffraction: Instrumentation and Applications. *Critical Reviews in Analytical Chemistry* **2015**, *45* (4), 289-299.
- ¹⁵⁹. Robinson, J. W. *Undergraduate instrumental analysis*; M Dekker: New York, 1995
- ¹⁶⁰. Libretexts. X-ray diffraction (XRD) basics and application.
[https://chem.libretexts.org/Courses/Franklin_and_Marshall_College/Introduction_to_Materials_Characterization_-_CHM_412_Collaborative_Text/Diffraction_Techniques/X-ray_diffraction_\(XRD\)_basics_and_application](https://chem.libretexts.org/Courses/Franklin_and_Marshall_College/Introduction_to_Materials_Characterization_-_CHM_412_Collaborative_Text/Diffraction_Techniques/X-ray_diffraction_(XRD)_basics_and_application) (accessed Dec 18, 2019).

- ¹⁶¹. Khursheed, A. *Scanning electron microscope optics and spectrometers*; World Scientific: Singapore, 2011.
- ¹⁶². Luo, Z. *A practical guide to transmission electron microscopy fundamentals*, 1st ed.; Momentum Press: New York, NY, 2016.
- ¹⁶³. Balci, M. *Basic ¹H- and ¹³C-NMR spectroscopy*; Elsevier: Amsterdam, 2005.
- ¹⁶⁴. Pasek, M. *Phosphorus NMR of Natural Samples*; Free Radical Consulting: Seffner, FL, 2018.
- ¹⁶⁵. Johnsson, M. S.-A.; Nancollas, G. H. The Role of Brushite and Octacalcium Phosphate in Apatite Formation. *Critical Reviews in Oral Biology & Medicine* **1992**, *3* (1), 61–82.
- ¹⁶⁶. V.; Ng, C.; Wilke, M.; Tiersch, B.; Fratzl, P.; Peter, M. Size-Controlled Hydroxyapatite Nanoparticles as Self-Organized Organic/Inorganic Composite Materials. *Biomaterials* **2005**, *26* (26), 5414–5426.
- ¹⁶⁷. Yang, Y.; Han, J.; Ning, X.; Cao, W.; Xu, W.; Guo, L. Controllable Morphology and Conductivity of Electrodeposited Cu₂O Thin Film: Effect of Surfactants. *ACS Applied Materials & Interfaces* **2014**, *6* (24), 22534–22543.
- ¹⁶⁸. Kauffman, G. B. Eduard Schweizer (1818-1860): The Unknown Chemist and His Well-Known Reagent. *Journal of Chemical Education* **1984**, *61* (12), 1095.
- ¹⁶⁹. Accuracy, Precision and Detection Limits.
<https://myscope.training/legacy/analysis/eds/accuracy/> (accessed Feb 16, 2020).
- ¹⁷⁰. Wang, X.; Zhang, L.; Liu, Z.; Zeng, Q.; Jiang, G.; Yang, M. Probing the Surface Structure of Hydroxyapatite through Its Interaction with Hydroxyl: a First-Principles Study. *RSC Advances* **2018**, *8* (7), 3716–3722.

¹⁷¹Dabo, I.; Wieckowski, A.; Marzari, N. Vibrational Recognition of Adsorption Sites for CO on Platinum and Platinum–Ruthenium Surfaces. *Journal of the American Chemical Society* **2007**, *129* (36), 11045–11052.

¹⁷²Lansford, J. L.; Vlachos, D. G. Infrared Spectroscopy Data- and Physics-Driven Machine Learning for Characterizing Surface Microstructure of Complex Materials. *Nature Communications* **2020**, *11* (1).

¹⁷³Zu, L.; Gao, X.; Lian, H.; Cai, X.; Li, C.; Zhong, Y.; Hao, Y.; Zhang, Y.; Gong, Z.; Liu, Y.; Wang, X.; Cui, X. High Electrochemical Performance Phosphorus-Oxide Modified Graphene Electrode for Redox Supercapacitors Prepared by One-Step Electrochemical Exfoliation. *Nanomaterials* **2018**, *8* (6), 417.

¹⁷⁴Hampton, C.; Demoin, D.; Glaser, R.E. *Vibrational spectroscopy tutorial: sulfur and phosphorus Org Spectrosc* (2010)
https://faculty.missouri.edu/~glaserr/8160f10/A03_Silver.pdf (accessed April 4, 2020)

¹⁷⁵Seesanong, S.; Laosinwattana, C.; Boonchom, B. A simple rapid route to synthesize monocalcium phosphate monohydrate using calcium carbonate with different phases derived from green mussel shells. *J. Mater. Environ. Sci.* **2019**, *10* (2) 113-118.

¹⁷⁶Li, X.; Stotesbury, S. J.; Jayasooriya, U. A. Infrared-spectra of Urea Isolated in a Solid Argon Matrix. *Spectrochimica Acta Part A: Molecular Spectroscopy* **1987**, *43* (12), 1595–1597.

¹⁷⁷King, S. Low Temperature Matrix Isolation Study of Hydrogen-Bonded, High-Boiling Organic Compounds—III: Infrared-spectra of Monomeric Acetamide, Urea and Urea-d₄. *Spectrochimica Acta Part A: Molecular Spectroscopy* **1972**, *28* (1), 165–175.

- ¹⁷⁸. Uno, T.; Machida, K.; Saito, Y. Out-of-Plane Vibrations of Acetamide and Partially N-Deuterated Acetamide. *Spectrochimica Acta Part A: Molecular Spectroscopy* **1971**, 27 (6), 833–844.
- ¹⁷⁹. Hadži, D.; Kidrič, J.; Kneževic, Ž.; Barlič, B. The Normal Coordinate Analysis of Urea, Thiourea, and Their Isotopic Analogues in the Solid Phase and in Solution. *Spectrochimica Acta Part A: Molecular Spectroscopy* **1976**, 32 (4), 693–704.
- ¹⁸⁰. Teo, L.-S.; Chen, C.-Y.; Kuo, J.-F. Fourier Transform Infrared Spectroscopy Study on Effects of Temperature on Hydrogen Bonding in Amine-Containing Polyurethanes and Poly(Urethane–Urea)s. *Macromolecules* **1997**, 30 (6), 1793–1799.
- ¹⁸¹. Manivannan, M.; RAJENDRAN, S. Investigation of inhibitive action of urea-Zn²⁺ system in the corrosion control of carbon steel in sea water. *International Journal of Engineering Science and Technology* 2011, 3 (11), 8048-8060.
- ¹⁸². Vijay, A.; Sathyanarayana, D. Ab Initio Study of the Force Field, Geometry and Vibrational Assignment of Urea. *Journal of Molecular Structure* **1993**, 295, 245–258.
- ¹⁸³. Wypych, F. *Clay surfaces: fundamentals and applications*; Academic: Oxford, 2004.
- ¹⁸⁴. Moreno, M. A.; Gálvez O.; Maté B.; Herrero, V. J.; Escribano, R. Formate Ion: Structure and Spectroscopic Properties. *The Journal of Physical Chemistry A* **2011**, 115 (1), 70–75.
- ¹⁸⁵. Donaldson, J.; Knifton, J.; Ross, S. The Fundamental Vibrational Spectra of the Formates of the Main Group Elements. *Spectrochimica Acta* **1964**, 20 (5), 847–851.

- ¹⁸⁶. Ito, K.; Bernstein, H. J. The Vibrational Spectra Of The Formate, Acetate, And Oxalate Ions. *Canadian Journal of Chemistry* **1956**, *34* (2), 170–178.
- ¹⁸⁷. Carpenter, W. B.; Fournier, J. A.; Biswas, R.; Voth, G. A.; Tokmakoff, A. Delocalization and Stretch-Bend Mixing of the HOH Bend in Liquid Water. *The Journal of Chemical Physics* **2017**, *147* (8), 084503.
- ¹⁸⁸. Mohamed, M. M.; Ichikawa, M. Spectroscopic and Kinetic Studies of the Reaction of CO+H₂O and CO+O₂ and Decomposition of HCOOH on Au/H-Mordenite Catalysts. *Journal of Colloid and Interface Science* **2000**, *232* (2), 381–388.
- ¹⁸⁹. Park, J. Y.; Woon, D. E. Theoretical Modeling of Formic Acid (HCOOH), Formate (HCOO⁻), and Ammonium Vibrational Spectra in Astrophysical Ices. *The Astrophysical Journal* **2006**, *648* (2), 1285–1290.
- ¹⁹⁰. Bertarione, S.; Scarano, D.; Zecchina, A.; Johánek, V.; Hoffmann, J.; Schauermann, S.; Libuda, J.; Rupprechter, G.; Freund, H-J. Surface Reactivity of Pd Nanoparticles Supported on Polycrystalline Substrates as Compared to Thin Film Model Catalysts: Infrared Study of CH₃OH Adsorption. *Journal of Catalysis* **2004**, *223* (1), 64–73.
- ¹⁹¹. Wang, X.; Qian, C.; Yu, X. Synthesis of Nano-Hydroxyapatite via Microbial Method and Its Characterization. *Applied Biochemistry and Biotechnology* **2014**, *173* (4), 1003–1010.
- ¹⁹². Periasamy, A.; Muruganand, S.; Palaniswamy, M. Vibrational studies of Na₂SO₄, K₂SO₄, NaHSO₄ and KHSO₄ crystals. *Rasayan J. Chem.* **2009**, *2* (4), 981-989.

- ¹⁹³. O. Mabrouk, K. B.; Kauffmann, T. H.; Aroui, H.; Fontana, M. D. Raman Study of Cation Effect on Sulfate Vibration Modes in Solid State and in Aqueous Solutions. *Journal of Raman Spectroscopy* **2013**, *44* (11), 1603–1608.
- ¹⁹⁴. Bandara, A.; Kubota, J.; Wada, A.; Domen, K.; Hirose, C. Adsorption and Reactions of Formic Acid on (2×2)-NiO(111)/Ni(111) Surface. 1. TPD and IRAS Studies under Ultrahigh Vacuum Conditions. *The Journal of Physical Chemistry* **1996**, *100* (36), 14962–14968.
- ¹⁹⁵. Ren, F.; Ding, Y.; Leng, Y. Infrared Spectroscopic Characterization of Carbonated Apatite: A Combined Experimental and Computational Study. *Journal of Biomedical Materials Research Part A* **2014**, *102* (2), 496–505.
- ¹⁹⁶. A Guide to Identifying Common Inorganic Fillers and Activators Using Vibrational Spectroscopy. <http://www.irdg.org/the-infrared-and-raman-discussion-group/ijvs/ijvs-volume-2-edition-3/a-guide-to-identifying-common-inorganic-fillers-and-activators-using-vibrational-spectroscopy/> (accessed Apr 4, 2020).

Appendix 1. Standard Operating Procedure for SEM

Tescan Vega 3: Scanning Electron Microscopy with Energy Dispersive X-Ray Spectroscopy

(SEM/EDX)

Written by Estefania Garcia

Edited by Matthew Rosenberg and Heather Abbott-Lyon

I. Getting Started

1. Reserve time online at <https://faces.ccrcc.uga.edu/>. Consult with your PI or instrumentation manager for help.
2. Sign the logbook include: date, time, user's name, PI's name (if different) and sample type.
3. Click the VegaTC icon  on the Windows Desktop (located on the **left monitor**).
4. The login screen will appear, requiring a username and password.
 - a. Username: Research
 - b. Password: Research

II. Adding/Removing Samples

1. The sample should be fixed with carbon or copper tape to the specimen stub (see Fig. 1) before it's placed in the sample chamber. Tweezers should be used to peel the tape and gloves should be worn to attach the sample. If you are unsure how to do this, consult with your PI or instrumentation manager.
2. Click on the “**Home**” button, which is located on the stage control panel, to ensure that the sample stage is lowered to 40 mm on the z-axis. The chamber camera should be off.



Fig. 1 Specimen stub (left) and carbon tape (right).

3. The microscope needs to be vented before placing a sample inside, click on the “Vent” button in the Vacuum panel (on the lower right side of the screen). Wait until the panel turns green, this indicates the pressure has increased to atmospheric level.



Fig. 2 Photo of the SEM chamber door when open.

4. Always wear gloves when handling samples and inserting them into the chamber.
5. Carefully open the chamber door by pulling it out slowly ensuring you do not hit anything. Fig. 2 shows the chamber door open.
6. There is a stage control panel on the desktop (illustrated below in Fig. 3); this has the automatic sample positions. The sample position can be selected by clicking on the corresponding number button on the carousel. The stage will then rotate to that position. For example, if you click on “2” (as shown below), the carousel will rotate to the “2”

position allowing you add or remove a sample from position “2.”

7. Once the stage has finished rotating, the screw on the sample stage must be loosened using an Allen wrench or screwdriver.

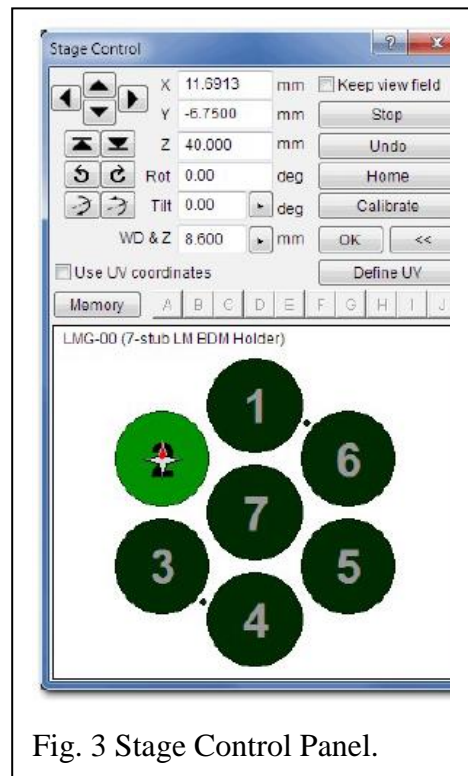


Fig. 3 Stage Control Panel.

8. Affix the sample to the specimen stub with carbon or copper tape. Place the specimen stub in the sample stage with suitable tweezers. Tighten the screw until there is a give or a pushback, indicating that the sample stub has made an electrical connection to the sample stage. Ensure that the sample does not touch the inside of any part of the chamber. If the sample does touch the chamber, then there will be an acoustic buzzer. If you hear the buzzer, consult with your PI or instrumentation manager for help.
9. Close the chamber door tightly.
10. Click on the “**Pump**” button in the Vacuum panel, it takes around 3 minutes for the microscope be vacuum ready (see Fig. 4). **NOTE:** Sometimes a vacuum error may occur during the “PUMP” procedures, if so then wipe down the door and O-ring with a Kimwipe,TM ensure the O-ring is inside the track, and then, repeat the pumping procedure.
11. To remove the sample, VENT the chamber via clicking the VENT button, and repeat Steps 5-7 as described above, except for Step 7 remove the sample.

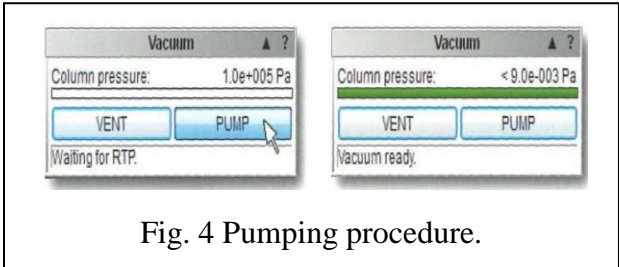


Fig. 4 Pumping procedure.

III. Analyzing Samples

A. Getting Started

1. Once the microscope is vacuum ready, click the “**HV**” button on the electron beam panel to turn on the high voltage (Fig. 5). Select the voltage appropriate for the sample. Samples with low conductivity work best with 10.00 kV; for all other samples 30.00 kV is recommended.

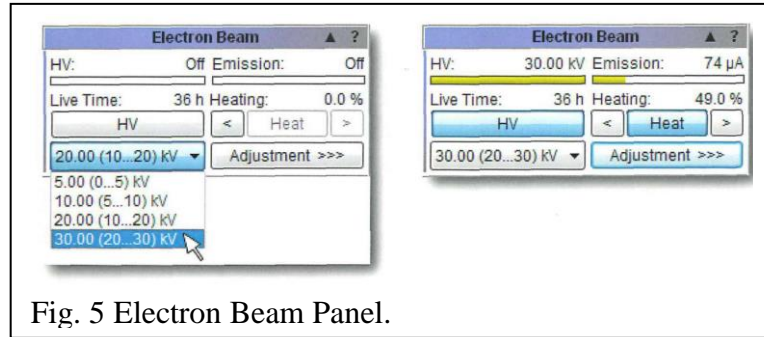


Fig. 5 Electron Beam Panel.

2. Select the sample to be analyzed by selecting its sample position in the Stage control panel (Fig. 6), click on the corresponding number on the carousel.

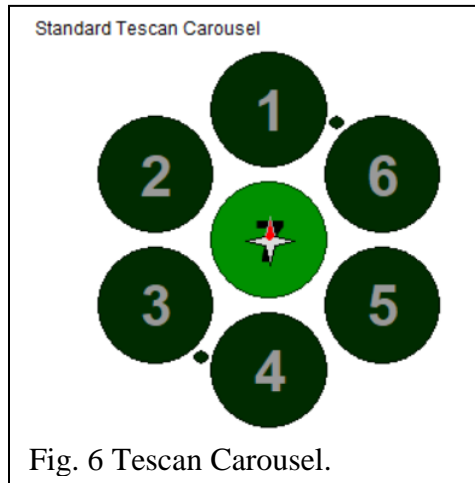


Fig. 6 Tescan Carousel.

3. Make sure that the chamber view is visible, by clicking on this icon  located on the Main Toolbar menu.

4. To achieve optimum resolution, shorten the working distance by moving the stage closer to the microscope, adjusting the Z axis, located on the stage control panel

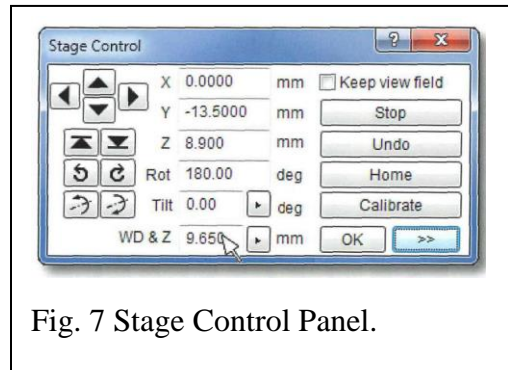


Fig. 7 Stage Control Panel.

(Fig. 7). This number cannot be less than 10 mm or the stage may hit the microscope.

5. To move the image, place the cursor over the SEM and use the trackball (Fig. 8) to adjust the location of the image, alternatively use the left, right, up and down arrows located on the stage control panel.

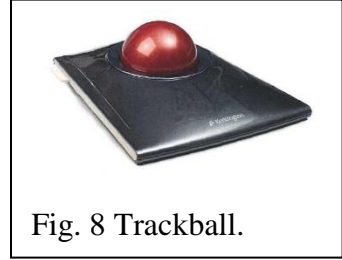


Fig. 8 Trackball.

6. The brightness and contrast can be adjusted by selecting the auto signal function, by clicking on this



icon located on the toolbar. To manually adjust the brightness and contrast, use the icon  and the Trackball.

7. Magnify the image by clicking this icon  on the toolbar, and adjust with the Trackball by turning it left and right.

8. Now that the image has been focused and magnified, adjust the speed by clicking on the speed icon  located on the toolbar.

9. Focus the image by clicking on the “**working distance**” icon , which is in the toolbar. Spin the Trackball from left to right to adjust the focus (Fig. 8). Additionally, right click on the mouse and select “**Auto WD.**”

10. Alternatively, checking the spot size may also improve image quality. The spot size is determined by the beam intensity value, right click on the image and select “**Auto BI OptiMag.**”

B. Wobble

1. Wobble adjusts the focal point of the sample up or down in relation to the sample, the wobble setting centers the objective lens. If the image rocks (shakes) back and forward, then adjustments are needed.

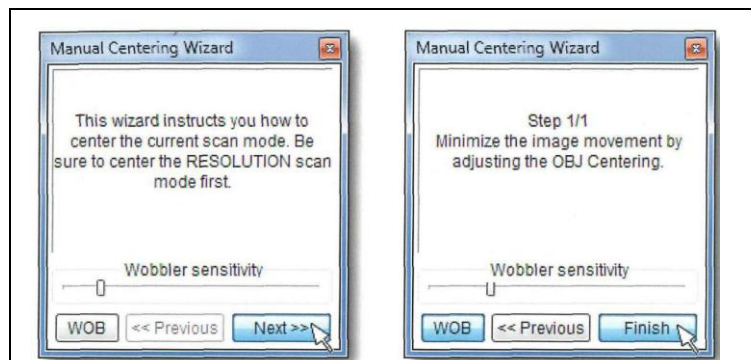


Fig. 9 Wobbler sensitivity.

2. Click on the wobble icon  to start the adjustment. The Manual Centering Wizard will appear (Fig. 9), click on the “**Next>>>**” button.
3. There are two adjustable values for centering the image. To ensure that only one value is changing, hold down the F12 key to change only the X movement and adjust with the Trackball, and hold down the F11 key to change only the Y movement and adjust with the Trackball.
4. Select “**Finish**” once the image is adjusted appropriately.

C. Alignment of the Electron beam (i.e., “Focusing” and “Stigmation,” this step is optional)

1. When observing images at higher magnification, the image loses focus and astigmatism needs to be corrected. This can be corrected by clicking on this icon  and manually adjusting it using the F11 and F12 keys in a similar manner as for the wobble function.
2. Alternatively, right click and select “**Auto Stigmation.**”

D. Acquiring (saving image)

1. To change the parameters of the image being collected, click on the “**SEM**” option on the main upper menu and then select “**Image Parameters**”, the scanning speed at which the image is being acquired can be adjusted (Fig. 10 and 11). Additionally, for low conductive samples, it may be best to collect the image in the current speed, click on “**Keep actual speed.**”
2. To save the image click on the “**Acquire**” button, which is the last icon on the toolbar . A “Header of Save” window will appear, click cancel and proceed to Step 3.
3. Choose the appropriate folder to store the image under your research group.

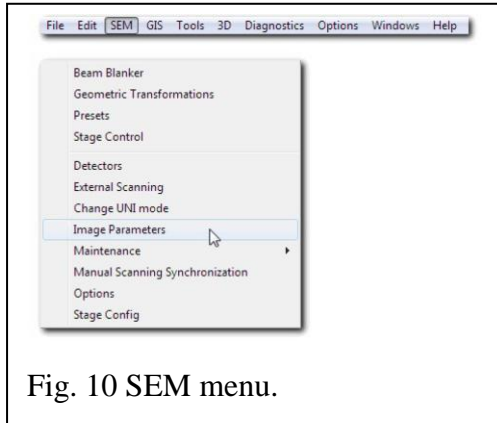


Fig. 10 SEM menu.

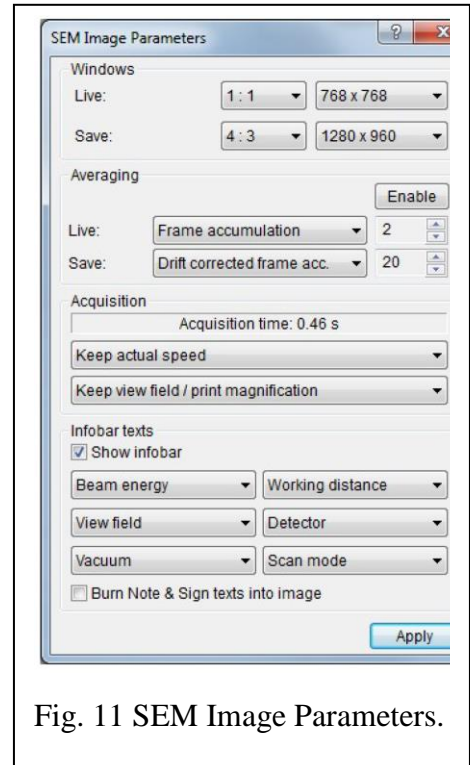


Fig. 11 SEM Image Parameters.

E. Logging Off

1. If the sample needs to be analyzed by EDX then proceed to **Section IV**, and do not close out of the program or remove the sample.
2. If the sample does not need to be analyzed by EDX, then the sample may be removed (while wearing gloves) by the reverse process in **Section II** and summarized briefly below.
 - >>1) Click on the “Home” button in the stage control panel; 2) Click on the “Vent” button in the vacuum panel, so that the microscope can be vented; 3) Open the chamber door carefully; 4) Use the stage control panel to select the sample position; 5) Use a screwdriver or Allen wrench to loosen the screw on the sample stage for that specific sample; 6) Remove the sample; and 7) Use a screwdriver or Allen wrench to tighten the screw.
3. Once the sample has been removed and the microscope is vacuum ready by having selected “**Pump**,” then close out of the program. Click “Exit Only.” The other option will switch off the instrument. **DO NOT** click on that option **IV. Energy Dispersive X-Ray (EDX) Detector**

A. Getting Started

1. Turn off the chamber view on the SEM by clicking on the camera icon .
2. Leave the program for the VEGA microscope open.
3. The program used for EDX is Pathfinder, which is located on the **right monitor**, click on this icon .
4. The program will open and there will be a window that appears, prompting the user to select the folder in which the image of interested is located. Double-click on the appropriate folder.
5. Click on **“Get Image”** located under **“Spectral Imaging”** on the right-hand side of the screen, as shown below in Fig. 12.

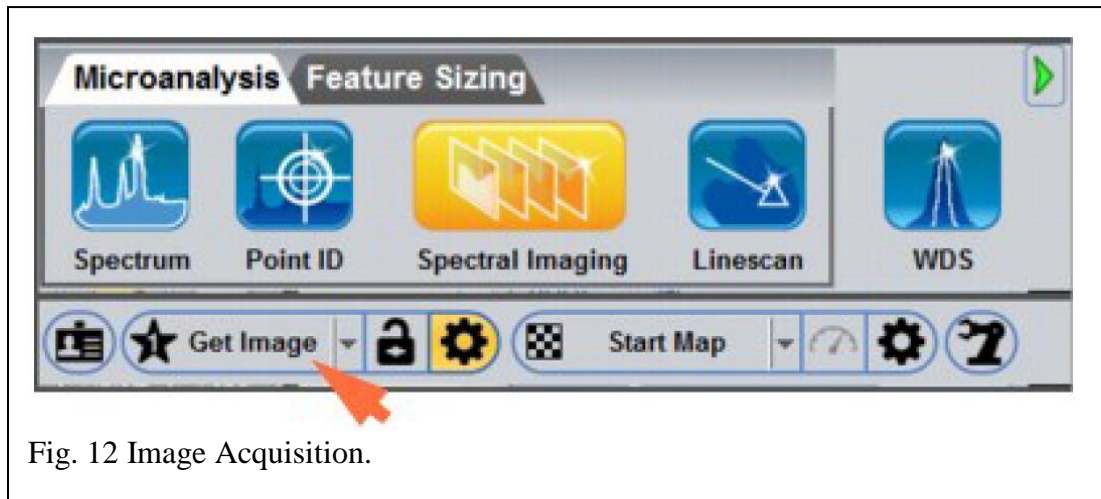
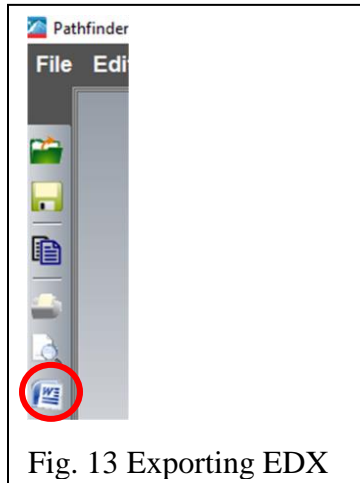


Fig. 12 Image Acquisition.

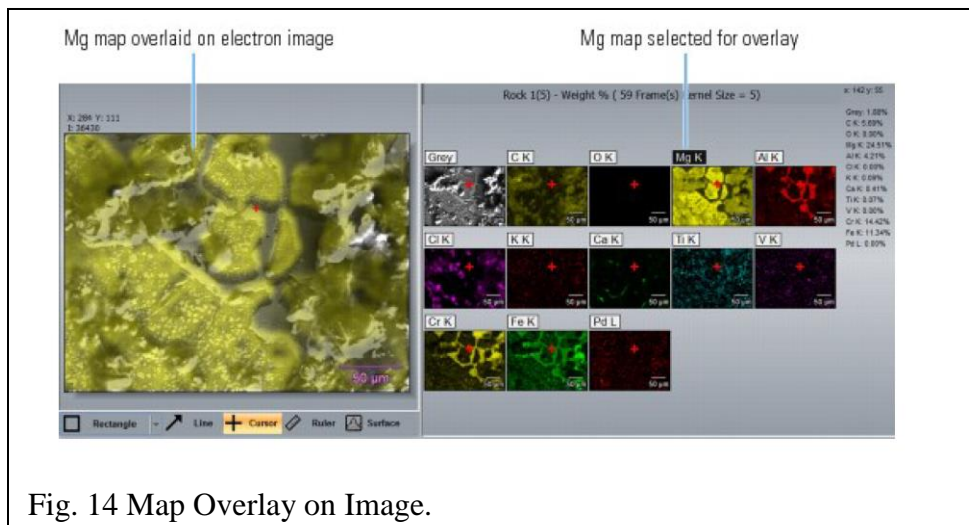
6. The image will load and appear on the left screen. Before starting analysis, click on the experiment setup button next to **“Start Map,”** which is located next to **“Get Image.”** Select the appropriate settings for the sample or consult your PI. Average map acquisition settings include: resolution of 256x192, frame time 20 seconds, number of frames 200, low energy cutoff 100, high energy cut off auto, and time constant rate 3.
7. For EDX, try to increase the **“cps”** (counts per second, located on the bottom left of the screen) above 1000 (kcps) to get an optimum spectrum; this may be done by increasing the voltage on the **“HV”** button, which is located on the left monitor in the Tescan Vega program.
8. Start EDX analysis by clicking **“Start Map.”**
9. After the spectrum is collected, save it by exporting it into a Word document. This is located underneath the File button, as shown in Fig. 13 below.



B. Overlay Maps and Electron Image

Individual or multiple element maps can be overlaid on the image to see if the detected elements correspond to features on the sample. Overlaying is done after a map has been collected for EDX. Then, the detected elements can be overlaid.

1. Click the element label above the map; the element symbol will turn black, as represented in Figure 14. This will overlay the selected element on the image.



2. The transparency and brightness of the selected element can be adjusted by selecting the “**Image Settings**” tab on the control panel.

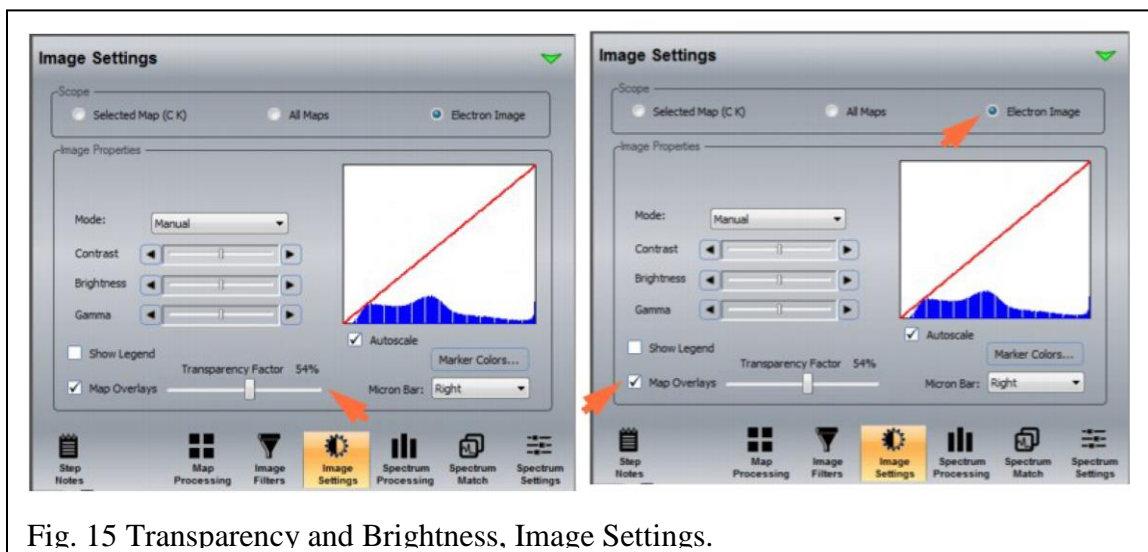


Fig. 15 Transparency and Brightness. Image Settings.

3. To overlay multiple elements on the image, select the “**Image Settings**” button as represented in Fig. 15.
4. Set Scope to “**Electron Image**” and click the element label above the map. The element symbol will turn black, as represented in Fig. 14. Then, click on “**Map Overlays**.”
5. To display the legend for the elements located in the image, click on “**Show Legend**,” which is above the Map Overlays option in the image settings.
6. Additionally, to better help identify the elements found, their color can be changed. This can be done for each individual element by clicking on “**Selected Map**” located in the Scope option.

C. Automatic Quantitative Analysis (weight% and atomic %)

1. To quantify the chemical elements detected, click on “**Spectrum**” in the Microanalysis tab (Fig. 16).

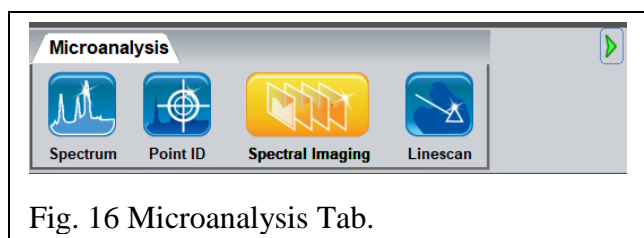


Fig. 16 Microanalysis Tab.

- Under Spectrum Processing (Fig. 17) select “Quant Setup” and click “Process.”

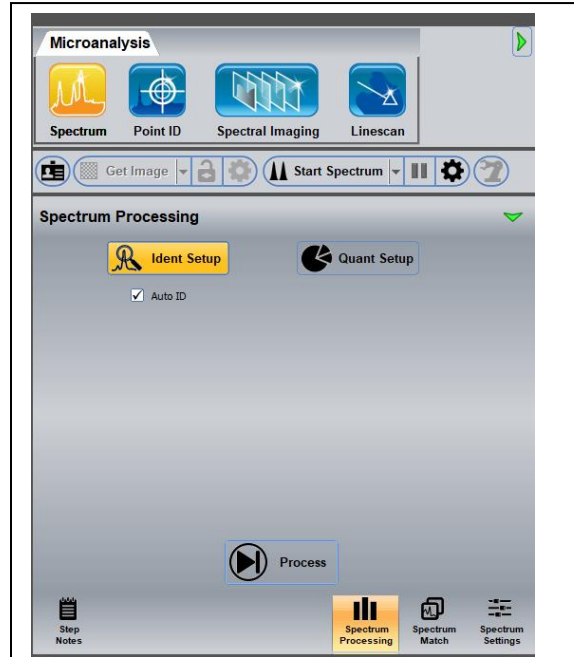


Fig. 17 Quant Setup.

- A table of elements with their corresponding weight % will be generated. This may be exported by clicking the MSWord icon underneath File in the upper left corner (see Fig. 18).

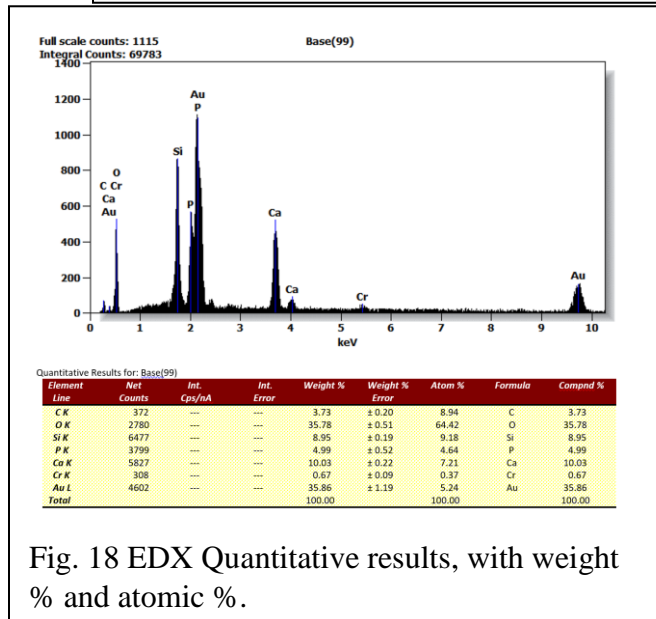


Fig. 18 EDX Quantitative results, with weight % and atomic %.

D. Logging Off

- When finished with the program, simply exit out of Pathfinder, and click “okay.” Go back to **Section III, E** for directions on sample removal and place SEM in standby mode. Make sure you sign out of th